

Universiteit
Leiden
The Netherlands

Manipulating carbon nanotubes Towards the application as novel field emission sources

Heeres, E.C.

Citation
Heeres, E. C. (2014, October 2). *Manipulating carbon nanotubes Towards the application as novel field emission sources*. Retrieved from https://hdl.handle.net/1887/28966

Version:	Not Applicable (or Unknown)
License:	Leiden University Non-exclusive license
Downloaded from:	https://hdl.handle.net/1887/28966

Note: To cite this publication please use the final published version (if applicable).

Cover Page



Universiteit Leiden



The handle http://hdl.handle.net/1887/28966 holds various files of this Leiden University dissertation

Author: Heeres, Erwin
Title: Manipulating carbon nanotubes towards the application as novel field emission sources
Issue Date: 2014-10-02

Manipulating carbon nanotubes

Towards the application as novel field emission sources

Manipulating carbon nanotubes

Towards the application as novel field emission sources

Proefschrift

ter verkrijging van
de graad van Doctor aan de Universiteit Leiden,
op gezag van Rector Magnificus prof. mr. C.J.J.M. Stolker,
volgens besluit van het College voor Promoties
te verdedigen op donderdag 2 oktober 2014
klokke 10:00 uur

door

Erwin Cornelis Heeres

geboren te Oss
in 1977

Promotiecommissie

Promotoren:

Prof. dr. ir. T.H. Oosterkamp	Universiteit Leiden
Prof. dr. N. de Jonge	Universität des Saarlandes

Overige leden:

Prof. dr. J. Aarts	Universiteit Leiden
Prof. dr. E.R. Eliel	Universiteit Leiden
Prof. dr. J.W.M. Frenken	Universiteit Leiden
Prof. dr. ir. P. Kruit	Technische Universiteit Delft
Dr. ir. S.J. van der Molen	Universiteit Leiden
Prof. dr. J.M. van Ruitenbeek	Universiteit Leiden
Dr. D.F.E. Samtleben	Universiteit Leiden

Casimir PhD series, Delft-Leiden 2014-21 ISBN 978-90-8593-194-2

An electronic version of this thesis can be found at https://openaccess.leidenuniv.nl and at http://www.interfacephysics.nl

The research described in this thesis was performed at the Leiden Institute of Physics, Leiden University, Niels Bohrweg 2, 2333 CA Leiden, The Netherlands and at Philips Research Laboratories, High Tech Campus 4, 5656 AE Eindhoven, The Netherlands. This work was supported by FEI Company and by the Dutch Ministry of Economic Affairs.

toc

Table of contents

1 Introduction **11**
1.1 Electron beams and applications 12
1.2 Electron sources 16
1.3 Carbon nanotubes 20
1.4 Carbon nanotube and other novel electron sources 22
1.5 Research questions 24
1.6 Results and discussion, summary, and future outlook 26
1.7 Layout of this thesis 27

2 Theory of electron emitters **39**
2.1 Fowler-Nordheim field emission model 40
2.2 Field emission current density 43
2.3 Field emission energy distribution 46
2.4 Distribution of transverse energies 47
2.5 Limitations of the Fowler-Nordheim theory 49
2.6 Field emission microscopy 50

3 A compact multi-purpose nanomanipulator for use inside a scanning electron microscope **59**
3.1 Introduction 60
3.2 Design considerations 60
3.3 Stage movement and stability 63
3.4 Nanomanipulator operation 66

3.5 Applications 69
3.6 Conclusions and discussion 72

4 Mounting techniques **77**
4.1 Sample preparation 78
4.2 Mounting techniques 82
4.3 Enhancing the mechanical contact of mounted probes 93
4.4 Conclusions and discussion 96

5 Making carbon nanotube electron sources of defined lengths and with closed caps **103**
5.1 Introduction 104
5.2 Cutting a carbon nanotube to length 104
5.3 Closing the cap of a MWNT 108
5.4 Electron emission characterization 111
5.5 Conclusions 113

6 Size of the localized electron emission sites on a closed multi-walled carbon nanotube **119**
6.1 Field emission patterns from carbon nanotubes 120
6.2 Field emission microscopy and its resolution 120
6.3 Carbon nanotube model 121
6.4 Mounting and TEM characterization 122
6.5 MWNT imaging inside the FEM 122
6.6 Transverse energy distribution and deconvolution of the emission pattern 125
6.7 Conclusion and discussion 129

7 Electron emission from individual indium arsenide semi-conductor nanowires **137**
7.1 Introduction 139
7.2 Sample preparation 139
7.3 Electron emission characteristics 143

7.4 TEM analysis 146
7.5 Conclusions and discussion..... 150

Appendix A **157**
A.1 Nanomanipulator specifications 157
A.2 Parts 157
A.3 Nanotube (or nanowire) mounting recipe 158

Summary **161**

Samenvatting **165**

List of publications **169**

Curriculum Vitae **171**

Acknowledgements **173**

1

Introduction

In an electron microscope (EM), samples and processes are imaged or studied with a resolution of several nanometers, or even a fraction of a nanometer, depending on the type of microscope and sample.[1] Besides imaging, other applications exist, such as the analysis of materials and processes, device testing, sample fabrication, deposition, and etching.

In this chapter some basic EM-principles and applications will be discussed first, after which the electron sources are treated in *Section 1.2*. Starting with the state-of-the-art sources, we will address the need for novel electron sources and introduce the (novel) materials in *Section 1.3 and 1.4,* which have been used throughout the research that is presented here. In *Sections 1.4 and 1.5* our research questions are posed, followed by a brief summary of the results and an overview of the project of which this research was a part in *Section 1.6*. Finally, in *Section 1.7*, the contents of the following chapters in this thesis are described.

1.1 Electron beams and applications

The key advantage of an electron microscope over a light microscope is the use of a beam of electrons, which behave like waves with much shorter wavelengths than photons in visible light. Using the equation for a free electron gas, the (relativistic) electron wavelength can be written as:[2]

$$\lambda = \frac{h}{p} = \frac{hc}{pc} = \frac{hc}{\left(E_{\text{kin}}{}^2 + 2E_{\text{kin}}m_0c^2\right)^{1/2}} \tag{1.1}$$

where λ is wavelength, h Planck's constant, c the speed of light in vacuum, E_{kin} the kinetic energy, and m_0 the electron rest mass. An electron with a kinetic energy of 200 keV has a corresponding wavelength of 2.5 pm, which is five orders of magnitude lower than the wavelength of a photon in visible light ~ 10^2 nm. Because of this difference in wavelength, the diffraction limit – being the fundamental resolution limit of an optical system that scales linearly with wavelength – is lower for electrons, and hence a higher resolution can be obtained using electron microscopy. However, this fundamental limit is not reached due to aberrations by imperfections in electron lenses which standard electron microscopes do not correct for. Chromatic and spherical aberrations cause the achievable resolution limit in a non-corrected electron microscope to be about 100 times higher than the electron wavelength.[3] Note that recent developments have led to systems for the correction of chromatic- and spherical aberrations.[4]

Three basic types of electron microscopes exist:

- Transmission electron microscope (TEM)
- Scanning electron microscope (SEM)
- Scanning transmission electron microscope (STEM)

In a TEM, displayed schematically in Figure 1.1a, the electron beam is transmitted through a section of the sample, hence restricting its thickness to approximately 100 nanometers, followed by a magnification and projection onto a phosphor screen or CCD camera. Both above the sample – for probe forming – and underneath – for

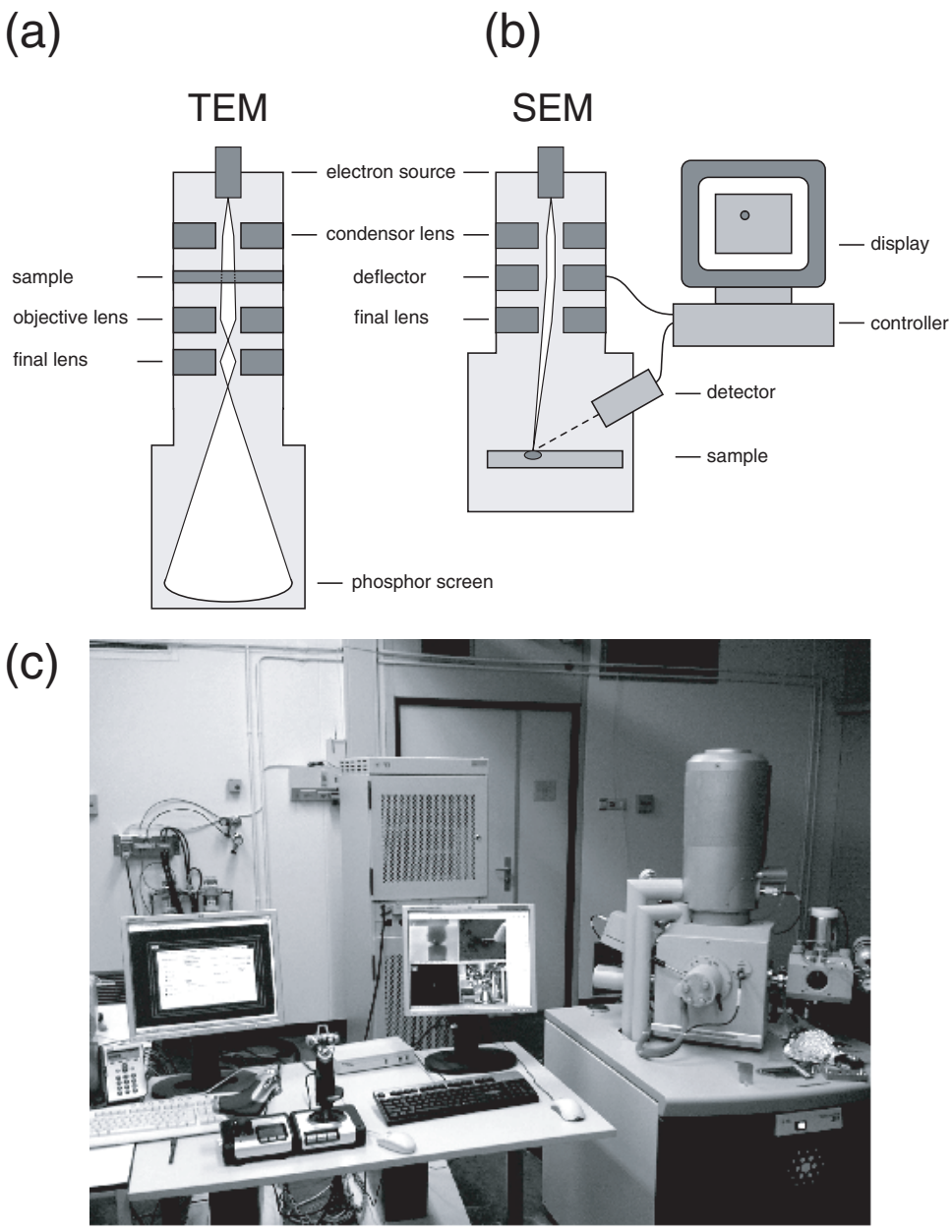


Figure 1.1 (a),(b) Schematic representation of a transmission electron microscope (TEM) and a scanning electron microscope (SEM). (c) Photograph of the SEM at Leiden University. The joysticks in between the two keyboards are used to operate the nanomanipulator inside the SEM.

projection – lenses are placed within short distances, hence enabling small focal lengths and keeping aberrations low, but restricting the overall size and movement of sample and holder within the millimeter range. The SEM employs a system to focus the electron beam into a spot with a typical diameter of about 1 nm (probe) and to deflect it in such a way as to scan the sample point by point and line by line, as shown schematically in Figure 1.1b. At each point of this scan, the electron signal collected at a detector – installed inside the vacuum chamber – is a measure for the intensity of the image that is generated point by point. Due to the layout of the SEM, usually with one lens column several millimeters to centimeters above the sample, the use of larger samples and larger movements are allowed. Compared with TEM, an SEM uses lower beam energies, typically ranging from 1 keV up to 30 keV, with corresponding lower resolution as a result. The resolution capabilities of both instruments are sketched in Figure 1.2.[5-7] Shown in Figure 1.1c is the setup of our SEM in Leiden. The scanning transmission electron microscope (STEM) uses an electron probe to scan the sample, as in an SEM, and subsequent recording of the transmitted electron beam. Recently, an experiment showing a resolution below 50 pm was published, using a TEM at 300 keV in scanning probe mode (STEM), corrected for spherical and chromatic aberrations.[8]

Apart from obtaining structural information of a sample, electron microscopes are often used for chemical analysis techniques,[9] based on interactions of the electron beam with the atoms in the specimen, such as electron energy loss spectroscopy (EELS), and energy dispersive x-ray spectroscopy (EDX). In EELS, the energy spectrum of the reflected/transmitted electron beam is studied for electron energy loss due to inelastic interactions with the species of the sample, like phonon excitations and ionization of inner shell electrons.[10] In EDX, the spectrum of x-ray radiation originating from electron interactions with the species of the sample is analyzed.

Also, electron beams focused into nanometer spots can be used for electron beam lithography. In such a system, the electron beam is used to define a pattern on a sample with an electron-sensitive resist by moving both the electron beam (deflection) and the stage (translation) with respect to each other. In this way,

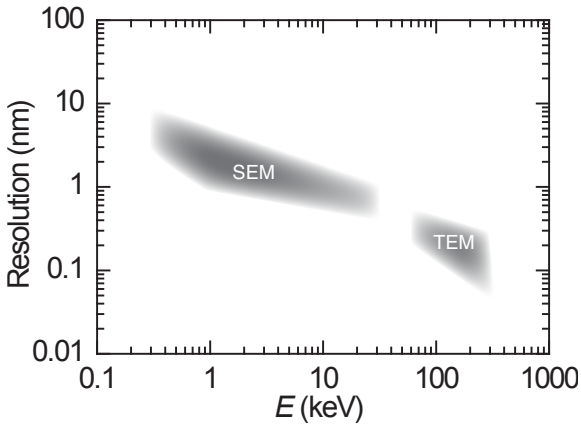


Figure 1.2 Indication of SEM and TEM resolution ranges as a function of electron beam energy.

structures with dimensions of 10 nm and smaller can be defined without the use of a mask.[11,12]

Finally, one of the first setups to study surfaces with near-atomic resolution was the field emission microscope (FEM),[13] which was also used throughout the research presented in this thesis to study the relation between an electron source and the electron beam emitted from it. To achieve this, a sharp tip (source) is placed in a high electric field inside a vacuum chamber, causing field emission of electrons; this electron beam is then imaged using a phosphor screen.

1.1.1 Electron beam-specimen interactions

Due to the interaction of an incident electron beam with the atoms in a specimen, a wide range of signals is available for imaging and analysis, see Figure 1.3. Some incident electrons are reflected or scattered back elastically – without loosing energy – also known as backscattered electrons (BSE). Other incident electrons loose energy by inelastic scattering events, knocking out electrons from the atoms of the specimen; the latter being secondary electrons (SE) and Auger electrons. Besides elastic and inelastic reflection of electrons, also transmission of both types exist which can be used in different ways for image formation.[14] Characteristic x-rays, generated within the interaction volume, can be used to map the elemental

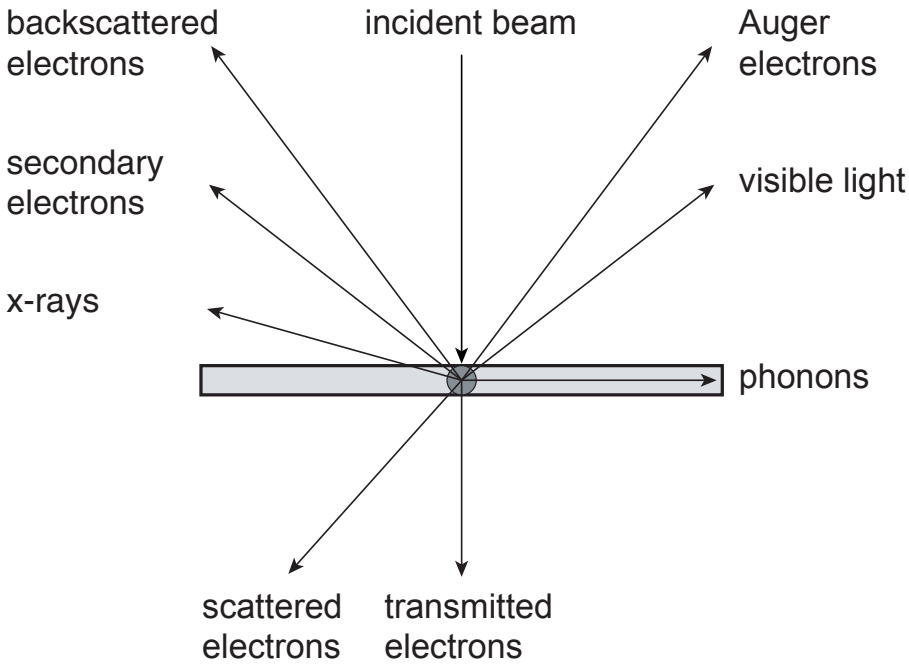


Figure 1.3 Schematic representation of the interactions of an incident electron beam with a specimen.

distribution of the sample with an EDX detector. If the sample is thin enough, electrons can be transmitted through the sample which is a prerequisite for the transmission electron microscope, as the transmitted electrons are used for imaging. Also for the scanning electron microscope, transmission detectors are available to perform scanning transmission electron microscopy (STEM), offering sub-nanometer resolution at ~30 keV beam energies, while restricting sample sizes.[15]

In Chapter 5, experiments are described in which the electron beam has been used to cut through carbon nanotubes.

1.2 Electron sources

In this section, the different types of electron emission will be discussed, as well as the key requirements for electron sources. Hereafter, the common commercially

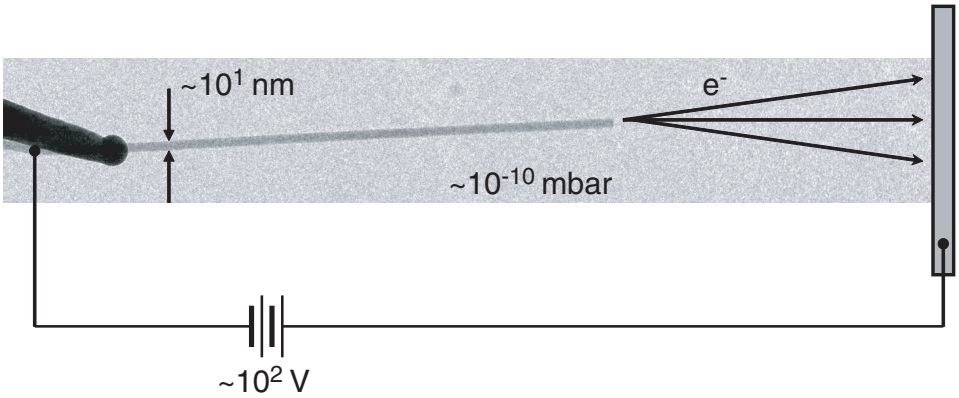


Figure 1.4 Schematic representation of an electron field emitter. Mounted onto a sharp tip is a high aspect ratio nano-object, i.e. a nanotube or -wire, with a typical diameter of several nanometers. In a vacuum chamber at a pressure of 10^{-10} mbar, electrons are emitted towards the anode, typically by applying an extraction voltage of several hundred volts.

used sources are compared.

1.2.1 Electron emission and source types

In an electron source, electrons are extracted from a solid material (cathode) and accelerated into vacuum towards an anode, creating an electron beam. In Figure 1.4 a nanowire emitter is shown, drawn within a schematic extractor setup. Several extraction mechanisms exist, that differ in the way which electrons pass the potential barrier between the cathode surface and vacuum. One way is to give the electrons sufficient energy to overcome the potential barrier; another way is to modify the potential barrier in such a way as to enable electron tunneling. The potential difference between the Fermi energy E_F and the vacuum is called the work function ϕ. In the first case, the electron energy is elevated by a high temperature or photon irradiation; called thermionic emission and photoemission, respectively. In the second case, the potential barrier is modified by an electric field. The electrons in the source placed within the attractive electric field will still see a barrier, but its width is reduced depending on the electric field strength, see Figure 1.5. Lower energy electrons will see a wider potential well, whereas higher energy electrons will see a thinner potential well, and have a higher tunneling probability.[16]

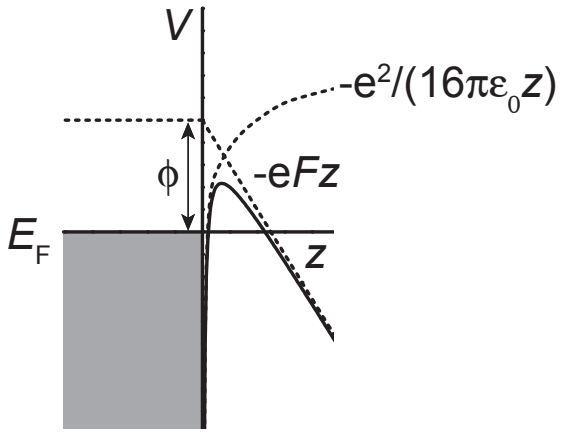


Figure 1.5 Potential for an electron outside the emitter as a function of distance from the emitter surface. The potential is made up of two parts: the image charge potential and the potential due to the applied electric field. Also indicated are the Fermi energy E_F and the workfunction ϕ. For simplicity the Fermi-Dirac distribution at 0 K is drawn and the filled (metallic) states are indicated in grey.

Electrons around the Fermi energy will be emitted, where the temperature (Fermi-Dirac distribution drawn for $T = 0$ K) determines the high-energy part of the field emission energy spectrum and the tunneling parameter[17] determines the low-energy part of the spectrum. This type of emission is called (cold) field emission. Schottky- or thermal field emission is the combination of emission at an electric field and at a high temperature.[18]

To improve upon the capabilities of electron microscopes, we first need to address the key requirements for a good electron source. These are: high brightness, low energy spread, high stability, and a long lifetime. Higher brightness will lead to more current in the same spot, and as a result faster imaging, analysis, or e-beam writing is possible. A low energy spread reduces chromatic aberrations. Stability can be divided in short- and long-term stability. Short-term stability is needed for proper measurements, as instabilities cause measurement errors. Long-term stability determines the time a source can be operated and hence affects its lifetime. With a longer lifetime, the source needs to be replaced less often and because of this it is more user-friendly and cheaper.

Table 1.1 List of characteristic parameter values for three most used commercial electron sources; the Schottky emitter, cold field emission gun (CFEG), and the LaB_6 emitter. Source: N. de Jonge.[19]

	Schottky	CFEG	LaB_6
Energy spread (eV)	0.4 – 0.7	0.25 – 0.3	1.0
Reduced brightness ($A \cdot m^{-2} \cdot Sr^{-1} \cdot V^{-1}$)	$(0.3 – 1.0) \times 10^8$	$(1 – 2) \times 10^8$	10^5
Geometric source size radius (nm)	900	50	15000
Virtual source size radius (nm)	15	2.5	10^4
Emission stability short term (%RMS)	< 1	3 – 5	< 1
Typical lifetime (h)	> 5000	> 1000	200
Operating temperature (K)	~ 1800	~ 300	~ 1700
Operating vacuum level (mbar)	$< 10^{-8}$	$< 10^{-10}$	$< 10^{-6}$

Common commercially used emitters are the LaB_6 source, the tungsten (W) cold field emission gun (W-CFEG) and the Schottky emitter. These three sources are listed in Table 1.1 together with their parameters.[19] The first type uses a low workfunction crystal – lanthanum hexaboride – and usually has a large virtual source size and low brightness. The W-CFEG has a tip with a radius of curvature ~50 nm, where electrons are extracted within a strong electric field at low temperatures, i.e. cold FE. A low energy spread and high brightness are characteristic features of this source which is used in ultrahigh resolution instruments. Instabilities of the tip shape and emission surface require periodical reprocessing of the tip, hence this

source is not the most user-friendly one. The Schottky emitter has high brightness, but a higher energy spread than the W-CFEG. A tungsten tip, coated with a workfunction-lowering layer of ZrO and its radius $r \sim 0.5$ μm, forms the base of this source which is being used in many modern electron microscopes.[20]

1.2.2 Characterization of sources

To characterize an electron source, the parameters mentioned in the above have to be determined and compared. After fabrication of the source, it is transferred into a field emission test setup and cleaned from adsorbed species by heating. The presence of such species is indicated by changes in the emitted current and in the image of the field emission microscope, as adsorption and desorption events locally change the field emission properties of the tip. In dedicated FE-test setups current-voltage (I-V) characteristics are measured, together with angular current density, virtual source size, energy spread, current stability, and lifetime. Models for the field emission energy distribution (FEED) and FE current can be fitted to the data and used to obtain characteristics of the source, such as electric field strength, operating temperature, tunneling parameter, etc.. The stability of the source structure affects its lifetime and emission current stability. To obtain information about the source's structural stability during field emission, TEM images before and after field emission experiments can be compared, or the source can be tested in-situ, i.e. performing TEM imaging during electron emission.[21] Such structural information can be used to explain observations during field emission measurements and gives insight in the long-term stability of the source. This is why Feynman's quote "Just look at the thing" was used as an introduction to this thesis.

1.3 Carbon nanotubes

Carbon nanotubes[22-25] have unique mechanical and electronic properties, see the quantities listed in Table 1.2.[26-29] Due to their size and structure, these mechanical and electronic properties are of great interest for potential applications, one of which is their use as next-generation field emission sources.[30] A carbon nanotube can be considered as one single layer of graphite (graphene) rolled-up into a single cylinder, creating a single-walled carbon nanotube (SWNT). A multi-walled carbon

Table 1.2 Carbon nanotube parameters

	SWNT	MWNT
Minimum diameter (nm)	< 1	~ 2
Maximum current density[26,27] ($A \cdot cm^{-2}$)	> 10^9	10^9 - 10^{10}
Young's modulus[28] (Pa)	~ 10^{12}	~ 10^{12}
Tensile strength[28] (Pa)	~ 10^{10}	~ 10^{10}
Wall separation distance[29] (nm)	-	0.34

nanotube (MWNT) can be considered to consist of multiple SWNTs wrapped around each other to form concentric tubes. The shell or wall separation distance between adjacent tubes is roughly equal to the plane spacing of graphite, 0.34 nm. Both SWNTs and MWNTs are made out of covalently bound carbon atoms, in a two-dimensional hexagonal lattice with sp^2 type carbon-carbon bindings,[31] making them very stiff, chemically stable structures and able to carry large current densities up to 10^9 A/cm^2.[26,32] Most of all, they are known for their exceptionally high Young's modulus, up to 1 TPa for single CNTs.[28] When CNTs are combined into macroscopic bundles, the reported Young's modulus is significantly lower, around 80 Gpa. However, electron beam treatments have shown to be able to reinforce such bundles.[33,34] To close a rolled-up graphene sheet, i.e. to create closed caps, half a fullerene molecule is needed on each of its ends – one of which is C_{60}, Buckminsterfullerene[35] – as the graphene lattice cannot be bent in such a way to form a closed structure.[36] Local changes in the atomic configuration (defects) have to be introduced to create local curvature in the otherwise "flat" (although it is rolled-up) sheet and to form a hemi-spherical-like cap.[37] These defects are five-membered carbon rings, named pentagons, and their presence is believed to cause local electronic states, i.e. peaks in the local density of states (LDOS) as compared to the bulk density of states (DOS).[38] If not closed, the cap of the CNT is left open with dangling bonds, which is a less stable configuration for field emission of electrons than the closed cap configuration.[39] The position of the pentagons determines the shape of the cap, which can vary between spherical and flat.

The electrical properties of CNTs depend on the orientation of lattice parameters with respect to the tube's length; SWNTs can be either semi-conducting or metallic.[40] The electrical properties of MWNTs depend on the properties of the tubes it consists of, where a weak electronic intertube coupling exists and current is transported mostly through the outermost shells.[29,41,42]

Although the properties of CNTs change significantly depending on whether they come in bundles, other arrangements, or dispersed within a carrier medium, many consumer products are available nowadays that make use of carbon nanotubes.[43-47] Growing long CNTs to be used as fibers is one of the ultimate goals, [48] yet another approach to make material primarily based upon CNTs is to spin yarns out of samples containing many CNTs.[49,50] Some examples of single CNT applications are the single-electron CNT field effect transistor,[51] an ultrasensitive CNT mass sensor,[52] a CNT radio transmitter/receiver,[53] and scanning probe microscopy tips.[54-56]

1.4 Carbon nanotube and other novel electron sources

Due to the unique properties of carbon nanotubes – see the previous section – they have already been used to study field emission, as described in the PhD thesis by Fransen.[57] Their strength and size make them candidates for stable (cold) field emission sources with a low energy spread and high brightness. The characterization and understanding of field emission from carbon nanotubes and any other nano-materials is needed, to make best use of their properties for next generation electron sources.

1.4.1 Carbon nanotube electron sources

Using a carbon nanotube, a source from a very strong material can be constructed that permits high current densities, has a small (emitting) area at its end where several sites with a high density of states exist.[58] Besides this, CNTs can be heated up to high temperatures, which is beneficial for the removal of adsorbed species, and have a high aspect ratio due to which a relatively low potential difference between anode and cathode already causes the electric field strength to exceed the

typically needed value for field emission, ~10^9 V/m.

As field emission will most likely occur at positions where the electric field strength is highest, for a CNT this means emission is most likely to occur at its apex. The existence of a fullerene-like cap is believed to determine the emission stability. Without such a fullerene-like cap, a so-called open cap, the emission current shows instabilities, probably due to the existence of dangling bonds.[59] FEM patterns of such open CNTs show temporal and spatial fluctuations within the beam.[39] As was shown by de Jonge et al., it is possible to create a closed cap again after having cut a CNT to a specific length first. Such a closed cap structure shows improved stability that is visible both in the current and in the FEM pattern. However, it did not show the beam profile as obtained from pristine as-grown closed capped MWNTs, with several localized regions of high emission current density.[60] These regions are attributed to regions of high local density of states,[38,58] but their exact relation to field emission is not yet clear. In between such local regions of high emission current density, fringe-like features are found that are attributed to electron interference.

1.4.2 Nanowire electron sources

Besides CNTs, other materials exist with interesting properties for field emission. Nanowires with a 1D density of states can be of interest, as their energy levels are occupied in a completely different way then a 3D quantum system.[61] Systems with such a density of states might be used to obtain an electron beam with a very low energy spread. However, the effects of band bending on the DOS of such systems under application of a large electric field are not yet known. Will there be enough free charge carriers? Another question is whether or not such structures will survive field emission. Do they meet the necessary requirements regarding stability, lifetime and brightness? Following research and theoretical calculations performed by Antonio Calvosa, Lou-Fé Feiner, Erik Bakkers and Niels de Jonge, measurements on indium-arsenide (InAs) nanowires are presented in Chapter 7 of this thesis. These nanowires were characterized before and after measurements using TEM and EDX.

1.5 Research questions

In the previous section on novel field emission sources, already a few points were mentioned that need clarification. Regarding field emission from carbon nanotubes several questions can be asked.

What do we see when we image the field emission pattern of a closed or open CNT? As the cap, open or closed, is at the very end of the CNT, this will be the position at which the applied electric field strength will be highest and most electrons are expected to leave the CNT. Hence, a FEM pattern will be a magnified map of the CNT end showing the locations with highest emission probability, which is affected by the local electric field strength, work function, and density of states. As can be concluded from experiments performed by other groups, the state of the cap of a carbon nanotube affects its emission properties significantly.[62-64] Additionally, it is necessary to consider the electron trajectories from a particular position on the cap to the screen.

Having a fullerene-like capped CNT emitter, it is argued that emission comes from the carbon atoms within the pentagon rings and that therefore a very small (virtual) source size is to be expected. The diameter of a pentagonal carbon ring equals 0.248 nm.[65] However, as has been calculated theoretically, the area with a high LDOS might be larger than the pentagon area.[66] We believe it is possible to use field emission microscopy on closed CNTs to reveal the emission sites and to determine their sizes. To do so, the geometry of the emitting structure and the magnification of the FEM should be known in order to calculate the corresponding sizes on the CNT cap from the FEM pattern. The information about the size and structure of the CNT needed to do this can be obtained by imaging the source in a TEM after the field emission measurements.

If the shape of the CNT cap is purely hemispherical, a configuration that is achieved with a central pentagon and five surrounding pentagons at equal distances from the center, the electric field strength can be assumed to be constant over the entire cap. Assuming the work function does not vary significantly over the cap, the FEM pattern will then show the LDOS. By comparing FEM images on small and

large diameter CNTs, only large diameter CNTs have clearly shown six localized emission sites at the CNT cap,[60] whereas small diameter CNTs show different emission patterns.[67] So to study the properties of local emission sites of carbon nanotubes, we have used relatively large ~10 nm diameter MWNTs.

Due to the transverse energy spread of the electrons – the normal energy determines its tunneling probability – the LDOS information in the FEM pattern is blurred. By calculating the field emission energy distribution (FEED), it is possible to estimate the tunneling parameter and to simulate the transverse energy beam broadening by means of a point spread function (PSF). This PSF can then be used for deconvolution of the FEM pattern and should reveal in more detail the LDOS at the CNT cap.

By mounting a single emitting MWNT without destroying its as-grown cap, we also believe it is possible to determine the origin of interference fringes observed in FEM patterns. These interference fringes are assumed to be single-nanotube effects, however, those measurements were performed using a sample containing many emitting CNTs.[68] To make sure this interference is not a multiple-CNT effect, we have constructed a source with only one emitting CNT.

On the mechanism behind the formation of interference fringes two different theories exist. One claims the interference pattern is built up from electrons interfering with the Fermi-wavelength, hence the FEM pattern shows a magnification of the electron wavefunction at the CNT cap; the phase difference between two paths from different emission sites towards a point on the screen of the FEM is believed to be zero and not to depend on the acceleration voltage.[69] Alternatively, the electrons may interfere with the wavelength obtained during their acceleration.[68] By measuring the interference fringe spacing as function of the extraction/acceleration voltage on a single emitting CNT, as presented at the end of Chapter 6, we have ruled out the possibility that the interference is already present on the cap.

Following up on the cap closing experiments on thin MWNTs (having approximately 5 walls) by de Jonge et al., we think it should be possible to create a closed cap showing localized emission sites using a MWNT that has been cut to length after

mounting it onto a support tip, i.e. having removed its as-grown cap. Possibly the experiments by de Jonge did not show similar FEM patterns as the ones by Saito,[60] either due to their small diameter or due to a more amorphous carbon cap. We have used large (~10 nm) diameter MWNTs, and combined heat treatment and field emission experiments to induce a reorganization of the carbon atoms in the CNT apex. In Chapter 5 we will address the questions if it is possible to close such a cap, to enhance its graphitization and to change the shape of such a cap and what FE properties the resulting structure will show.

1.6 Results and discussion, summary, and future outlook

In Chapter 6 of this thesis we describe the measurements that provide a better understanding of local emission sites and interference effects visible in electron emission patterns from CNTs. First of all, such emission sites are measured to be larger than the diameter of a single pentagon. Also the virtual source size measurement shows a larger value. We demonstrated the interference is a single nanotube effect, and it appears that the interference pattern obtained is not a magnification of the electron wavefunction at the cap, but it is caused by phase differences between paths from different emission sites at the CNT cap towards the measurement screen, and is related to the extraction voltage and hence to the De Broglie wavelength of the electrons. (A simple analytical model yielded similar results as those which were obtained from measurements.) These results were obtained from unmodified, as-grown nanotubes.

Similar local emission sites were also reproduced using modified CNTs, i.e. MWNTs that were cut to length during the source mounting procedure inside the SEM. In the process of field emission and heating, changes in the cap structure were induced, which were also visible in the FEM pattern and the emission stability. If this process is further improved upon, it should be possible to obtain robust MWNT emitters with specified sizes and well graphitized caps that exhibit stable emission, low energy spread and a high brightness. The typical pattern of a well graphitized MWNT can be used to check the source status if, for example, used in a TEM.

To select and mount such CNT field emitters, a compact multi-purpose nanomanipulator for use inside the electron microscope was constructed, that is described in Chapter 3. This was followed by a patent application and hopefully the commercialization into a commercial product,[70] as the techniques developed and used for electron source fabrication proved to be useful for other applications as well, like high aspect-ratio probes for AFM studies on rough surfaces, electrochemical probes and manipulation of single spin nano-objects to build quantum bit circuits.[71]

To end this short summary of obtained results, single, closed CNT field emitters are being used now to study the fundamental limit on brightness imposed by the Pauli exclusion principle.[72] The goal of this research, performed at Vanderbilt University, is to obtain a quantum degenerate electron beam, where the entire phase space is filled with electrons.

1.7 Layout of this thesis

This thesis contains the following chapters:

Chapter 1	Introduction
Chapter 2	Theory of electron field emission and of the field emission microscope – the instrument used to record electron beam profiles
Chapter 3	Nanomanipulator – design, construction, specifications and applications of the device to produce microscopy probes within the SEM
Chapter 4	Mounting Techniques – how we enhance our probes using nano-objects
Chapter 5	Closing Experiments – experiments to close a cut MWNT and to re-graphitize its cap to obtain emission from local emission sites
Chapter 6	Closed MWNTs – experiments on unmodified, closed capped MWNTs
Chapter 7	Nanowires – characterization of the field emission properties of these structures and analysis of their structure and morphology

afterwards using TEM and EDX

References

1. R. F. Egerton *Physical Principles of Electron Microscopy: An Introduction to TEM, SEM, and AEM*. Springer, (2005).

2. D. J. Griffiths *Introduction to Electrodynamics*. Prentice-Hall, New Jersey (1999).

3. H. H. Rose. Optics of high-performance electron microscopes. *Science and Technology of Advanced Materials* **9**, 014107 (2008).

4. P. D. Nellist, M. F. Chisholm, N. Dellby, O. L. Krivanek, M. F. Murfitt, Z. S. Szilagyi, A. R. Lupini, A. Borisevich, W. H. Sides Jr. and S. J. Pennycook. Direct Sub-Angstrom Imaging of a Crystal Lattice. *Science* **305**, 1741 (2004).

5. Richard Young, Todd Templeton, Laurent Roussel, Ingo Gestmann, Gerard van Veen, Trevor Dingle and Sander Henstra. Extreme High-Resolution SEM: A Paradigm Shift. *Microscopy Today* **16**, 24-28 (2010).

6. FEI website, *http://www.fei.com/products/sem/nova-nanosem/*

7. Hitachi website, *http://hitachi-hta.com/products/electron-microscopes-and-focused-ion-beam/field-emission-sem/su9000-uhr-fe-sem*

8. R. Erni, M. D. Rossell, C. Kisielowski and U. Dahmen. Atomic-Resolution Imaging with a Sub-50-pm Electron Probe. *Physical Review Letters* **102**, 096101 (2009).

9. H. Müllejans and J.Bruley. Electron energy-loss spectroscopy (EELS) ; comparison with X-ray analysis. *J. Phys. IV France* **03**, C7-2083 (1993).

10. R. F. Egerton. Electron energy-loss spectroscopy in the TEM. *Reports on*

Progress in Physics **72**, 016502 (2009).

11. D. R. S. Cumming, S. Thoms, S. P. Beaumont and J. M. R. Weaver. Fabrication of 3 nm wires using 100 keV electron beam lithography and poly(methyl methacrylate) resist. *Applied Physics Letters* **68**, 322-324 (1996).

12. E. Slot, M. J. Wieland, G. de Boer, P. Kruit, G. F. ten Berge, A. M. C. Houkes, R. Jager, T. van de Peut, J. J. M. Peijster, S. W. H. K. Steenbrink, T. F. Teepen, A. H. V. van Veen and B. J. Kampherbeek. MAPPER: high throughput maskless lithography. *Emerging Lithographic Technologies XII* **6921**, 69211P-9 (2008).

13. S. Flügge (Ed.) R. H. Good and E. W. Müller *Handbuch der Physik, XXI*. Springer Verlag, Berlin (1956).

14. A. R. Lupini and S. J. Pennycook. Localization in elastic and inelastic scattering. *Ultramicroscopy* **96**, 313-322 (2003).

15. FEI website, *http://www.fei.com/products/sem/verios-xhr/*

16. D. J. Griffiths *Introduction to Quantum Mechanics*. Prentice-Hall, New Jersey (1995).

17. P. W. Hawkes and E. Kasper *Principles of electron optics*. Academic Press, London (1989).

18. Jon Orloff (Ed.) *Handbook of Charged Particle Optics*. CRC Press, Boca Raton (1997).

19. N. de Jonge. Carbon nanotube field emitters for electron microscopes. *Philips Research Technical Note* **PR-TN2001/251** (2001).

20. L. W. Swanson and G. A. Schwind. A Review of the Zr/O Schottky Cathode *in Handbook of charged particle optics*. J. Orloff (ed.), CRC Press, New York, 77-102 (1997).

21. M. Doytcheva, M. Kaiser and N. de Jonge. In situ transmission electron microscopy investigation of the structural changes in carbon nanotubes during electron emission at high currents. *Nanotechnology* **17**, 3226-3233 (2006).

22. S. Iijima. Helical microtubules of graphitic carbon. *Nature* **354**, 56-58 (1991).

23. M. Monthioux and V. L. Kuznetsov. Who should be given the credit for the discovery of carbon nanotubes? *Carbon* **44**, 1621-1623 (2006).

24. S. Iijima and T. Ichihashi. Single-shell carbon nanotubes of 1-nm diameter. *Nature* **363**, 603-605 (1993).

25. D. S. Bethune, C. H. Klang, M. S. de Vries, G. Gorman, R. Savoy, J. Vazquez and R. Beyers. Cobalt-catalysed growth of carbon nanotubes with single-atomic-layer walls. *Nature* **363**, 605-607 (1993).

26. B. Q. Wei, R. Vajtai and P. M. Ajayan. Reliability and current carrying capacity of carbon nanotubes. *Applied Physics Letters* **79**, 1172-1174 (2001).

27. Z. Yao, C. L. Kane and C. Dekker. High-Field Electrical Transport in Single-Wall Carbon Nanotubes. *Physical Review Letters* **84**, 2941 (2000).

28. B. I. Yakobson and P. Avouris. Mechanical Properties of Carbon Nanotubes *in Carbon Nanotubes Synthesis, Structure, Properties and Applications*. M. S. Dresselhaus, G. Dresselhaus & P. Avouris (eds.), Springer-Verlag, Berlin, 287-327 (2001).

29. L. Forró and C. Schönenberger. Physical Properties of Multi-wall Nanotubes *in Carbon Nanotubes Synthesis, Structure, Properties and Applications*. M. S. Dresselhaus, G. Dresselhaus & P. Avouris (eds.), Springer-Verlag, Berlin, 329-390 (2001).

30. N. de Jonge. Carbon nanotube electron sources for electron microscopes. *Advances in Imaging & Electron Physics* **156**, 203-233 (2009).

31. M. S. Dresselhaus and M. Endo. Relation of Carbon Nanotubes to Other Carbon Materials *in Carbon Nanotubes Synthesis, Structure, Properties and Applications*. M. S. Dresselhaus, G. Dresselhaus & P. Avouris (eds.), Springer-Verlag, Berlin, 11-28 (2001).

32. P. M. Ajayan and O. Zhou. Applications of Carbon Nanotubes *in Carbon Nanotubes Synthesis, Structure, Properties and Applications*. M. S. Dresselhaus, G. Dresselhaus & P. Avouris (eds.), Springer-Verlag, Berlin, 391-425 (2001).

33. A. Kis, G. Csanyi, J. P. Salvetat, T. N. Lee, E. Couteau, A. J. Kulik, W. Benoit, J. Brugger and L. Forro. Reinforcement of single-walled carbon nanotube bundles by intertube bridging. *Nat Mater* **3**, 153-157 (2004).

34. P. M. Ajayan and F. Banhart. Nanotubes: Strong bundles. *Nat Mater* **3**, 135-136 (2004).

35. H. W. Kroto, J. R. Heath, S. C. O'Brien, R. F. Curl and R. E. Smalley. C60: Buckminsterfullerene. *Nature* **318**, 162-163 (1985).

36. R. Saito, G. Dresselhaus and M. S. Dresselhaus *Physical properties of carbon nanotubes*. Imperial College Press, London (1998).

37. S. Iijima, T. Ichihashi and Y. Ando. Pentagons, heptagons and negative curvature in graphite microtubule growth. *Nature* **356**, 776-778 (1992).

38. T. W. Odom, J.-L. Huang, P. Kim and C. M. Lieber. Structure and Electronic Properties of Carbon Nanotubes. *J. Phys. Chem. B* **104**, 2794-2809 (2000).

39. N. de Jonge, M. Doytcheva, M. Allioux, M. Kaiser, S. A. M. Mentink, K. B. K. Teo, R. G. Lacerda and W. I. Milne. Cap Closing of Thin Carbon Nanotubes. *Adv. Mater.* **17**, 451-455 (2005).

40. S. G. Louie. Electronic Properties, Junctions, and Defects of Carbon Nanotubes *in Carbon Nanotubes Synthesis, Structure, Properties and Applications*. M. S. Dresselhaus, G. Dresselhaus & P. Avouris (eds.), Springer-Verlag, Berlin, 113-145 (2001).

41. B. Bourlon, C. Miko, L. Forró, D. C. Glattli and A. Bachtold. Determination of the Intershell Conductance in Multiwalled Carbon Nanotubes. *Physical Review Letters* **93**, 176806 (2004).

42. J. C. Charlier, X. Blase and S. Roche. Electronic and transport properties of nanotubes. *Rev. Mod. Phys.* **79**, 677 (2007).

43. La Sportiva ski's, *http://www.sportiva.com/resources/images/Product_Images/TechSheets/VaporNano_techsheet.pdf*

44. Review on BMC bicycle using Easton CNT technology, *http://www.pezcyclingnews.com/page/tech-n-spec/?id=88739*

45. Easton CNT bat commercial, *http://www.youtube.com/watch?v=ORWyDSluw8g*

46. L. Xiao, Z. Chen, C. Feng, L. Liu, Z. Q. Bai, Y. Wang, L. Qian, Y. Zhang, Q. Li, K. Jiang and S. Fan. Flexible, Stretchable, Transparent Carbon Nanotube Thin Film Loudspeakers. *Nano Lett.* **8**, 4539-4545 (2008).

47. Zyvex sports case studies, *http://www.zyvextech.com/sports*

48. Q. Wen, W. Qian, J. Nie, A. Cao, G. Ning, Y. Wang, L. Hu, Q. Zhang, J. Huang and F. Wei. 100 mm Long, Semiconducting Triple-Walled Carbon Nanotubes. *Adv. Mater.* **22**, 1867-1871 (2010).

49. M. Zhang, K. R. Atkinson and R. H. Baughman. Multifunctional Carbon Nanotube Yarns by Downsizing an Ancient Technology. *Science* **306**, 1358-1361 (2004).

50. K. Jiang, Q. Li and S. Fan. Nanotechnology: Spinning continuous carbon nanotube yarns. *Nature* **419**, 801 (2002).

51. H. W. C. Postma, T. Teepen, Z. Yao, M. Grifoni and C. Dekker. Carbon Nanotube Single-Electron Transistors at Room Temperature. *Science* **293**, 76-79 (2001).

52. B. Lassagne, D. Garcia-Sanchez, A. Aguasca and A. Bachtold. Ultrasensitive Mass Sensing with a Nanotube Electromechanical Resonator. *Nano Lett.* **8**, 3735-3738 (2008).

53. K. Jensen, J. Weldon, H. Garcia and A. Zettl. Nanotube Radio. *Nano Lett.* **7**, 3508-3511 (2007).

54. M. H. van Es. A new touch to atomic force microscopy: smart probing of biological and biomedical systems at the nanoscale. Ph.D. thesis, Leiden University (2008).

55. A. J. Katan and T. H. Oosterkamp. Measuring Hydrophobic Interactions with Three-Dimensional Nanometer Resolution. *J. Phys. Chem. C* **112**, 9769-9776 (2008).

56. A. V. Patil, A. F. Beker, F. G. M. Wiertz, H. A. Heering, G. C. Coslovich,

R. Vlijm and T. H. Oosterkamp. Fabrication and characterization of polymer insulated carbon nanotube modified electrochemical nanoprobes. *Nanoscale* **2**, 734-738 (2009).

57. M. J. Fransen. Towards high-brightness, monochromatic electron sources. Delft University of Technology (1998).

58. P. Kim, T. W. Odom, J.-L. Huang and C. Lieber. Electronic Density of States of Atomically Resolved Single-Walled Carbon Nanotubes: Van Hove Singularities and End States. *Phys. Rev. Lett.* **82**, 1225-1228 (1999).

59. A. G. Rinzler, J. H. Hafner, P. Nikolaev, P. Nordlander, D. T. Colbert, R. E. Smalley, L. Lou, S. G. Kim and D. Tomanek. Unraveling Nanotubes: Field Emission from an Atomic Wire. *Science* **269**, 1550-1553 (1995).

60. Y. Saito, K. Hata and T. Murata. Field Emission Patterns Originating from Pentagons at the Tip of a Carbon Nanotube. *Jpn. J. Appl. Phys.* **39**, L271-L272 (2000).

61. Charles Kittel *Introduction to Solid State Physics*. John Wiley & Sons, New York (1996).

62. N. de Jonge, M. Allioux, M. Doytcheva, M. Kaiser, K. B. K. Teo, R. G. Lacerda and W. I. Milne. Characterization of the field emission properties of individual thin carbon nanotubes. *Appl. Phys. Lett.* **85**, 1607-1609 (2004).

63. K. A. Dean and B. R. Chalamala. Field emission microscopy of carbon nanotube caps. *Journal of Applied Physics* **85**, 3832-3836 (1999).

64. K. A. Dean and B. R. Chalamala. Experimental studies of the cap structure of single-walled carbon nanotubes. *J. Vac. Sci. Technol. B* **21**, 868-871 (2003).

65. K. Hedberg, L. Hedberg, D. S. Bethune, C. A. Brown, H. C. Dorn, R. D. Johnson and M. De Vries. Bond Lengths in Free Molecules of Buckminsterfullerene, C60, from Gas-Phase Electron Diffraction. *Science* **254**, 410-412 (1991).

66. A. De Vita, J. C. Charlier, X. Blase and R. Car. Electronic structure at carbon nanotube tips. *Appl. Phys. A: Mater. Sci. Process.* **68**, 283-286 (1999).

67. M. Khazaei, K. A. Dean, A. A. Farajian and Y. Kawazoe. Field Emission Signature of Pentagons at Carbon Nanotube Caps. *J. Phys. Chem. C* **111**, 6690-6693 (2007).

68. K. Hata, A. Takakura, K. Miura, A. Ohshita and Y. Saito. Interference fringes observed in electron emission patterns of a multiwalled carbon nanotube. *J. Vac. Sci. Technol. B* **22**, 1312-1314 (2004).

69. C. Oshima, K. Mastuda, T. Kona, Y. Mogami, M. Komaki, Y. Murata, T. Yamashita, T. Kuzumaki and Y. Horiike. Young's Interference of Electrons in Field Emission Patterns. *Phys. Rev. Lett.* **88**, 038301 (2002).

70. D. J. van der Zalm, E. C. Heeres, M. B. S. Hesselberth, A. J. Katan, and M. H. van Es. A nano-scale manipulator. U.K.Patent Application GB0908780.0 (2010)

71. T. van der Sar, E. C. Heeres, G. M. Dmochowski, G. de Lange, L. Robledo, T. H. Oosterkamp and R. Hanson. Nanopositioning of a diamond nanocrystal containing a single nitrogen-vacancy defect center. *Appl. Phys. Lett.* **94**, 173104-3 (2009).

72. J. D. Jarvis, H. L. Andrews, B. Ivanov, C. L. Stewart, N. de Jonge, E. C. Heeres, W. P. Kang, Y. M. Wong, J. L. Davidson and C. A. Brau. Resonant tunneling and extreme brightness from diamond field emitters

and carbon nanotubes. *J. Appl. Phys.* **108**, 094322-094326 (2010).

2

Theory of electron emitters

A theoretical background of electron field emission is given in this chapter. We describe the Fowler-Nordheim field emission model for metals and discuss its limitations. The field emission microscope, the setup that was used for some of our experiments, is also presented and its features are explained, such as its magnification – which are necessary to interpret field emission patterns obtained with this setup.

2.1 Fowler-Nordheim field emission model

To obtain equations for the field emission current density and for the field emission energy distribution we follow the derivations by Hawkes and Kasper[1] in this and in the following sections. Within the Fowler-Nordheim field emission model, the conduction electrons in the metallic emitter are considered as non-interacting particles, as is the case in an ideal free electron gas. The electrons in a free electron gas obey Fermi-Dirac statistics – only two electrons with oppositely directed spins can occupy the same state (Pauli exclusion principle).
The Fermi-Dirac distribution function for such particles reads:

$$f\left(E,T\right)=\frac{1}{e^{\frac{E-\zeta}{k_{\mathrm{B}}T}}+1} \tag{2.1}$$

where E is the energy, ζ the Fermi energy, k_{B} Boltzmann's constant, and T the absolute temperature. To describe electron emission from the surface of an emitter, we define a Cartesian coordinate system $\left(x,y,z\right)$ as follows: the x and y axes run parallel to the emitter surface and the z axis points in the direction normal to the emitter surface, see Figure 2.1. We can write the electron density in phase space as $\rho^{*}\left(\mathbf{r}^{*}\right)$ where the phase space vector $\mathbf{r}^{*}=\left(\mathbf{r},\mathbf{p}\right)=\left(x,y,z,p_{x},p_{y},p_{z}\right)$. In every phase space volume h^3, where h is Planck's constant, two states exist. So the electron density can be written as:

$$\rho^{*}\left(\mathbf{r}^{*}\right)=\frac{2}{h^{3}}f\left(E,T\right)D\left(\mathbf{r}^{*}\right)=\frac{2}{h^{3}}\frac{1}{e^{\frac{E-\zeta}{k_{\mathrm{B}}T}}+1}D\left(\mathbf{r}^{*}\right) \tag{2.2}$$

using the Fermi-Dirac distribution of Equation (2.1) and a transmission factor D, describing the emission. The transmission factor $D=1$ inside the emitter and $D<1$ outside the emitter.
Writing down the Hamiltonian:

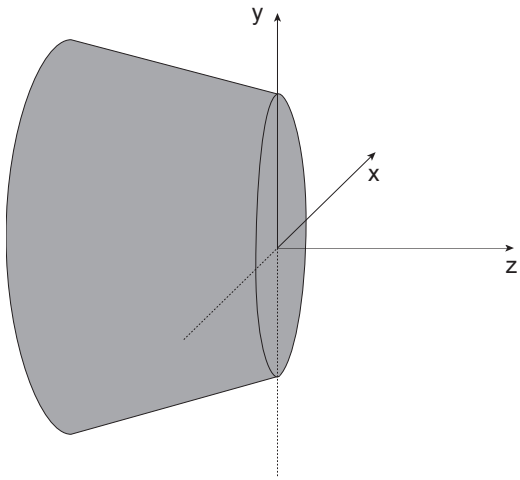


Figure 2.1 The Cartesian coordinate system for our electron emitter. The tip (grey) has an emitting surface parallel to the *xy*-plane. In the model we use, electron emission is considered to originate from this plane only.

$$E = H\left(\mathbf{r}^*\right) = \frac{1}{2m}\left(\mathbf{p} + e\mathbf{A}\left(\mathbf{r}\right)\right)^2 + V\left(\mathbf{r}\right) \tag{2.3}$$

which can be simplified by assuming no magnetic fields and $\mathbf{A} = 0$, and by assuming the potential V is a one-dimensional function of z. Now the total energy E can be written as:

$$E = \frac{{p_x}^2 + {p_y}^2 + {p_z}^2}{2m} + V\left(\mathbf{r}\right) = \left(\frac{{p_x}^2 + {p_y}^2}{2m}\right) + \left(\frac{{p_z}^2}{2m} + V\left(z\right)\right) = E_t + E_n \tag{2.4}$$

As indicated, the total energy has a transverse and a normal part, E_t and E_n, respectively. The potential energy inside the metal is constant, and we choose to define it as zero there. Outside the metal in the vacuum, a potential barrier with height ϕ exists, where ϕ is the work function. If an electric field in the z-direction is applied, the potential barrier will be lowered as a function of the distance from the tip, z. Assuming the electric field in the vicinity of the tip has a constant value

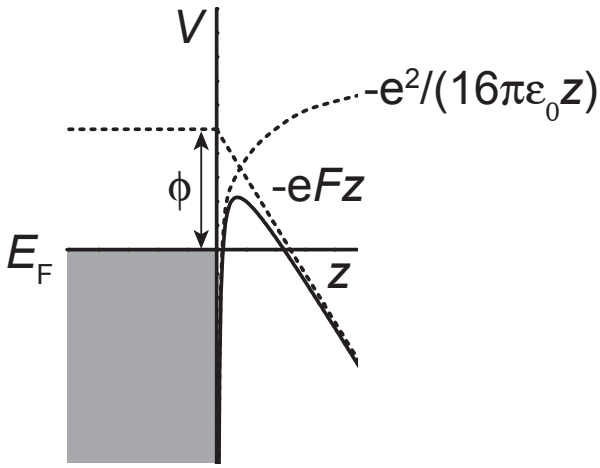


Figure 2.2 Potential (solid black curve) as a function of distance from the tip. The zero potential is chosen to coincide with the Fermi energy E_F.

F, we can write down the expression for the potential energy due to this field:

$$\begin{aligned} V_{\text{field}} &= 0 \qquad z < 0 \\ V_{\text{field}} &= -eFz \qquad z \geq 0 \end{aligned} \tag{2.5}$$

Furthermore, if an electron leaves the tip it feels the force of an image charge located at the same distance inside the tip; as if being in the electric field of a charge $+e$ at a distance $2z$. The potential energy of this configuration $V_{\text{image}} = -e^2/(4\pi\varepsilon_0 4z)$, which is also represented in Figure 2.2.[2] Now the total potential energy is a sum of all contributions and reads:

$$\begin{aligned} V(z) &= 0 && z < 0 \\ V(z) &= \phi + V_{\text{field}} + V_{\text{image}} = \phi - eFz - \frac{e^2}{16\pi\varepsilon_0 z} && z > 0 \end{aligned} \tag{2.6}$$

as we choose the Fermi energy level inside the tip at zero.

For any classical observable $K^*(\mathbf{r}^*)$ its three dimensional distribution function $K(\mathbf{r})$ is obtained by integrating over the entire momentum range:

$$K(\mathbf{r}) = \iiint K^*(\mathbf{r}^*)\rho^*(\mathbf{r}^*)\,d^3\mathbf{p} \tag{2.7}$$

2.2 Field emission current density

Using Equation (2.7) a current density can be obtained by calculating the expectation value of $\mathbf{K}^* = e\mathbf{v} = e\,\mathbf{p}/m$:

$$\mathbf{j}(\mathbf{r}) = \frac{e}{m}\iiint \mathbf{p}\rho^*(\mathbf{r}^*)\,d^3\mathbf{p} = \frac{2e}{mh^3}\iiint \mathbf{p}f(E,T)D(\mathbf{r}^*)\,d^3\mathbf{p} \tag{2.8}$$

We now assume the emission is in the *z*-direction only, so the current density is obtained as the expectation value of $K = ev_z = e\,p_z/m$. Furthermore, for field emission the transmission function is a function of the normal energy only:

$$\begin{aligned}\mathbf{j}(\mathbf{r}) = j_z\hat{z} &= \frac{2e\hat{z}}{mh^3}\iiint p_z f(E,T)D(\mathbf{r}^*)\,dp_x dp_y dp_z \\ &= \frac{2e\hat{z}}{mh^3}\iiint p_z f(E,T)D(E_n)\,dp_x dp_y dp_z\end{aligned} \tag{2.9}$$

To evaluate this integral, we perform the following coordinate transformation to obtain a representation in cylindrical coordinates (E_t, γ, E_n), where γ is the angle between the transverse momentum and p_x:

$$
\begin{aligned}
p_x &= \sqrt{2mE_t}\cos\gamma \\
p_y &= \sqrt{2mE_t}\sin\gamma \\
p_z &= \sqrt{2m\left(E_n - V\left(z\right)\right)} \\
dp_x dp_y dp_z &= \frac{m^2}{p_z} dE_t d\gamma dE_n
\end{aligned}
\tag{2.10}
$$

By integrating over all possible values for $\left(E_t, \gamma\right)$, we are left with an expression for the current density, where we still need to integrate over E_n:

$$
j_z = \frac{4\pi mekT}{h^3} \int_{-\infty}^{\infty} D\left(E_n\right) \ln\left(1 + e^{\frac{\zeta - E_n}{kT}}\right) dE_n \tag{2.11}
$$

The transmission function $D\left(E_n\right)$ can be found by using the WKB approximation for the solution to the Schrödinger equation:[3,4]

$$
D\left(E_n\right) = e^{-\frac{4}{3\hbar eF}\sqrt{2m\left(\phi - E_n\right)^3} v(w)} \tag{2.12}
$$

As a part of this solution two elliptic functions $v\left(w\right)$ and $t\left(w\right)$ are introduced, which are functions of the Nordheim parameter w (here I chose not to use the commonly used symbol *y*, as we already use that in our coordinate system). The equation above can be simplified by using a Taylor series expansion around the Fermi level, which was chosen to coincide with the origin of our coordinate system, see Figure 2.2. By doing this, we can write:

$$
D\left(E_n\right) \approx e^{-c + \frac{E_n}{d}} \tag{2.13}
$$

The dimensionless parameter *c* is introduced to further simplify this equation, and its value reads:

$$c = \frac{4\sqrt{2m\phi^3}}{3\hbar eF} v(w) \tag{2.14}$$

The other parameter *d*, an energy, is the so-called tunneling parameter:

$$d = \frac{\hbar eF}{2t(w)\sqrt{2m\phi}} = c_4 \frac{F}{t(w)\sqrt{\phi}} \tag{2.15}$$

The functions $t(w)$ and $v(w)$ can be approximated by:[1]

$$\begin{aligned} v(w) &= 1 - w^{1.69} \\ t(w) &= 1 + 0.1107 \cdot w^{1.33} \end{aligned} \tag{2.16}$$

where *w* is given as:

$$w = \frac{\left(e^3 F / 4\pi\varepsilon_0\right)^{1/2}}{\phi} = \frac{\left(c_3 F\right)^{1/2}}{\phi} \tag{2.17}$$

The transmission function is substituted in Equation (2.9) and after integration an expression for the field emission current density at zero temperature is obtained:[1,4]

$$j_z = \frac{4\pi me}{h^3} d^2 e^{\left(\frac{-2v(w)\phi}{3t(w)d}\right)} = \frac{e^3 F^2}{8\pi h t^2(w)\phi} e^{\left(\frac{-4v(w)\phi^{3/2}\sqrt{2m}}{3\hbar eF}\right)} \tag{2.18}$$

Using the notation by de Jonge,[5] this equation can be simplified further into:

$$j_z = \frac{c_1 F^2}{b_1^{\,2}\phi} e^{\left(\frac{c_2 a_2 c_3}{\phi^{1/2}}\right)} e^{\left(-\frac{c_2 a_1 \phi^{3/2}}{F}\right)}$$
$$c_1 = \frac{e^3}{8\pi h} \qquad (2.19)$$
$$c_2 = \frac{8\pi\sqrt{2m}}{3he}$$
$$c_3 = \frac{e^3}{4\pi\varepsilon_0}$$

Where the functions *v* and *t* have been approximated by a quadratic function and by a constant:

$$v(w) = a_1 - a_2 w^2 \qquad (2.20)$$
$$t(w) = b_1$$

Values for the constants a_1, a_2 and b_1 are derived from experimental conditions, such as the electric field strength.

2.3 Field emission energy distribution

We can use Equation (2.9) to derive an expression for the total energy distribution *J(E)* of the emitted electrons. To do so, this integral can be rewritten by using a spherical representation of the momenta using the coordinates (E, γ, θ), with θ the angle between the total momentum and p_z:

$$p_x = \sqrt{2m\left(E - V(z)\right)}\sin\theta\cos\gamma$$
$$p_y = \sqrt{2m\left(E - V(z)\right)}\sin\theta\sin\gamma \qquad (2.21)$$
$$p_z = \sqrt{2m\left(E - V(z)\right)}\cos\theta$$
$$dp_x dp_y dp_z = m\sqrt{2me}\sin\theta dE d\gamma d\theta$$

After integration over (γ,θ) and simplification, we obtain:

$$j=\int J(E)dE=\int \frac{4\pi med}{h^3}\frac{e^{\frac{E}{d}}}{1+e^{\frac{E}{k_BT}}}e^{-\frac{4v(w)\sqrt{2m}}{3\hbar eF}\phi^{3/2}}dE \tag{2.22}$$

For a complete derivation, see the work by Hawkes and Kasper,[1] or Gadzuk and Plummer.[3] Finally, the following total energy distibution expression is obtained, which is used throughout this thesis to evaluate the measured energy spectra of our electron sources:

$$J(E)\propto \frac{e^{\frac{E}{d}}}{1+e^{\frac{E}{k_BT}}} \tag{2.23}$$

2.4 Distribution of transverse energies

From Equation (2.7) the distribution of transverse energies can also be obtained by integrating over all normal momentum values:[1]

$$D(E_{transverse})=\int \frac{ep_z}{m}f(E,T)D(E_n)dp_z \tag{2.24}$$

Hence we have:

$$d^2j=D(E_{transverse})dp_xdp_y=dp_xdp_y\int \frac{ep_z}{m}\frac{1}{e^{\frac{E}{k_BT}}+1}e^{-c+\frac{E_n}{d}}dp_z \tag{2.25}$$

Changing integration from dp_z into dE_n using the following transformation:

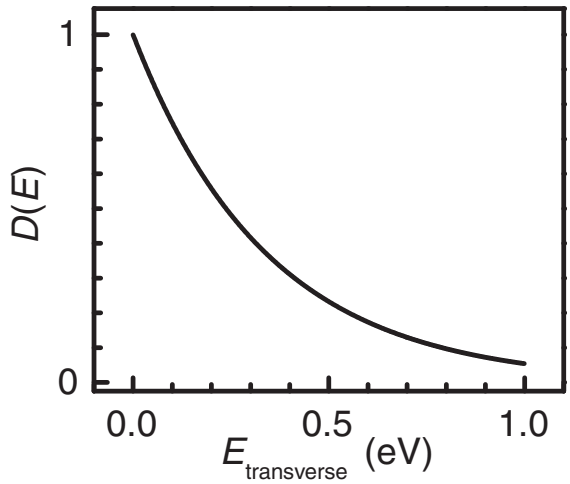


Figure 2.3 Transverse energy distribution function $D(E_{\text{transverse}})$.

$$E_n = \frac{p_z^{\,2}}{2m} + V(z),\ dE_n = \frac{p_z}{m} dp_z \tag{2.26}$$

we obtain:

$$d^2 j = D\left(E_{transverse}\right) dp_x dp_y = dp_x dp_y \int e \frac{1}{\frac{E_n + E_{\text{transverse}}}{e^{k_B T}} + 1} e^{-c + \frac{E_n}{d}} dE_n \tag{2.27}$$

Integration over the normal energy range yields the transverse energy distribution $D\left(E_{\text{transverse}}\right)$:

$$D\left(E_{transverse}\right) \sim e^{-E_{\text{transverse}}/d} \tag{2.28}$$

So the transverse momentum distribution is a Gaussion function, because:

$$E_{\text{transverse}} = \frac{1}{2m}\left(p_x{}^2 + p_y{}^2\right) \tag{2.29}$$

The average value of the transverse energy equals:

$$\left\langle E_{\text{transverse}} \right\rangle = \frac{\int E_{\text{transverse}} D\left(E_{\text{transverse}}\right) dE_{\text{transverse}}}{\int D\left(E_{\text{transverse}}\right) dE_{\text{transverse}}} = d \tag{2.30}$$

For a specific field emitter tip, with d = 0.34 eV, the transverse energy distribution was calculated and is shown in Figure 2.3. The parameter values were obtained from field emission measurements and numerical simulations of the tip. Having obtained the transverse energy distribution function, it is possible to calculate the electron beam profile up to the screen semi-classically, if the electron paths as a function of transverse energy are known. This will be done in Chapter 6, and will enable us to relate the observed emission pattern to the emitting area at the tip.

2.5 Limitations of the Fowler-Nordheim theory

Some assumptions that were made in the Fowler-Nordheim model should be reconsidered with a carbon nanotube as emitter in mind. These are the metallic density of states, the planar surface of emission – which only takes into account the z-direction dependence, and the work function, which is assumed constant over the entire emission area.

A CNT emitter is expected to have localized emission sites,[6] that have a high local density of states.[7] As we will show in Chapter 6, these sites originate from a single emitting CNT and interference fringes can appear between the corresponding spots from such sites on an imaging screen. The problem of a curved emitter surface was addressed by Edgcombe and de Jonge,[8] but up until now the Fowler-Nordheim field emission model for metals, as described above, was used successfully to derive several parameters of the CNT emitters, like workfunction ϕ, emitter radius

R, field factor β , and tunneling parameter d.

2.6 Field emission microscopy

Various aspects of the field emission microscope – used to record an emitted electron beam to image the electron emitting surface (field emission pattern) – will be treated in the remainder of this chapter.

2.6.1 Field emission patterns

In 1936 the field emission microscope (FEM) was invented by Erwin Müller.[9,10] The FEM produces a magnified image of the emitting surface – without the need for lenses – and the electronic structure of the emitter can be studied with near atomic resolution. An image of the electronic structure of the emitter (cathode) is obtained by extracting an electron beam using a sufficiently large electric field to obtain field emission in vacuum. Most often a phosphor screen is used to generate a visible image of the beam, which can then be recorded with a camera. One drawback of this technique is that the magnification is usually not known a priory, unless additional information about the emitting tip is known. Local variations in morphology of the emitter can cause an inhomogeneous transformation of the electronic structure on the tip into the image on the screen. However, it is still possible to retrieve information about the local structure of the emitter, such as crystal structure,[11-13] cleanness,[11,14] etc.. Due to the low mass of an electron, the maximum obtainable resolution of the resulting image on the screen is limited by the transverse electron energy distribution and by diffraction effects.[15]

To overcome these problems, it is possible to obtain a higher resolution image by employing an ion beam originating from a sharp tip, Field Ionization Microscopy (FIM), also invented by Müller.[15,16] By changing the polarity of the field and supplying an imaging gas in the vacuum chamber, gas molecules adsorbed at the emitter can be ionized and the positively charged ions are accelerated towards the screen. The ionization rate at the position of the atoms of the tip, especially at step edges, is higher than at other positions. Because of this and the fact that the ions have a larger mass compared to electrons, and hence suffer less from diffraction,

atoms could be resolved for the first time.

To study the properties of tips as field emission sources, we only used field emission microscopy to obtain information on the local electronic structure of the emitter. By performing in-situ FEM experiments, the stability of this emitter can be tested and studied in several ways: e.g. its annealing behavior, adsorption of various contaminants, and the extent to which a tip can withstand high fields and high current densities. For instance, a nanotube field emitter can be open or closed, and can have an amorphous or a crystalline cap. The FEM is an important tool to check whether the emitter has been fabricated correctly, and whether it is possible to even control the shape and electronic structure of the emitter in a desired way.

To draw conclusions from field emission patterns, one should know two things. First, the magnification of the setup has to be known, to establish how a distance on the emitter converts to a distance on the screen. Second, it is useful to determine the theoretical resolution of the FEM in order to verify what the smallest structure is one can identify. Sometimes, claims about the atomic structure of emitters are made, without addressing both points describe above. For instance, atomic structure has been claimed to be observed, in cases where the overall scale of the entire image does not seem to correspond at all with this observation. In this part of the chapter an important point will be addressed to be able to use the FEM and to draw conclusions from FEM patterns. The magnification of the field emission microscope, which determines the image size on the screen with respect to the size of emission sites on the tip, will be treated in *Section 2.6.3*. As this magnification depends on the actual emitter morphology, it is essential to know the emitter morphology. This is why an emitter consisting of a sharp tip with only one CNT is needed.

2.6.2 Electron trajectories

For non-spherically symmetric emitters, it is hard to find analytical solutions to the equations of motion. To calculate the electron trajectories for such geometries, the EMECH software included in the numerical package MEBS has been used

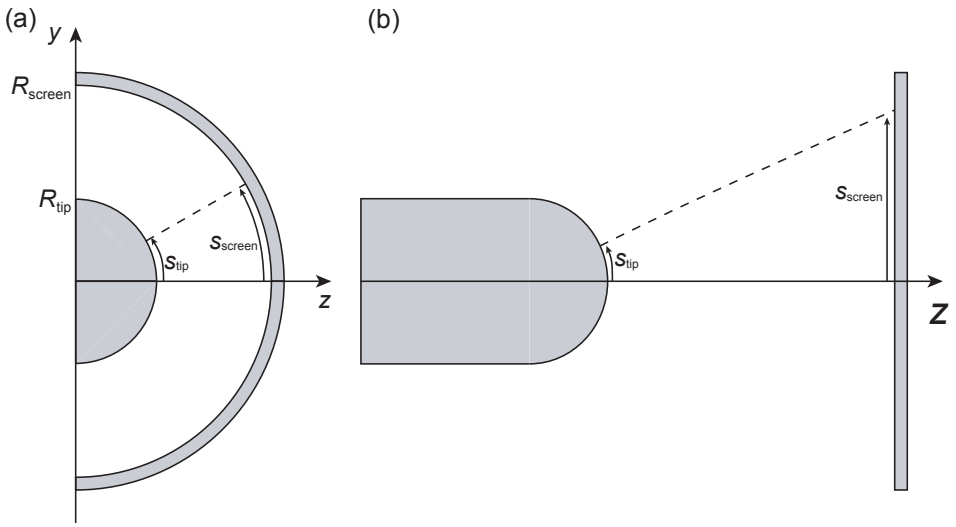


Figure 2.4 Models used to calculate the magnification of a field emission microscope using electron trajectories. Drawings are not scaled properly for clarity. (a) Simple two concentric spheres model, where the emitter has radius R_{tip} and the extractor (screen) has radius R_{screen}, assuming spherical symmetry. The dashed line indicates the electron trajectory of an electron leaving the tip at a distance s_{tip} from the *z*-axis, measured along the emitter surface, and hitting the screen at a distance s_{screen} from the y-axis. (b) Enhanced model consisting of a cylindrically shaped emitter and a planar extractor, assuming cylindrical symmetry along the longitudinal *z*-axis.

throughout this thesis.[17] In this way, the electron trajectories starting near the tip and landing on a screen as a function of transverse energy could be found, where the tip and screen were simulated using axial symmetry.

2.6.3 Magnification of the field emission microscope

The magnification of the field emission microscope for the simple case of two concentric spheres – i.e. a spherically shaped emitter inside a spherically shaped extractor which serves as a screen – and electrons with zero transverse energy is simply the division of the two radii: $M = R_{screen} / R_{tip}$, this layout is depicted in Figure 2.4a. Changing the shape of either the emitter or the extractor yields a different magnification. This magnification was calculated by Good & Müller for several different tip shapes[4], however, for a carbon nanotube emitter the shape

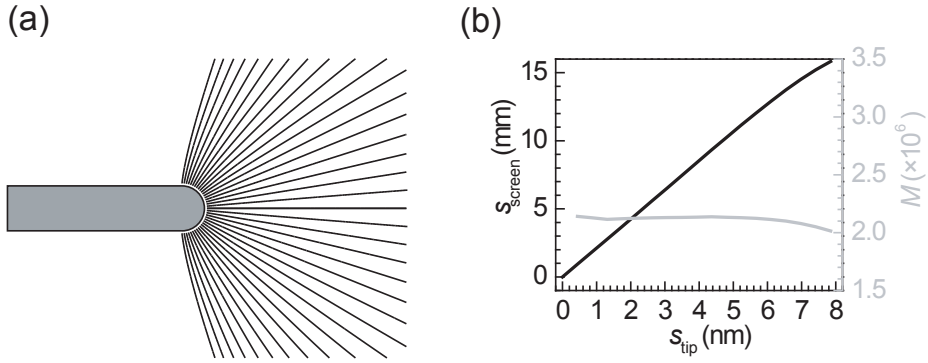


Figure 2.5 (a) Model of the carbon nanotube with electron trajectories from different starting positions. (b). Left axis: landing position of the electron as a function of the initial position with respect to the longitudinal symmetry axis of the system. Right axis: magnification of the emitter MWNT #1 as a function of the initial position.

and hence calculating the magnification analytically is more complex, because of the large aspect ratio of the CNT. Using a numerical simulation of a model of the carbon nanotube on a support tip, the magnification of the experimentally used setup was calculated. The rays were simulated to start 0.5 nm outside the nanotube cap, as this approximately equals the expected potential barrier width, as the electric field strength $E \sim 9\,\mathrm{V/nm}$ at the nanotube cap and assuming the potential barrier equals the nanotube work function of 5.1 eV. This is a quite simplistic approximation, but varying the starting position by a factor two did not change the electron traces significantly. The magnification was then calculated by dividing the radial position on the screen, s_{screen}, by the distance from the center of the cap, s_{tip}, as is illustrated in Figure 2.4b. The cap of the carbon nanotube was modeled as a hemisphere. From several different starting positions on this hemisphere electron rays were simulated, see Figure 2.5. For the carbon nanotube sample MWNT #1, a magnification of 2.1×10^6 was obtained, see Figure 2.5b. Over the entire hemisphere the calculated magnification did not vary more than 10 %, resulting in a magnification $M = \left(2.1 \pm 0.1\right)\times10^6$.

References

1. P. W. Hawkes and E. Kasper *Principles of electron optics*. Academic Press, London (1989).

2. D. J. Griffiths *Introduction to Electrodynamics*. Prentice-Hall, New Jersey (1999).

3. J. W. Gadzuk and E. W. Plummer. Field Emission Energy Distribution (FEED). *Rev. Mod. Phys.* **45**, 487 (1973).

4. S. Flügge (Ed.) R. H. Good and E. W. Müller *Handbuch der Physik, XXI*. Springer Verlag, Berlin (1956).

5. N. de Jonge, M. Allioux, M. Doytcheva, M. Kaiser, K. B. K. Teo, R. G. Lacerda and W. I. Milne. Characterization of the field emission properties of individual thin carbon nanotubes. *Appl. Phys. Lett.* **85**, 1607-1609 (2004).

6. Y. Saito, K. Hata and T. Murata. Field Emission Patterns Originating from Pentagons at the Tip of a Carbon Nanotube. *Jpn. J. Appl. Phys.* **39**, L271-L272 (2000).

7. T. W. Odom, J.-L. Huang, P. Kim and C. M. Lieber. Structure and Electronic Properties of Carbon Nanotubes. *J. Phys. Chem. B* **104**, 2794-2809 (2000).

8. C. J. Edgcombe and N. de Jonge. Deduction of work function of carbon nanotube field emitter by use of curved-surface theory. *J. Phys. D: Appl. Phys.* **40**, 4123-4128 (2007).

9. E. W. Müller. Beobachtungen über die Feldemission und die Kathodenzerstäubung an thoriertem Wolfram. *Zeitschrift für Physik A*

Hadrons and Nuclei **106**, 132-140 (1937).

10. M. Drechsler. Erwin Müller and the early development of field emission microscopy. *Surface Science* **70**, 1-18 (1978).

11. Schwoebel, P. R., Spindt, C. A., Holland, C. E. & Panitz, J. A. Field emission current cleaning and annealing of microfabricated cold cathodes. Papers from the 13th international vacuum microelectronics conference 19(3), 980-987. 2001. Guanghou (China), AVS.
Ref Type: Conference Proceeding

12. K. A. Dean and B. R. Chalamala. Experimental studies of the cap structure of single-walled carbon nanotubes. *J. Vac. Sci. Technol. B* **21**, 868-871 (2003).

13. T. Kuzumaki, Y. Horiike, T. Kizuka, T. Kona, C. Oshima and Y. Mitsuda. The dynamic observation of the field emission site of electrons on a carbon nanotube tip. *Diamond Relat. Mater.* **13**, 1907-1913 (2004).

14. K. A. Dean and B. R. Chalamala. Field emission microscopy of carbon nanotube caps. *Journal of Applied Physics* **85**, 3832-3836 (1999).

15. E. W. Muller. Resolution of the Atomic Structure of a Metal Surface by the Field Ion Microscope. *Journal of Applied Physics* **27**, 474-476 (1956).

16. E. W. Müller. *Z. Physik* **31**, 136 (1951).

17. E. Munro, J. Rouse, H. Liu, L. Wang and X. Zhu. Simulation software for designing electron and ion beam equipment. *Microelectronic Engineering* **83**, 994-1002 (2006).

3

A compact multi-purpose nanomanipulator for use inside a scanning electron microscope

A compact, two-stage nanomanipulator was designed and built for use inside a scanning electron microscope (SEM). It consists of a fine stage employing piezo-stacks that provide a 15 micrometer range in 3 dimensions and a coarse stage based on stick-slip motors, commercially available from Attocube. Besides the fabrication of enhanced probes for scanning probe microscopy and the enhancement of electron field emitters, other novel manipulation processes were developed, such as locating, picking up and positioning small nanostructures with an accuracy of ~10 nm. In combination with in situ *I-V* experiments, welding and etching, this results in a multi-purpose nano-factory, enabling a range of new experiments.

This chapter is based on the following publication:
Erwin C. Heeres, Allard J. Katan, Maarten H. van Es, Anne France Beker, Marcel Hesselberth, Dian van der Zalm, and Tjerk H. Oosterkamp, A compact multipurpose nanomanipulator for use inside a scanning electron microscope, *Rev. Sci. Instrum.* **81**, 023704 (2009).

3.1 Introduction

Nanomanipulation inside an electron microscope can give control on a very fine scale while providing real time feedback on the object being manipulated.[1-3] A nanomanipulator extends the applicability of the electron microscope far beyond that of an imaging tool, much like other available SEM add-ons, like GIS, EDX or a variable temperature stage. Sample fabrication processes often include characterization and localization of features of interest using optical microscopy, AFM or SEM and a subsequent design of actuation, measurement or control structures, often by lithographic processes.[4,5] Drawback of AFM and STM manipulation is that the process cannot be imaged, only the result, as the object which is used to manipulate with, is also used to obtain the image. With a manipulator inside an SEM however, the feature of interest can be accurately positioned in situ, immediately after localization onto another predefined structure.

In this chapter we first discuss the constraints to our design set by our electron microscope, then we discuss the design considerations that improve the user friendliness of the manipulator, the properties of the manipulator and finally we give some examples of fabricated structures.

3.2 Design considerations

To image and manipulate even the smallest nano-objects, like as-grown single-walled carbon nanotubes (SWNTs) lying on a Si substrate, or protruding from the edge of such substrates, we employ a 30 kV SEM (FEI, Nova NanoSEM) , which is equipped with a field emission source and a magnetic immersion lens system and has a measured resolution of 1 nm. To reduce the deposition of amorphous carbon during SEM imaging, a plasma-cleaner is installed and used to regularly clean the SEM chamber. Because of this, it is also necessary to use exclusively UHV compatible materials inside. Such a high-resolution microscope also imposes a number of restrictions on the design of a nanomanipulator to be used inside. Because of its magnetic immersion lens, all materials used in the manipulator have to be non-magnetic. Due to the size of the chamber, a compact design with a height of less than 57 mm is needed, such that the manipulator fits in the limited space

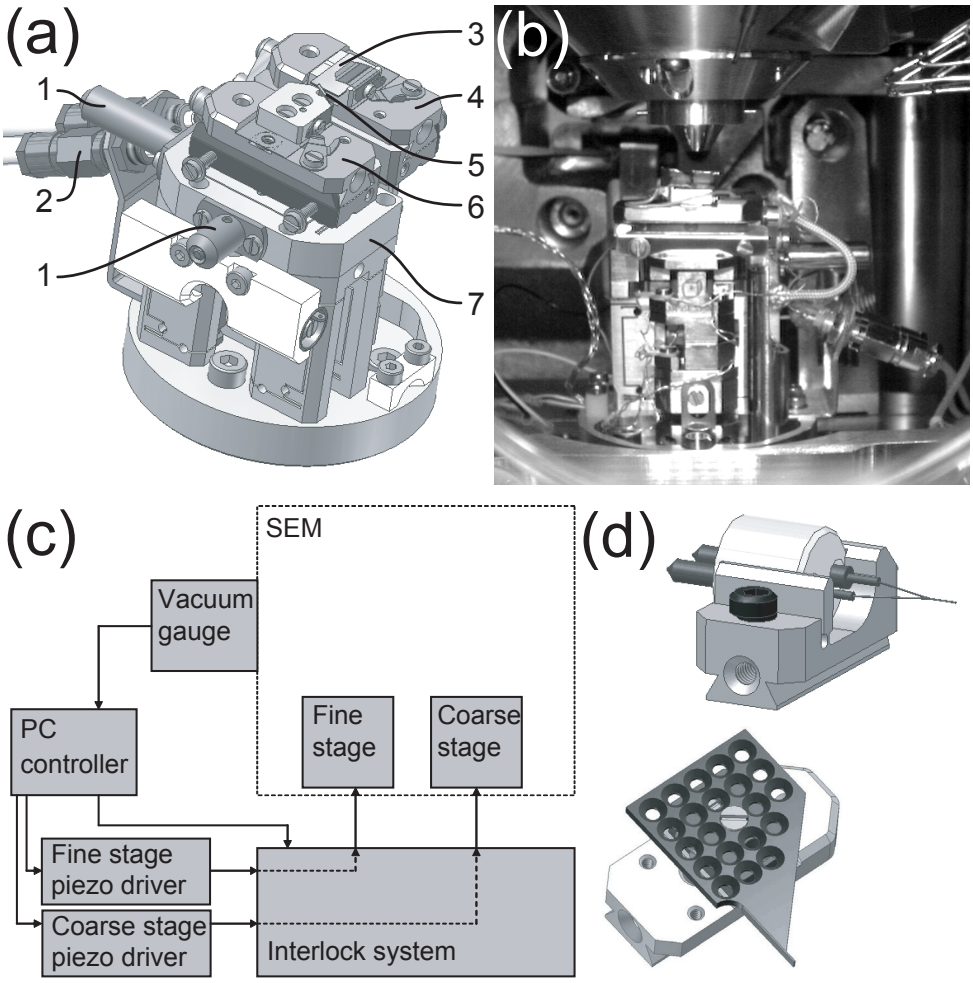


Figure 3.1 (a) 3D image of the nanomanipulator with the following numbered parts: (1) fine stage piezo-actuator, (2) IV-connector, (3) flat substrate holding objects to be manipulated (e.g. nanotubes, nanowires, diamond nanocrystals), (4) flat substrate slider on coarse stage, (5) AFM chip onto or by which objects are manipulated, (6) AFM chip slider on fine stage, (7) fine stage. (b) CCD image of the nanomanipulator installed in the SEM. The total available height underneath the polepiece is 62 mm. To be able to work at eucentric height, a working distance of 5 mm is required. The entire manipulator (total height: 52 mm) fits underneath the final lens and is screwed onto the default SEM stage. An additional adapter block facilitates installation and removal of wiring. (c) Schematic diagram of the nanomanipulator setup. (d) Two additional sliders. Above: field emission gun (FEG) source holder. Below: probing tip holder, e.g. to hold an etched tungsten tip.

underneath the final lens and experiments can be performed at the SEM eucentric working distance of 5 mm (see also Figure 3.1). With a total height of 52 mm for the entire manipulator we can thus work at a maximum working distance of 10 mm down to the smallest allowable working distance. The entire manipulator can be positioned within the chamber by moving the SEM stage.

To allow a wide variety of experiments, sliders were made that allow manipulation of different types of objects: sharp tips, e.g. etched metallic wires, AFM chips or field emission sources, but also flat samples, see Figure 3.1a and d. By using such sliders, the time needed to create a functionalized probe is reduced, because it allows the rapid exchange of the tip and/or the sample that contains the objects that are to be mounted. For this too, the SEM is more convenient than a TEM, where sample sizes are restricted to a few millimeters and waiting times are often longer. The sliding system has been designed in such a way that different holders – each designed for a specific tip – slide onto the manipulator base. A guiding rail and spring clamping assembly enable a stable but movable connection. Furthermore, the detached slider enables simple installation and positioning of a tip or substrate outside the confined environment of the SEM chamber.

The range of motion of the manipulator should be large enough to be able to preposition the samples manually without the need of an optical microscope. As nanomaterials are often grown onto substrates of several cm^2, a range of several millimeters is desirable such that cleaving of the sample is not necessarily needed and a large area can be searched to find a suitable nano-object to be mounted. The sizes of samples that can be accommodated onto our manipulator range up to 30 mm by 30 mm with a maximum height of 10 mm.

A drawback of a system with a very large range often is its poor positioning accuracy. To take advantage of a large range and a high positioning accuracy, a coarse positioning system used for the approach was combined with a separate fine positioning system. For the coarse stage, a system consisting of three stackable positioners was used (Attocube, ANP 50 series, ANC 150 step controller), all non-magnetic and UHV compatible. The fine stage, a flexure hinge design, is operated

using piezo stacks (PI, PICMA™, P-883.50, -20 V to +120 V) with a continuous range of motion. The piezo stacks are integrated into the flexure hinges in a way that limits shear stress on the piezo stacks, such that these stacks do not break if forces act laterally on them. Due to this design, coupling between the two mutually orthogonal directions of motion is avoided as x and y motions are integrated into the same body of material. Furthermore, this design enables easy installation of an actuator if replacement would be needed.

Separation of fine and coarse motion on two different stages allows accurate imaging of the tip and overcomes problems arising from unwanted motion during coarse positioning, such as hysteresis and vibrations of the stick-slip motor, which are discussed in detail in the next section. When changing the step direction of a coarse stage actuator, it needs several step actuations before it is running properly in the desired direction. In between, a combination of two unwanted effects is observed: motion in the opposite direction (which accumulates to a total of ~300 nm) and motion in the orthogonal directions (which accumulates to a total of ~700 nm). We attribute these effects to the reorientation of the rod-shaped piezo inside its housing after a step-direction change has been given, as the housing is clamped mechanically using springs onto the piezo over which it runs forwards and backwards. We find that it is not possible to use the coarse stage to perform accurate positioning processes. However, the magnitude of these effects is an order of magnitude smaller than the range of the fine stage and simple approach and retract operations can repeatedly be performed without any tip crashes, as the fine stage is designed to be robust and incorporating a large range.

3.3 Stage movement and stability

Figure 3.2 shows the (x,y)-motion of the coarse stage as its motors step in x, y and z. For each panel in the figure a motor is given ten single step actuations in one direction followed by ten steps back, after which this sequence is repeated one more time. Arrows indicate after which points the step direction is reversed. As can be seen from the figures, the coarse stage shows hysteresis; unwanted motion in the opposite direction as well as an unwanted motion perpendicular to

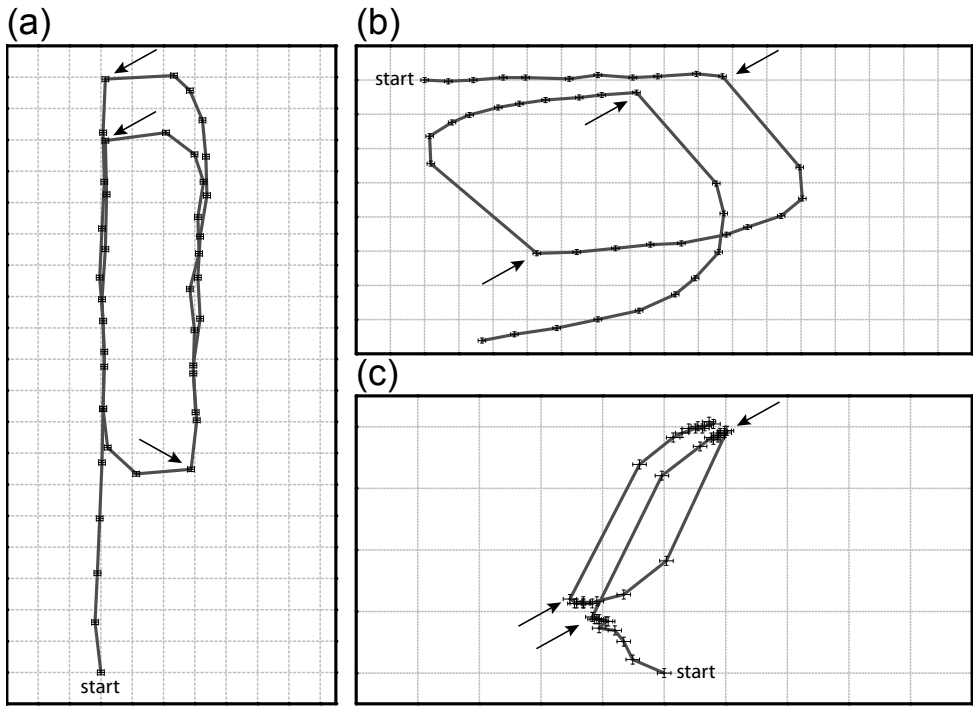


Figure 3.2 Measured movement of the coarse stage in the XY-plane after applying individual step actuations to each of the three actuators. Before the measurements, each actuator has been pre-conditioned by actuating steps (>10) in the starting direction, ensuring proper linear movement. From each starting point, 10 step actuations were given in the starting direction, after which the direction of the steps was reversed. The point after which this change is performed has been indicated with arrows. In the opposite step-direction, another 10 steps were actuated, after which the entire sequence is repeated again, without pre-conditioning. The data points were obtained by in situ SEM imaging and have been determined with an accuracy of about 10 nm. The grid lines have a separation distance of 100 nm. Actuation in the (a) y-direction, (b) x-direction and (c) z-direction.

the intended direction of motion. The total movement in the opposite direction accumulates to ~300 nm for the x-actuator and ~25 nm for the y-actuator during 10 steps. The motion in directions perpendicular to the intended motion of the x, y and z actuators, is measured to be roughly 700 nm, 300 nm, and 300 nm respectively. Due to imaging in the x-y plane, motion in the z-direction cannot be observed directly. However, as measured on the z-actuator, unwanted motion in both orthogonal directions are present, hence due to design similarities this is also

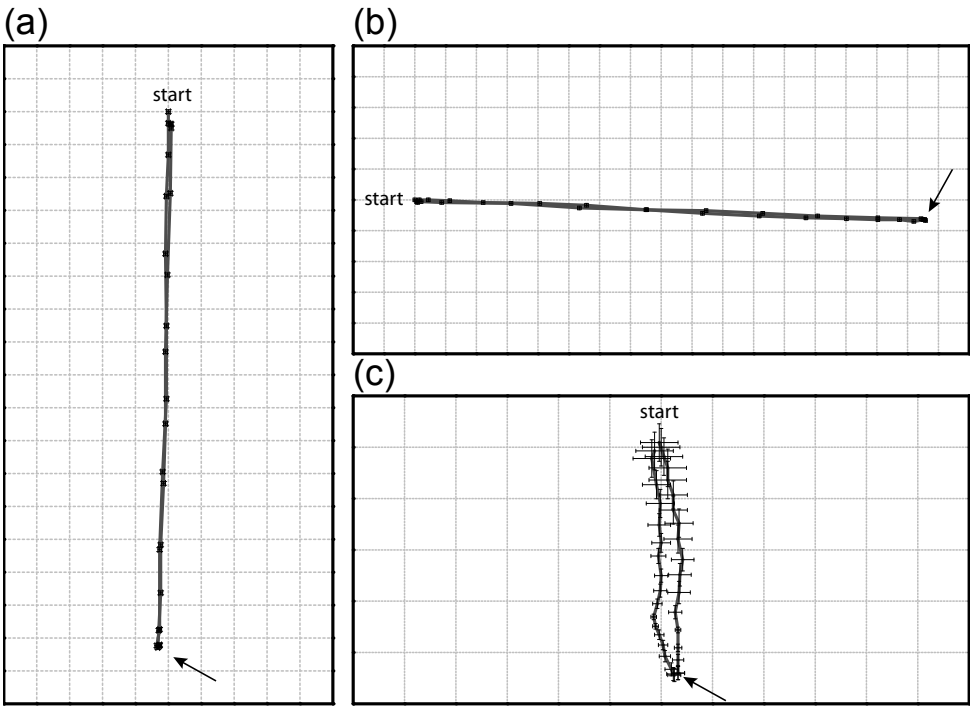


Figure 3.3 Measured movement of the fine stage in the XY-plane over its entire range. The data points were obtained by analyzing the position of a sharp tip on the fine stage from in situ recorded SEM movies. The stage was moved forward and backward once over its entire range of 15 μm; the change of direction is indicated with an arrow. From a linear fit, the angle between x and y directions was found to be (90.9 ± 0.1) °. Actuation in the (a) y-direction and (b) x-direction. The grid lines have a separation distance of 1 μm; data points have been determined with an accuracy of about 60 nm. (c) Actuation in z-direction with a grid line separation distance of 100 nm. This figure shows how much the fine stage moves in x and y when the actuator is moved in z by 15 μm and back. Due to the SEM's limited depth of focus, the error bars increase when the tip is moving out of focus.

expected to be the case for the x- and y-actuator. Although the x and y actuators are of similar types, a large difference in behavior is observed. The x actuator needs more than 10 steps for linear motion after a direction change, whereas the y actuator needs 4.

The measured movement of the fine stage over its entire range is presented in Figure 3.3. Data points were obtained by analyzing the frames from in situ recorded

SEM movies and measuring the position of a sharp tip that was mounted onto the stage. Because the fine stage motion is continuous, one out of every 200 frames was analyzed. The angle between x and y directions was obtained by a linear fit and equals (90.9 ± 0.1) °, which shows the two directions are orthogonal within one degree. The observed diagonal motion is caused by a slight difference between the electron beam scan line direction and the positioning of the stage inside the SEM. Figure 3.3c shows the motion in x-y direction during actuation of the z-direction. A shift of about 450 nm in y direction is observed, which can be compensated for by programming the piezo control software to move the y-stage in opposite direction.

In Figure 3.4 we show the vibrations of the fine and coarse stage while obtaining an image, with a dwell time of 24 μs per pixel and 24.6 ms per line. These are the residual vibrations after engaging the active vibration isolation that the SEM is equipped with. As can be concluded from the amount and magnitude of flags and spikes, see Figure 3.4b, the coarse stage suffers much more from instabilities. These vibrations are inherent to the design of the piezo-electric actuators.

In addition, vibrations are present during actuation of the coarse stage. In Figures 3.4c-e three subsequent images obtained from a movie are depicted, that show the coarse stage shaking with an amplitude of approximately 500 nm, while it is being operated in single-step mode. The fine stage moves with an amplitude roughly three times smaller. After a few frames the vibrations are damped out.

3.4 Nanomanipulator operation

The coarse stage has a range of motion of 4 mm in x and y and 2.5 mm in z. The step sizes of the coarse stage are controlled by varying the driver signal amplitude and are specified to range from 25 nm to 500 nm. The step size depends on the clamping force which is set by the manufacturer as well as on the mass that is being moved and the state of the sliding surfaces.[6] Hence the step size as a function of driving signal amplitude will vary for each actuator. When operating the coarse stage at a 10 V actuation amplitude, which represents a compromise between minimal step size and reasonable reliability, this yields an average step size of approximately

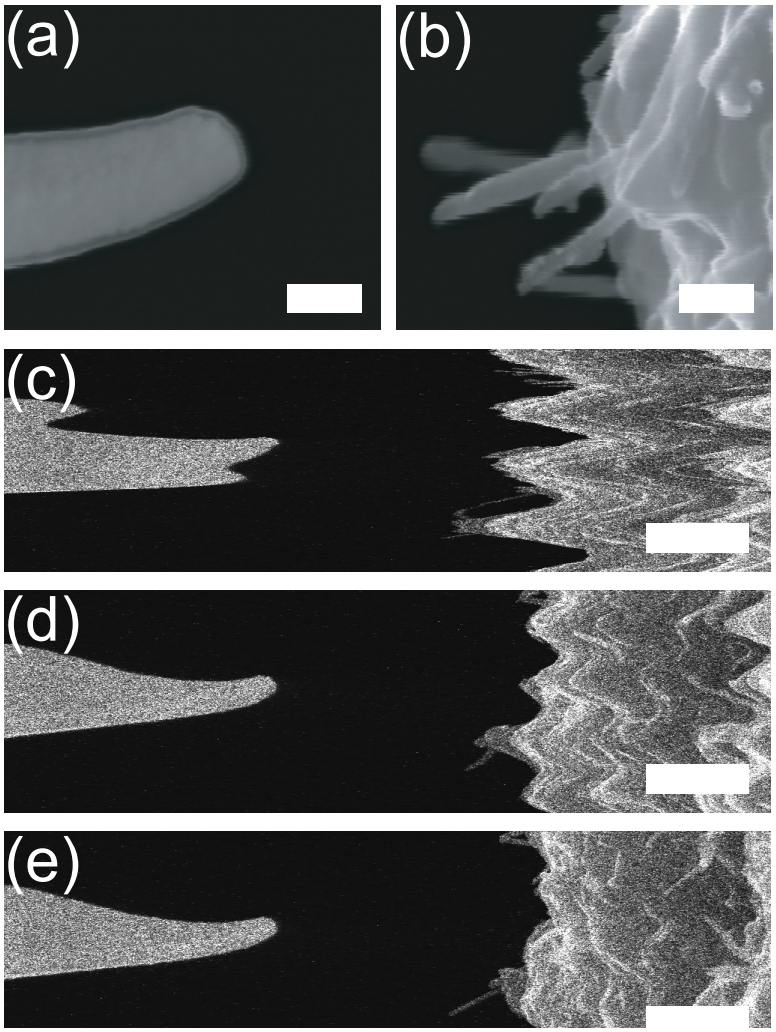


Figure 3.4 Stability of the nanomanipulator as observed by SEM imaging. (a)-(b) Stability durig image acquisition. Each image was obtained with a dwell time of 24 μs per pixel, and a linetime of 24.6 ms. Flags in each image are present due to vibrations of the stages. The length of the scalebar equals 100 nm. (a) Fine stage with a sharp AFM tip. Few spikes are observed with a maximum of ~ 10 nm. (b) Coarse stage with a sample of MWNTs protruding from a support sample. Many flags and spikes with a maximum up to ~ 50 nm are visible. (c)-(e) Actuation stability during single-step coarse stage movement. Images obtained from a movie which was recorded with a frame rate of 40 Hz. The scalebar has a length of 500 nm. (c) Immediately after step actuation. (d) After 25 ms. (e) After 50 ms. Due to conversion of the raw SEM images to an avi movie, the frame rate is automatically converted to 100 fps. In such a movie, multiple frames show the exact same SEM capture, so this is not the true frame rate which is 40 Hz. Judging from the avi movie, the second frame follows after 13 ms, whereas the third frame follows 30 ms after frame 1. However, with a SEM imaging rate of 40 Hz, this should be 25 ms and 50 ms respectively.

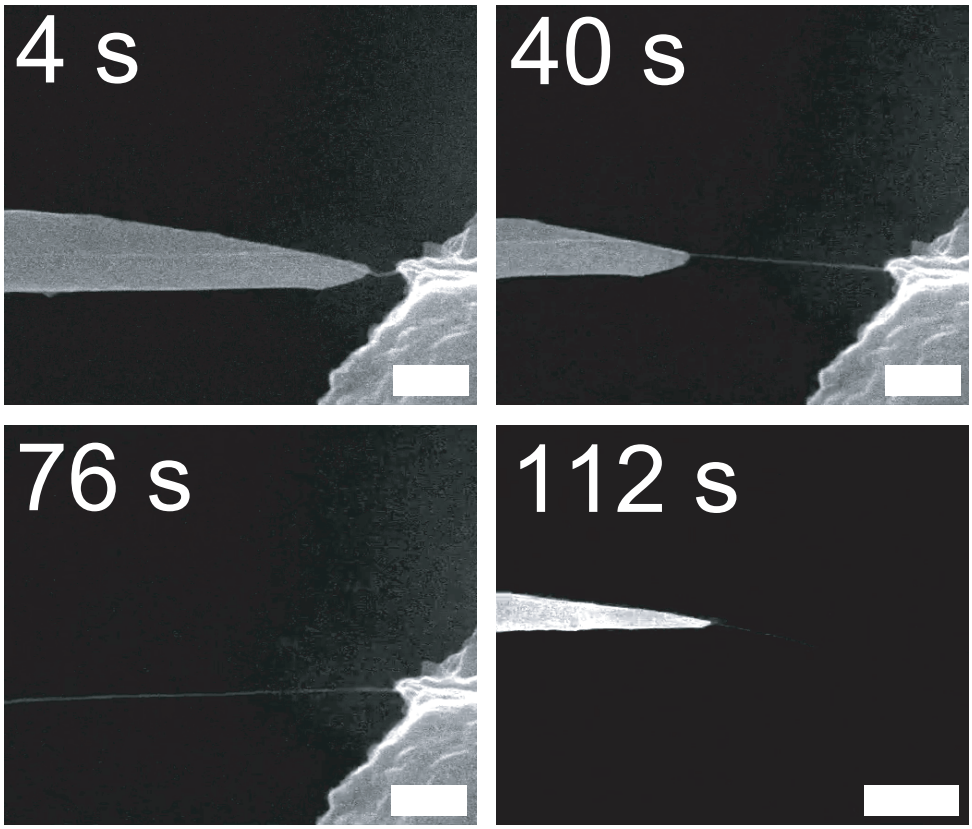


Figure 3.5 The process of pulling a MWNT from its as-grown material by using a sharply etched tungsten tip mounted onto the fine stage. After approaching and attaching the MWNT (not shown) the tip is carefully retracted; movement is performed only by operating the fine stage. The substrate with the MWNT material is mounted onto the coarse (approach) stage. Four still images show the process at 4 s, 40 s, 76 s, and 112 s (movie available online). (Scale bars: 300 nm, 300 nm, 300 nm, and 3 μm, respectively)

90 nm in x and 170 nm in y. Although the step sizes of the coarse stage actuators are not constant, as was discussed above, this does not interfere with any of the experiments we perform due to the fine stage design.

The fine stage shows continuous motion within a range of 15 μm in x, y and z. It is operated by home-built piezo-drivers which receive an input signal from a DAC card inside the PC. Motion in x and y are orthogonal within one degree, as

was shown before. The z-motion is not completely decoupled from the y-motion, probably due to the use of two piezo-actuators that are not completely balanced. Over the entire range of motion of the fine stage z-piezo (15 μm) the stage moves by 450 nm (3 %) in the perpendicular directions, which can be compensated for by the piezo control software. When changing the direction of movement, the fine stage does not show overshoot in the wrong direction. An example of the fine stage operation during the process of mounting a MWNT is presented in a movie which can be viewed online, see Figure 3.5.[7]

Using Labview, a user-interface was created that can be controlled using a three axes joystick system (Saitek, X52). The speed with which either the coarse or the fine stage moves, is determined by the joystick and can be adjusted to be more or less sensitive on the joystick motion. The joysticks are also used to switch between coarse and fine positioning and to apply single step actuations, voltage pulses, etc.

To perform *I-V* measurements and in situ field emission tests of mounted carbon nanotubes, the sample and tip stages were electrically isolated from the base of the manipulator and wired to high-voltage connectors and feedthroughs. All wires can be disconnected from the SEM stage after which the manipulator can be removed within a few minutes for normal SEM imaging. In Figure 3.1c a schematic diagram of the manipulator system is depicted. To prevent damaging the piezo actuators during venting or evacuating the SEM, an interlock system was designed. Hence the manipulator can be operated only at ambient pressure and pressures below 10^{-4} mbar.

3.5 Applications

As is shown by some examples below, our design will work for a large variety of applications. To fabricate novel electron field emitters, both single-walled and multi-walled carbon nanotubes (MWNTs) and semiconductor nanowires have been mounted.[8,9] Closed MWNTs were mounted by pulling them from a sample with agglomerates of carbon nanotubes, see Figure 3.5. We have managed to repeatedly mount single MWNTs with their as-grown cap by pulling the entire MWNT without

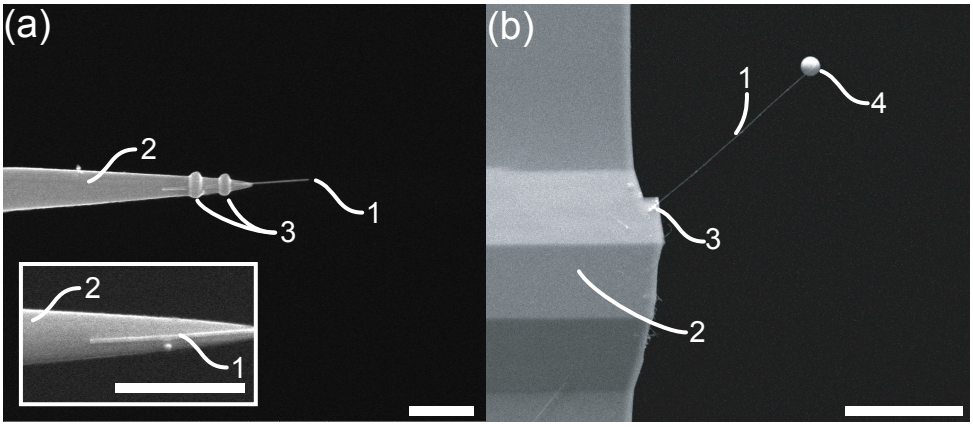


Figure 3.6 Two examples of probes fabricated with the nanomanipulator. (a) InAs nanowire (1) after mounting on a sharply etched tungsten tip (2). Using EBID a layer of Pt (3) was deposited maskless at two positions to ensure a proper fixation of the nanowire onto the tip. The inset shows the tungsten tip with the nanowire before deposition. (Scale bars: 1 μm) (b) SiC nanowire (1) mounted on an AFM chip (2). After fixing the nanowire by EBID (3), a small magnetic (NdFeB) particle (4) was added to the very end of the nanowire tip, also by EBID. In this way novel, very sensitive MRFM cantilevers can be constructed. (Scale bar: 30 μm)

breaking it from its as-grown material.[10] In these experiments a large fine stage range is needed to be able to handle flexible nanotubes or nanowires. With the fine stage it is possible to manipulate micrometer-sized as-grown nanotubes and -wires, without running out of range. Not only field emitters, but also high-aspect ratio AFM-tips with carbon nanotubes have been created, which enable the studies of rough surfaces in liquid.[11-13] In such mounting processes, nanotubes were cut using a voltage pulse, or by electron beam etching which was facilitated by introducing water vapor into the chamber.[14,15] Using a gas injection system (GIS) attached to our SEM, fixation of the nanotube or -wire was improved by electron beam induced deposition (EBID) of platinum at the position of overlap, see Figure 3.6a. Novel nanometer-sized electrochemistry electrodes consisting of an insulating AFM tip and mounted carbon nanotube were also created to study the electrochemistry properties of substances on a very small scale.[16] A combination of the techniques mentioned before, yields a very sensitive MRFM resonator, see Figure 3.6b.

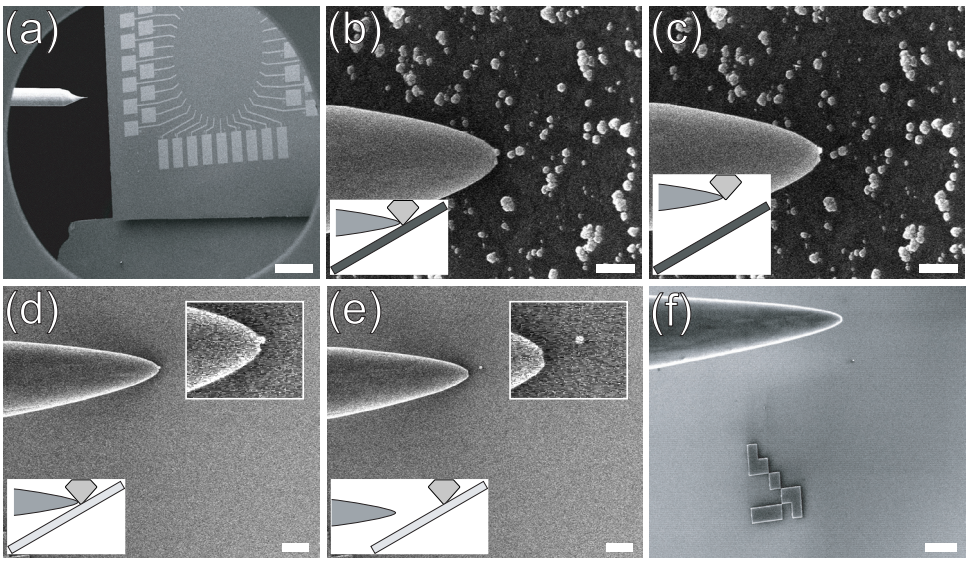


Figure 3.7 Positioning of a diamond nanocrystal. In this process a nanocrystal is picked up from a substrate onto which many were dispersed and positioned onto a different substrate containing markers located a few millimeters away. The insets in the lower left corners show a schematic representation of the position of the tip, substrate and diamond. (a) Demagnified view of both substrates and the etched tungsten tip. Substrates are tilted to facilitate picking up and positioning of nanocrystals. (Scale bar: 500 μm) (b)-(c) Picking up the nanocrystal from the substrate. (Scale bars: 500 nm) (d) and (e) Positioning near a marker on the other substrate. (Scale bars: 1 μm) (f) Demagnified view of (e), showing the positioned nanocrystal in the vicinity of a reference marker. (Scale bar: 2 μm)

Besides mounting, the nanomanipulator is used as a positioning tool. It has been used to pick up nano-objects and put them down somewhere else, as has been demonstrated for diamond nanocrystals placed accurately inside a photonic crystal.[17,18] The initial placement of a nanometer sized object can be performed with an accuracy of about 20 nm. After placement, the positioning accuracy can be enhanced by pushing the object with the tip. This final positioning is limited only by SEM imaging resolution of about one nanometer as the fine stage has a continuous range. The procedure to position these crystals is shown in Figure 3.7. The tungsten tip was etched in such a way as to yield a somewhat blunt, stiff and strong tip for the sole purpose to select and pick up the nanocrystals. Using a tip that was etched too sharply, resulted in deformation of the tip, as some nanocrystals

were stuck to the sample very tightly. To determine whether or not the tip touches the surface, a bias voltage was set between tip and sample and the current was measured using a picoammeter (Keithley). In order to reposition nanometer sized objects it is important to create a situation in which the adhesion of the object to the tip – with which it was picked up – is smaller than the adhesion to the surface onto which the object will be put down. This can be achieved by a combination of the following strategies. We try to keep the contact area between the object that is to be repositioned and the tip as small as possible. When the object is put down one can try to roll the object, in effect wiping it off the tip. It is also possible to put the object against another object and scrape it off the tip. Finally, we can use electron induced deposition to fixate the manipulated object to the surface onto which it is to be deposited.

Another strategy to facilitate manipulation is to apply a voltage difference across the sample and the tip. The detection of a current makes it easier to navigate the tip towards the surface. Additionally, the current through the manipulated object can be used to 'weld' it to the tip or the surface onto which it is to be repositioned. Subsequent *I-V* measurements can be used to characterize the quality of the electrical connections, which can be useful, e.g. for subsequent field emission, STM or electrochemistry experiments.

3.6 Conclusions and discussion

In conclusion, we have presented a stable and compact nanomanipulator consisting of a coarse stage with a range in x, y and z of several millimeters and a fine stage with a continuous range of 15 μm in all three dimensions. Its use has been demonstrated already in a wide range of experiments. Vibrations are limited to approximately 10 nm except during coarse stage actuation. Further improvements on a new coarse stage design are in progress.

References

1. N. de Jonge, Y. Lamy and M. Kaiser. Controlled Mounting of Individual Multiwalled Carbon Nanotubes on Support Tips. *Nano Lett.* **3**, 1621-1624 (2003).

2. D. Nakabayashi, P. C. Silva and D. Ugarte. Inexpensive two-tip nanomanipulator for a SEM. *Appl. Surf. Sci.* **254**, 405-411 (2007).

3. K. Andersen, K. Carlson, D. H. Petersen, K. Mølhave, V. Eichhorn, S. Fatikow and P. Bøggild. Electrothermal microgrippers for pick-and-place operations. *Microelectron. Eng.* **85**, 1128-1130 (2008).

4. M. S. Fuhrer, J. Nygård, L. Shih, M. Forero, Y. G. Yoon, M. S. C. Mazzoni, H. J. Choi, J. Ihm, S. G. Louie, A. Zettl and P. L. McEuen. Crossed Nanotube Junctions. *Science* **288**, 494-497 (2000).

5. T. Brintlinger, Y. F. Chen, T. Dürkop, E. Cobas, M. S. Fuhrer, J. D. Barry and J. Melngailis. Rapid imaging of nanotubes on insulating substrates. *Appl. Phys. Lett.* **81**, 2454-2456 (2002).

6. C. Meyer, O. Sqalli, H. Lorenz and K. Karrai. Slip-stick step-scanner for scanning probe microscopy. *Review of Scientific Instruments* **76**, 063706-5 (2005).

7. See the nanotube pulling video online, *http://www.frozenlines.com/physics/NanotubePulling.avi*

8. N. de Jonge, Y. Lamy, K. Schoots and T. H. Oosterkamp. High brightness electron beam from a multi-walled carbon nanotube. *Nature* **420**, 393-395 (2002).

9. E. C. Heeres, E. P. A. M. Bakkers, A. L. Roest, M. Kaiser, T. H.

Oosterkamp and N. de Jonge. Electron Emission from Individual Indium Arsenide Semiconductor Nanowires. *Nano Lett.* **7**, 536-540 (2007).

10. E. C. Heeres, T. H. Oosterkamp and N. de Jonge. The size of the localized electron emission site on a closed multi-walled carbon nanotube. *Submitted* (2011).

11. M. H. van Es. A new touch to atomic force microscopy: smart probing of biological and biomedical systems at the nanoscale. Ph.D. thesis, Leiden University (2008).

12. A. J. Katan and T. H. Oosterkamp. Measuring Hydrophobic Interactions with Three-Dimensional Nanometer Resolution. *J. Phys. Chem. C* **112**, 9769-9776 (2008).

13. H. Dai, J. H. Hafner, A. G. Rinzler, D. T. Colbert and R. E. Smalley. Nanotubes as nanoprobes in scanning probe microscopy. *Nature* **384**, 147-150 (1996).

14. T. D. Yuzvinsky, A. M. Fennimore, W. Mickelson, C. Esquivias and A. Zettl. Precision cutting of nanotubes with a low-energy electron beam. *Appl. Phys. Lett.* **86**, 053109-3 (2005).

15. E. C. Heeres, T. H. Oosterkamp and N. de Jonge. Making carbon nanotube electron sources of defined lengths and with closed caps. *Nanotechnology* **22**, 235308 (2011).

16. A. V. Patil, A. F. Beker, F. G. M. Wiertz, H. A. Heering, G. C. Coslovich, R. Vlijm and T. H. Oosterkamp. Fabrication and characterization of polymer insulated carbon nanotube modified electrochemical nanoprobes. *Nanoscale* **2**, 734-738 (2009).

17. T. van der Sar, E. C. Heeres, G. M. Dmochowski, G. de Lange, L.

Robledo, T. H. Oosterkamp and R. Hanson. Nanopositioning of a diamond nanocrystal containing a single nitrogen-vacancy defect center. *Appl. Phys. Lett.* **94**, 173104-3 (2009).

18. T. van der Sar, J. Hagemeier, W. Pfaff, E. C. Heeres, S. M. Thon, H. Kim, P. M. Petroff, T. H. Oosterkamp, D. Bouwmeester and R. Hanson. Deterministic nanoassembly of a coupled quantum emitter--photonic crystal cavity system. *Applied Physics Letters* **98**, 193103 (2011).

4

Mounting techniques

The object of mounting is obtaining a nanometer sized probe, containing a single nano-object, i.e. nanotube, nanowire or nanodiamond. In this chapter several mounting techniques will be described that were used in our experiments. The different ways in which such a nanoprobe can be obtained are compared. Furthermore, several after-mounting treatments are described, performed to optimize the probe for its application. To obtain a suitable sample to mount from, sample preparation techniques are started with.

4.1 Sample preparation

4.1.1 Carbon nanotube samples

Arc discharge CNTs come in powder form (soot), where several kinds of carbonaceous materials can be present: carbon onions, graphite flakes, fullerenes, multi-walled carbon nanotubes, single-walled carbon nanotubes and amorphous carbon.

To make use of the soot, a suspension is made, which can be used in different ways after sonication of the soot in a liquid medium within an ultrasonic bath. By using an ultrasonic bath, the larger carbonaceous aggregates will be broken down into smaller ones. One way of using the obtained solution is by drying: after drying, the aggregates are easily picked up using a substrate – in our case often a piece of metallic foil covered with conductive carbon tape, or even without the tape. A second method involves the application of a drop of the suspension onto the substrate and subsequent drying. A check with the electron microscope immediately shows the results of both methods, and the quality of the sample is judged by the availability of free standing CNTs with a length of at least several hundreds of nm, which can be approached with a sharply etched tungsten tip (tip radius of curvature typically ~ 100 nm). Several SEM images of a mounting sample with conductive carbon tape are shown in Figure 4.1. It should be noted that the optimal solvent to make a proper suspension can differ for different nanotube samples. For our ROS1 sample,[1-3] we made suspensions that would stay stable for several days using di-chloro-ethane.

Chemical vapour deposition (CVD) grown CNTs are grown on a substrate using catalyst particles. Hence the density is often lower than in the arc discharge soot and cleaving the sample can already result in single freestanding nanotubes protruding from the edge. The cleaved substrate is ready for mounting nanotubes.

Purification methods exist,[4,5] but often it is hard to successfully repeat such a method, or the method could damage the CNTs, i.e. oxidation methods easily damage the nanotube cap. All of our experiments on CNTs were performed with as-grown CNTs or with CNTs obtained from sonicated suspensions. Described

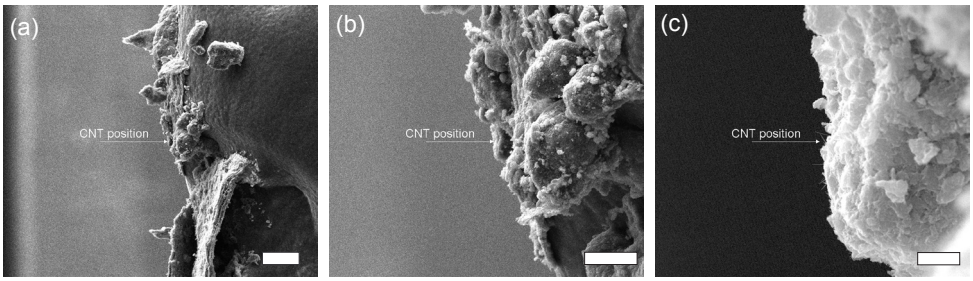


Figure 4.1 SEM images of a multi-walled carbon nanotube mounting sample. (a) Aggregates of carbonaceous particles picked up with a conductive carbon tape covering a metallic (tantalum) substrate. The position on the sample containing freestanding MWNTs is marked with an arrow. (Scale bar: 50 μm) (b) View of several aggregates. (Scale bar: 20 μm) (c) Zoom into aggregate containing freestanding MWNTs. (Scale bar: 2 μm)

elsewhere are our efforts to try and apply purification methods, like heat treatment, to obtain separated single tubes. However, most of these methods resulted in CNTs with affected caps.[5]

4.1.2 Nanowire samples

A nanowire mounting sample was made to be able to approach a selected nanowire with the support tip. It turned out that the nanowires, vapour-liquid-solid[6] (VLS) grown III-V semiconductor nanowires (InAs, InP, InAs/InGaAs heterostructured nanowires), were directed vertically,[7] i.e. perpendicular to the substrate, and the density of nanowires varied along the surface of the substrate, which made mounting directly from the silicon substrate difficult. Therefore, nanowires were transferred onto another silicon substrate that was cleaved with a diamond scribe to obtain a sharp edge on one side. Furthermore, this substrate had a conductive gold coating for imaging purposes. The transfer was performed under an optical microscope while using a micro-manipulator, pictured schematically in Figure 4.2a-c. The gold coated silicon substrate was positioned in close proximity to the growth substrate at a location on the growth substrate where the nanowire density was high. Successively, the gold coated substrate was carefully lowered until it just touched the wires, as in Figures 4.2a-b. The substrate was then translated parallel to the surface, to allow a large number of nanowires to adhere. Finally, the substrate

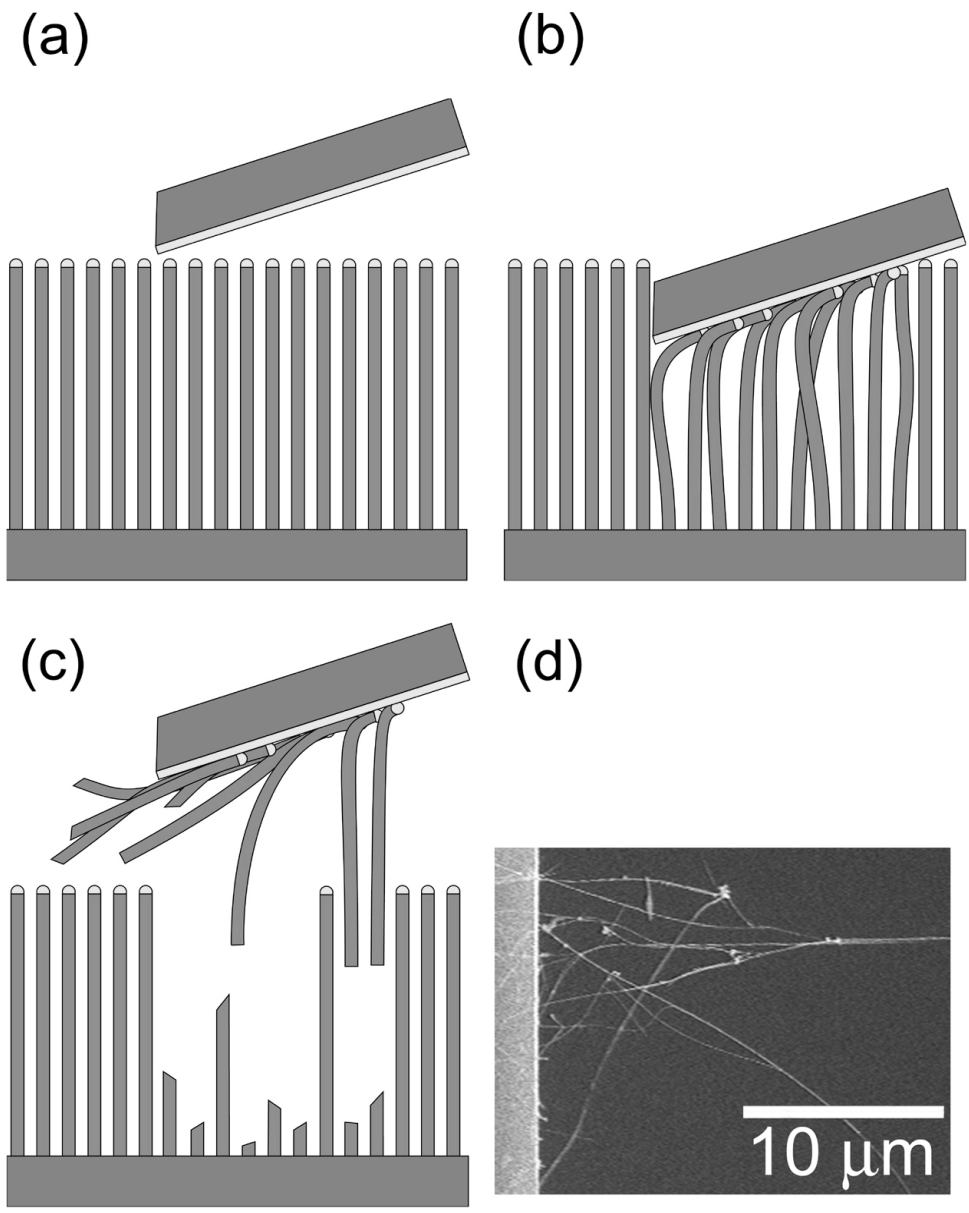


Figure 4.2 Schematic representation of the preparation of a nanowire mounting sample to use inside an SEM. (a) Approaching the as-grown nanowire sample (bottom) with a gold-coated substrate. The positioning is performed using a three-axis micro-manipulator under an optical microscope (not shown). (b) and (c) Touching and scraping the nanowires from the as-grown sample, in order to make them stick to the gold-coated mounting substrate. (d) SEM image of the edge of the gold-coated substrate with nanowires protruding from its edge.

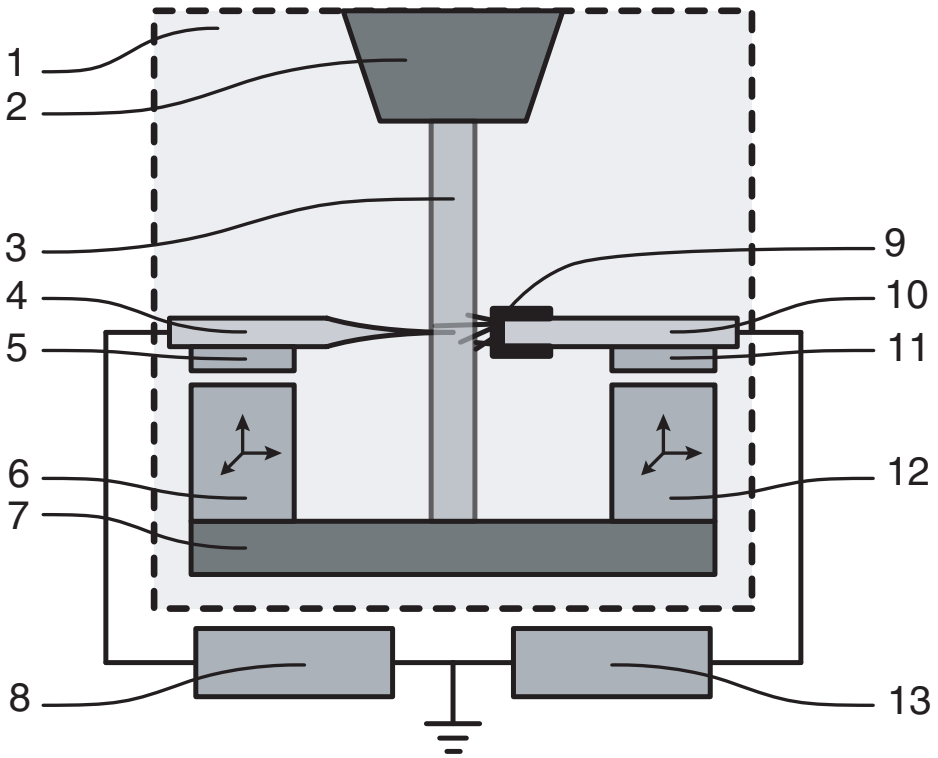


Figure 4.3 Schematic representation of the manipulator inside the SEM chamber together with the *IU* measurement setup. SEM chamber (1) with the column (2) generating the electron beam (3). The sharp tip (4) is mounted onto a removable slider (5) on the coarse stage (6). The manipulator base (7) is screwed to the SEM stage (not shown). A power supply (8) is used to apply a bias voltage between tip and sample. Carbon nanotubes (9) at the mounting sample (10) which is located on the removable fine stage slider (11). The fine stage (12) is also attached to the manipulator base (7). The current is measured using a picoammeter (13).

was retracted, causing the nanowires to detach from the growth substrate, as in Figure 4.2c. An SEM image of the resulting gold coated substrate with nanowires protruding from the edge is shown in Figure 4.2d. This substrate, the nanowire mounting substrate, was used to mount individual nanowires onto tungsten support tips for several applications: field emission sources and samples to test an atom probe system.

4.2 Mounting techniques

4.2.1 Attaching the carbon nanotube or nanowire to a tip

The general procedure to attach a nano-object, i.e. a nanotube or nanowire (in the following text I will just use "nanotube") to a sharp tip using a nanomanipulator will be described below. The nanomanipulator we used was custom-built and is described in detail in Chapter 3; the coarse stage was used to position the tip and the fine stage to position the nanotube sample. A schematic overview of the manipulator inside the SEM is given in Figure 4.3. To be able to view the position and attachment of the nanotube with respect to the tip, the nanotube has to be closer to the electron beam than the tip, as the tip is thicker and not transparent for the electron beam. After locating a nanotube to be mounted, both the very end of the tip and the nanotube are put at the same height using the coarse stage z positioner, which can be checked if both of them are in focus. To prevent unwanted motion of the coarse stage to interfere with the process, the height alignment is performed with the tip and nanotube sample separated laterally at least 10 microns. After height alignment, the coarse stage positioner is used to bring the sample and tip within fine stage range (typical separation ~ 5 microns), during which the fine stage has been retracted as far as possible. If both are within fine stage range, the fine stage z positioner is used to lower the tip several hundreds of nm, after which the fine stage can be used to approach the nanotube with the tip. The tip will be out of focus and imaged blurry compared to the nanotube which still is in focus, see Figure 4.4a.

The first step in attaching the nanotube to the tip is positioning the tip underneath the freestanding apex of the nanotube, where the position of the tip also determines the length over which the nanotube will be attached (overlap length), Figure 4.4b. Using the fine stage z controller, the tip height is increased until the nanotube apex touches the tip, shown in Figure 4.4c.

A method to determine whether the nanotube and tip are being manipulated at the same height is needed for proper alignment, Figure 4.4d. When the tip is moved up and down in the z-direction, the visible length of the nanotube will change, as it will

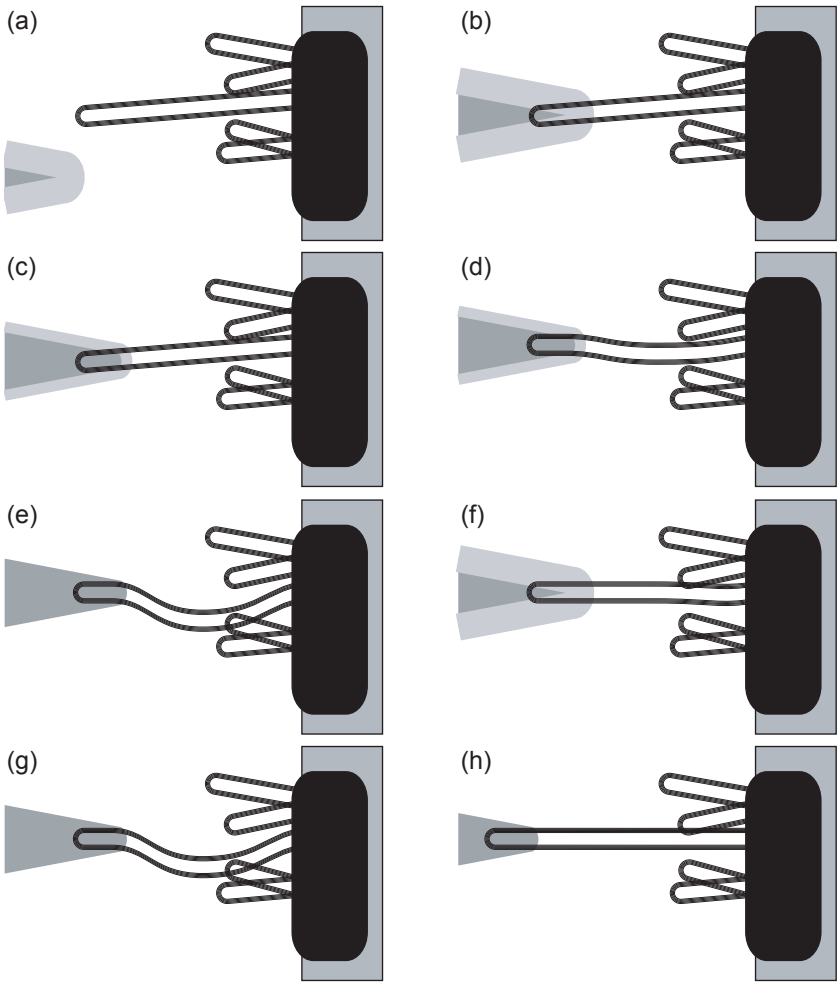


Figure 4.4 Schematic illustration of the process to attach a multi-walled nanotube to a sharply etched tip. The sample containing the MWNTs (right side) is pictured in focus. The tip (left side) is displayed with a border, where the thickness represents the amount of out-of-focus. Hence, the border thickness is a measure for the height difference between tip and sample. (a) Sample with MWNTs has been brought into plane of focus; the tip is lowered to be able to approach the freestanding MWNT without touching it. (b) Positioning of tip underneath the MWNT to be attached. The attachment length is determined by position of MWNT cap with respect to tip. (c) Decreasing height difference by moving tip upwards in z-direction until it touches MWNT. (d) Moving tip parallel to the edge of the mounting sample, so the MWNT can be straightened. (e) Further decreasing the height difference until tip and MWNT are in focus. The MWNT bends, because more of its length is visible in the x-y plane. (f) Stretching the MWNT such that it gets attached over the entire overlap length. This is done by moving the tip upwards, i.e. increasing height difference. (g) Tip lowered in focus, MWNT attached from its own apex up to the apex of the tip. (h) Retracting the tip to stretch the MWNT – MWNT is ready now to be detached from the mounting sample.

be stretched or bent. When the visible length becomes larger it effectively is being bent and more length of the nanotube becomes visible in the x-y imaging plane, hence the tip is moving towards the height at which the base of the nanotube is fixed at the sample, as shown in Figure 4.4e. When the nanotube's length decreases, i.e. it is being stretched and less length is visible in the x-y plane, as shown in Figure 4.4f, the tip is moving in a direction away from the nanotube's fixture.

Using the fine stage x, y, and z positioners, the tip is moved such that the nanotube is attached up to the apex of the tip, Figure 4.4g. The latter can be checked by movement of the nanotube with respect to the tip apex when moving the tip.

To check conductivity and/or touching of the tip and nanotube, a bias voltage can be applied between the tip and the sample. The current through the nanotube is measured using a picoammeter (Keithley). When focusing the electron beam on the overlap of the nanotube and tip, an increase in current is observed. This increase is higher than the beam current, indicating an improvement in conduction, i.e. a lower contact resistance, and the tip and nanotube are "welded" together.

At this moment, as pictured in Figure 4.4h, the nanotube is attached securely to the tip and several options exist to obtain the nanotube from the mounting sample, which will be discussed in the next section.

4.2.2 Obtaining the mounted nanotube tip

After attaching the carbon nanotube or nanowire to the tip, as described above, it can be detached from the mounting sample in several ways. Depending on the technique that is used, the original cap of the nanotube is obtained or a new apex is formed. Length control depends on which technique is selected. Three different techniques were used to obtain tips with mounted carbon nanotubes. First, the pulling method which leaves the nanotube as it was grown is discussed, as pictured schematically in Figure 4.5a. The second method involves cutting the nanotube at a desired location with the SEM electron beam, see Figure 4.5b. The third method uses a bias current through the nanotube to cut it, in a slow or a fast manner, respectively, Figure 4.5c.

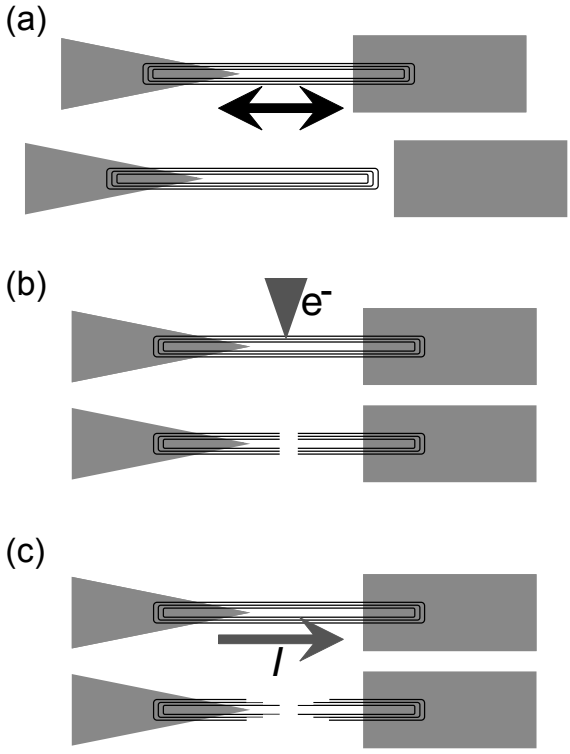


Figure 4.5 Three different techniques to separate the mounted CNT from the sample are pictured schematically. Sharp tip (left) and the mounting sample containing a MWNT (right). (a) Non-destructive separation by pulling the entire MWNT from the mounting sample. (b) Electron beam induced breaking. (c) Bias current cutting.

Each application for such a tip has its own requirements. For scanning probe experiments a stable but sharp tip is required to be able to scan rough surfaces – here a carbon nanotube tip provides better results than a regular SPM tip. To be able to scan in liquids, the fixation of the nanotube to the tip can be enhanced by electron beam induced deposition (EBID) of a material such as platinum.[8] However, for field emission a carbon nanotube with a closed cap is needed for stable emission, and preferably no materials added that could diffuse along the tip because of the high electric field strength and temperature at which it is operated.

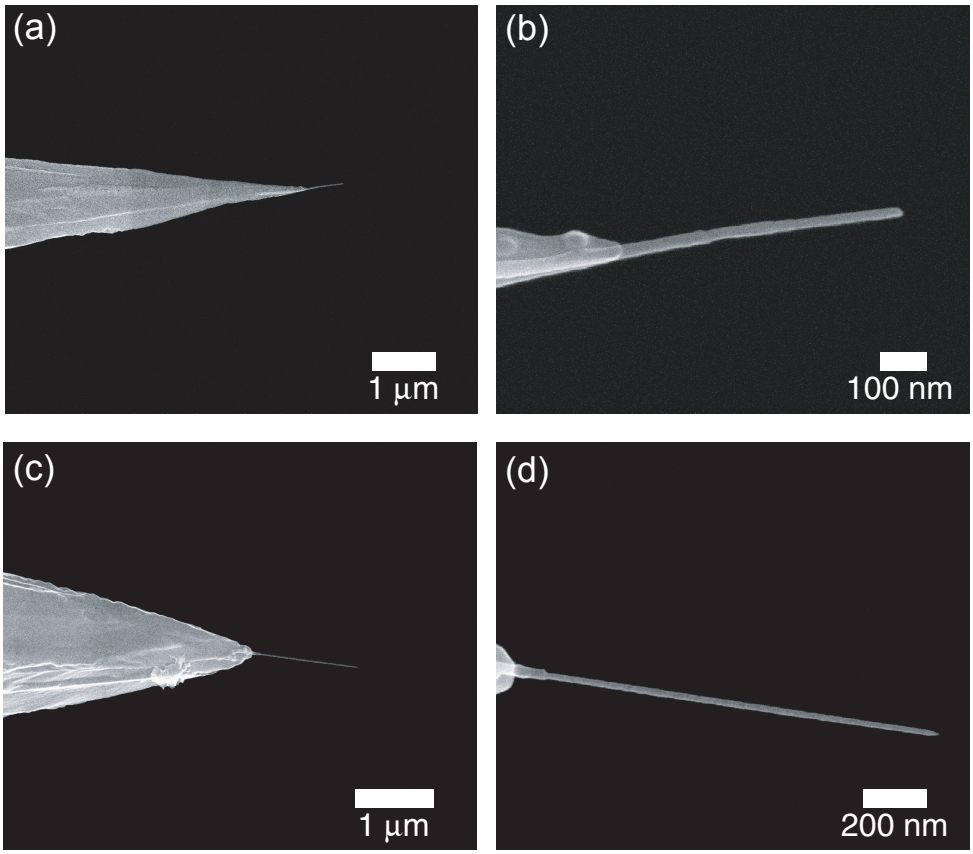


Figure 4.6 (a) (c) Two multi-walled carbon nanotubes mounted by pulling them out of the carbonaceous soot using the Leiden nanomanipulator. (b) (d) Enlarged views of the nanotubes.

4.2.3 Pulling without breaking

A non-destructive method was developed, in which the tip with the attached nanotube is retracted in such a way that the entire nanotube is pulled from the mounting sample, see Figure 4.5a. By using this technique the nanotube with its originally as-grown cap is obtained. See Figure 4.6 for SEM images of nanotubes mounted in this way. Field emission experiments on these carbon nanotubes show emission from spatially separated emission sites, indicating a pristine closed cap at the end of the nanotube. These experiments are described in further detail in Chapter 6.

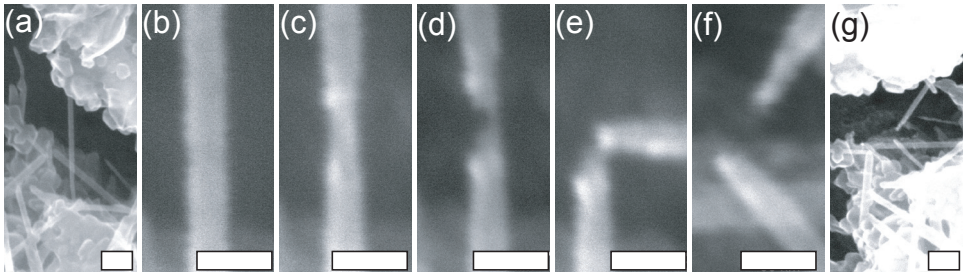


Figure 4.7 Cutting a MWNT using the electron beam in linescan mode. After a total time of about 11 minutes, the MWNT was completely cut without the use of any additional gases. (a) Overview of the MWNT, protruding from the carbonaceous aggregate at the bottom of the image. (Scale bar: 100 nm) (b) t = 0 s (Scale bar: 30 nm) (c) t = 30 s (Scale bar: 30 nm) (d) t = 195 s (Scale bar: 30 nm) (e) At t = 210 s, the upper part of the MWNT rotated about 90 degrees with respect to the bottom part. (Scale bar: 30 nm) (f) Image showing the completed cut obtained at t = 645 s and using a scan rotation of -45° to avoid scanning parallel to the length of either of the two pieces shown in (e). (Scale bar: 30 nm) (g) Overview of the cut MWNT. (Scale bar: 100 nm)

Often it is not possible to predetermine the length of the mounted nanotube, because as-grown arc-discharge nanotubes come packed into larger carbonaceous aggregates, see Figure 4.1c, and part of their length is hidden inside the aggregate. Only after pulling the entire nanotube out of its surrounding material, its length can be measured. We find that the length cannot be controlled using this method, since the length of the CNT buried in the soot varies.

This method will work for nanowires, too, as was shown by the direct mounting of a heterostructured nanowire from its as-grown substrate. The nanowire was attached in such a way that the part of the nanowire containing the gold catalyst particle protruded from the tip (results not shown).

4.2.4 Electron beam induced cutting

Another method was developed to be able to control the length of nanowires and nanotubes on tips using electron beam irradiation. By focusing the electron beam of the SEM on the part of the wire or tube between tip and sample, it can be broken either mechanically after irradiation or cut entirely by the electron beam. The

accuracy of this process is about ~ 10 nm, as was measured in the SEM. However, if the nanowire or –tube has not been attached properly to the tip, errors in length measurements might occur which can not be observed directly. The cutting of nanowires is discussed in more detail in Chapter 7, as this technique was used to obtain nanowire field emitters. Cutting MWNTs proved to be more difficult, so before cutting mounted MWNTs, experiments were performed to obtain proper beam settings and to prevent carbon deposition. One of the first successful cuts was obtained on a MWNT protruding from a carbon aggregate that was supported by an aluminum SEM stub, see Figure 4.7a. The acceleration voltage was set to 15 kV and a beam current of 700 pA was chosen. Figures 4.7b-f show the cutting progress after 0 s, 30 s, 195 s, 210 s and 645 s, respectively. An overview of the resulting cut, after approximately 11 minutes of irradiation, is shown in Figure 4.7g.

Cutting a mounted nanotube, i.e. a nanotube with one end attached to a tip as decribed before and the other end still attached to the mounting sample, proved to be more difficult. Therefore, different beam settings were used and the microscope chamber was cleaned beforehand using a plasma cleaner (XEI Scientific, Evactron) attached to the SEM.

For a low contact resistance between tip and nanotube, the oxide layer was removed from the tungsten tip before attaching the nanotube. This was performed by ramping a current through the tip, while touching a metal part of the sample on the fine stage, for instance the tantalum support foil. When applying a bias voltage, the oxide layer in between the tungsten and the foil would block a current from flowing. At a voltage of typically 0.5 V, the charge build-up would induce an electrostatic discharge, due to which the oxide layer was removed. Care should be taken to properly position the tungsten tip against the metal foil, otherwise a too high current will deform the tip, resulting in a not so useful spherical shape.

Successful cuts were obtained using an acceleration voltage of 15 kV and a beam current of 5.6 nA. To ensure proper alignment, the electron source tilt and shift were checked before using these settings.

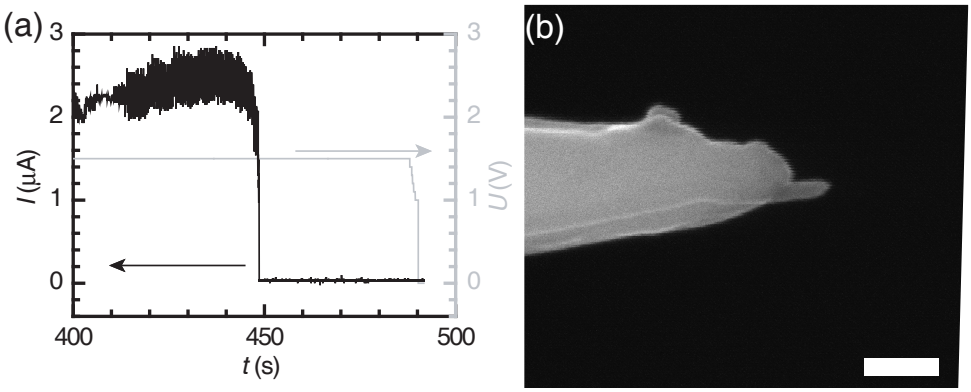


Figure 4.8 Monitoring the electron beam cutting process of a MWNT by using a bias current. (a) Bias voltage (U) and current (I) through the nanotube as a function of time. The monitoring process was started at t = 0 s, whereas the electron beam cutting was started at $t \approx 415$ s. After starting the electron beam irradiation of the MWNT in a reduced area scan mode, first an increase in the bias current was observed. After 20 seconds of irradiation ($t \approx 435$ s) the bias current through the MWNT started to decrease, and after 35 seconds ($t \approx 450$ s) it dropped to zero. (b) An SEM image of the resulting MWNT. (Scale bar: 100 nm)

After locating a freestanding nanotube, it was attached to the tip using the procedure described previously. The resistance of the tip and nanotube was measured to make sure a good contact will be obtained; typically a resistance of several hundred kilohm. The next step is zooming in into the section of the nanotube to be cut. The field of view is chosen such that the position of the cut can be determined accurately and the cut can be performed quickly. We used a magnification of 500k up to 1M times, before switching to the reduced area scan used for cutting, the typical size of the reduced area scan equals 50 nm × 10 nm.

In order to stop the irradiation process immediately after a complete cut has been obtained, the process should be monitored continuously. However, when irradiating the MWNT, it is not possible to properly judge the cutting progress from the line scan amplitude, nor from the reduced area scan signal. The MWNT might move during or after cutting, which affects the detected electron signal. Obtaining full frame SEM images during the process would take too much time as well. Hence

Table 4.1 Results of cutting three multi-walled carbon nanotubes using electron beam induced cutting. The electron beam was positioned at a certain distance from the tip apex (set length) and after the cut the length was measured using the SEM images (obtained length).

Sample	Set length (nm)	Obtained length (nm)
20070201MWNT01	150	170
20070201MWNT02	150	146
20070201MWNT03	150	161

the cutting progress was monitored by measuring the current through the MWNT resulting from a bias voltage applied between the tip and sample, see the schematic representation of the measurement/mounting setup in Figure 4.3. A successful cut results in a drop of the bias current, after which the electron beam can be blanked immediately. A graph of the bias current during electron beam cutting is shown in Figure 4.8.

To determine the accuracy with which a nanotube can be cut, three nanotubes were cut at a position 150 nm away from the tip apex. The length after a cut was obtained, was also measured and is shown in Table 4.1. An average length of 159 ± 7 nm was measured, which indicates the length of the nanotube can be controlled with an accuracy of at least 20 nm, as can be measured within the SEM. If the nanotube is positioned under an angle in the XZ plane its length might be different, which can be checked beforehand by tilting the entire sample stage. However, this was not done in our experiments.

Using a needle valve at the exterior of the chamber, water vapor could be added to the chamber, to speed up the cutting process from several minutes to less than one minute. The pressure was increased from $\sim 1 \times 10^{-6}$ mbar up to 5×10^{-5} mbar. The cutting of a nanotube, i.e. mass loss due to electron beam irradiation, with added water vapor is considered to be caused by oxidation.[9]

In conclusion, we have developed a method to obtain thick multi-walled nanotube probes, in which their length can be controlled within 20 nm. To study the effect of the electron beam on the crystallinity of the nanotube, TEM experiments were performed on cut nanotubes, which are discussed in more detail in Chapter 5. Moreover, experiments to change the apex and obtain stable field emission from such structures were performed and described in that chapter, too.

4.2.5 Wall-by-wall cutting using bias current

Instead of cutting the carbon nanotube with the electron beam, we have also used a bias current cutting method, as shown on MWNT samples #1 and #2 in Figures 4.9.[10] First, a carbon nanotube was attached to the tip of a platinum coated AFM chip. After this the tip with the nanotube was moved towards another platinum surface located at the fine stage, so a current could be sent through the carbon nanotube when the freestanding part was touching the surface. The platinum contacts ensured a low contact resistance, to have as much as possible energy dissipation into the carbon nanotube. By slowly increasing the voltage difference between tip and sample the current through the nanotube will increase, see MWNT #1 in Figure 4.9a. At a typical current of 200 μA and a voltage of 2.5 V, increasing the voltage more would not increase the current anymore, hence a maximum conduction was reached, see Figures 4.9b and c. This regime is called the saturation regime. By monitoring the current and regulating the voltage it is possible to cut the nanotube in a step-by-step manner up until a final drop to zero in the current and obtain a cut nanotube, Figure 4.9d. The decreasing steps in conductance have been attributed to the wall-by-wall destruction of the multi-walled carbon nanotube, where the nanotube is cut from outside inwards and its apex becomes conically shaped.[11] Hence, a sharpened, conically shaped tip is obtained in this way.

Using this procedure we cannot yet control the length of the obtained nanotube probe, as it will be cut at a position somewhere in between the two contacts. This position might be in the middle of the suspended carbon nanotube,[12] or at a “defect”, in the case of MWNT #2 defined by the particle visible in Figure 4.9e.

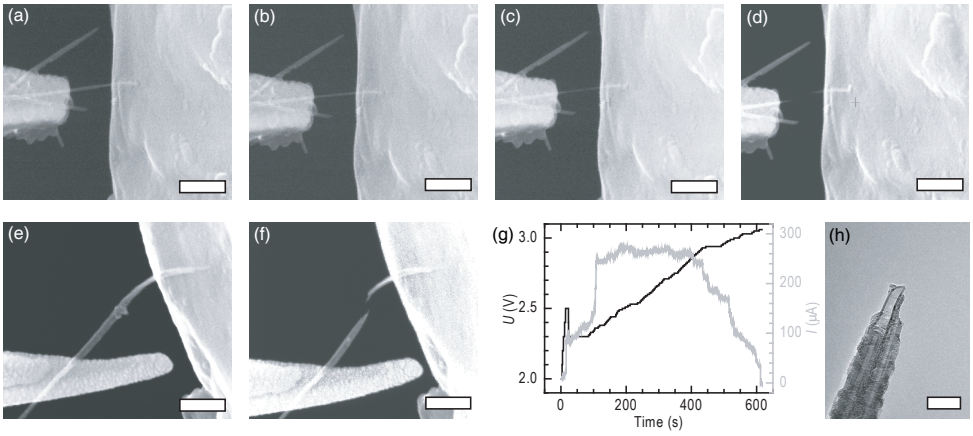


Figure 4.9 Cutting two multi-walled carbon nanotubes by ramping a bias current; MWNTs in between a platinum substrate and platinum coated AFM chip. (a)-(c) MWNT #1 becoming thinner. (Scale bar: 200 nm) (d) MWNT #1 cut and sharpened. (Scale bar: 200 nm) (e) MWNT #2 before cutting. (Scale bar: 200 nm) (f) MWNT cut and sharpened by the bias current, exactly at the position of the particle visible in (e). (Scale bar: 200 nm) (g) Applied voltage and measured current as a function of time. After the current saturates at ~250 μA, it started to decrease in a stepwise way. (h) TEM image of the cut MWNT, showing nicely graphitized walls and a closed cap. (Scale bar: 20 nm) Images and data courtesy of Dirk van Baarle.[10]

A significant sharpening of the MWNT #2 is visible in the SEM image of Figure 4.9f. The applied voltage and measured current as a function of time are presented in Figure 4.9g, clearly visible are the steps in the current. To investigate in more detail the cutting results, high resolution TEM images of MWNT #2 were obtained, shown in Figure 4.9h. The TEM image does not clearly reveal the nanotube has been cut wall by wall, as it shows several inter-tube boundaries and the whole structure seems to consist of two parallel running multi-walled nanotubes. The TEM data of the cut nanotube cannot be used to determine the exact cause of the conductance steps. However, it does show the nanotube has a closed cap and a well graphitized structure.

Summarizing the results, the conical shape ensures a very stable probe, with a thick base and a sharp apex, which was also observed on other nanotube samples, described in more detail in the bachelor thesis by Dirk van Baarle.[10] We envision

that this technique can be used to fabricate stiff, high aspect ratio carbon nanotube AFM probes with a small apex radius of curvature – an ideal probe to study rough surfaces. More experiments are needed to check whether the closed cap is a result of the cutting process, or that it is an artifact of the nanotube itself. Also more experiments are needed to investigate the position of the cut and the ability to control that position, for instance by the creation of a small defect using the electron beam.

4.3 Enhancing the mechanical contact of mounted probes

By depositing a thin layer of material onto the overlapping part of a nanotube or nanowire and its support tip, its adhesion will be improved significantly over the van der Waals adhesion forces. In this way probes can be obtained that have an improved mechanical contact. One example is the creation of carbon nanotube probes to perform AFM measurements in liquid, where the AFM tip with the nanotube can be dipped repeatedly into the liquid without loosing the nanotube.[8]

A layer of platinum can be deposited by electron beam induced deposition (EBID), after mounting a nanotube or nanowire and detaching it from the mounting sample, following the procedures described in the beginning of this chapter. An organometallic precursor ($MeCpPtMe_3$) was injected locally into the SEM chamber via a hollow needle, after which it sticks to the sample and is decomposed by the electron beam mainly by the secondary electrons at the location being scanned.[13,14] In this way nanowires and nanotubes, already attached to tips, were partially covered with a platinum containing layer, see Figures 4.10 and 4.11. Analysis of deposits using the same precursor by Botman et al. showed they contained an average amount of 81 at.% carbon.[15]

Another EBID method is the cracking of hydrocarbons still present in the SEM chamber, i.e. the residual gas, by which a layer of amorphous carbon can be deposited. However, the cleanliness of the chamber and sample affect the deposition rate, which are factors that are hard to control.

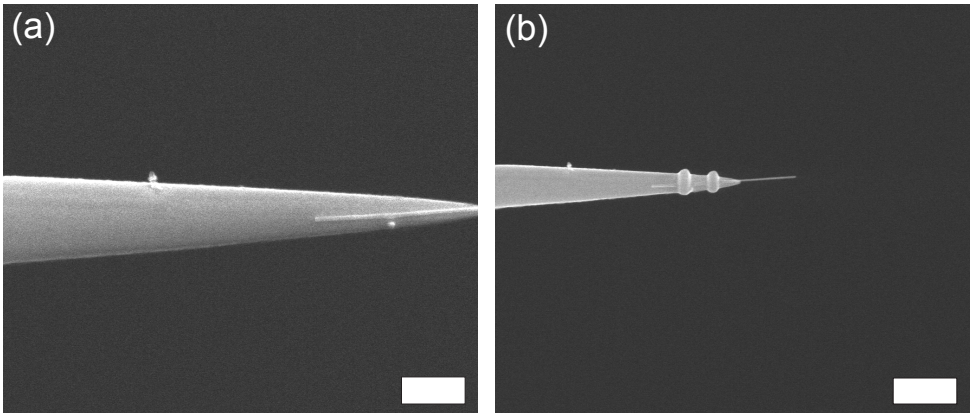


Figure 4.10 SEM images of the fixation of a nanowire by electron beam induced deposition of platinum inside the SEM. (a) Nanowire on tungsten support tip after mounting and detaching it from the mounting sample. To prevent unwanted deposition of carbon (from the residual gas inside the SEM chamber), the apex of the nanowire was not imaged at high magnification. (Scale bar: 500 nm) (b) Nanowire fixed with two Pt deposits, defined by rectangular scan areas. (Scale bar: 1 μm)

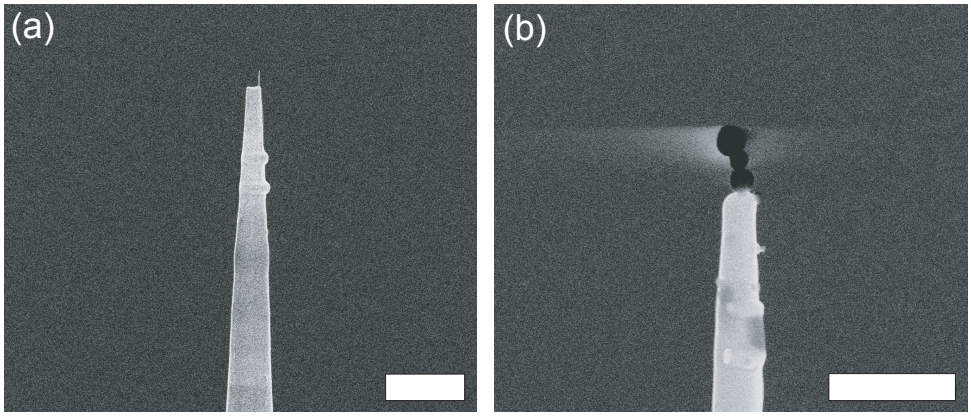


Figure 4.11 SEM images of a CNT field emission source fixed after mounting using platinum deposition. (a) CNT protruding from the W-tip and fixed by two line deposits of platinum, approximately 1 μm away from the end of the W-tip. (Scale bar: 1 μm) (b) After running field emission experiments at FEI Beamtech Hillsboro, the tip was again imaged in the SEM. The CNT is not visible anymore due to several spherical features present at the apex of the W-tip. (Scale bar: 1 μm)

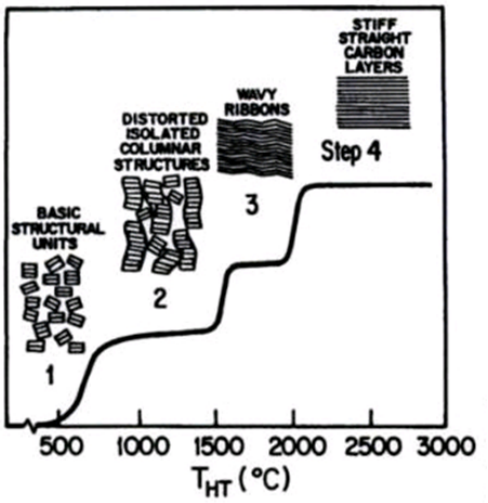
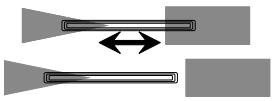
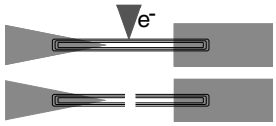
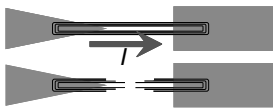


Figure 4.12 The different states in the graphitization process of a carbon nanotube as a function of temperature. Image obtained from "Physical properties of carbon nanotubes, R. Saito, G. Dresselhaus, M.S. Dresselhaus, Imperial College Press, 1998".[19]

SEM images of a Pt-fixed CNT are shown in Figure 4.11. After fixation the source was tested for field emission at FEI Beamtech in Hillsboro. Since the emitting area needs to be clean from adsorbates, it should be possible to heat the mounted nanotube up to ~ 600 ºC, as was shown by de Jonge.[16] If the deposited layer starts diffusing along the tip shank, it will influence the emission properties of the carbon nanotubes and its stability. After the field emission experiments, SEM images showed that the tip had been modified, probably due to diffusion of the deposited platinum during these experiments, see Figure 4.11b. At the position of the CNT spherical objects were found; the CNT was not visible anymore. Because of these results and because of another observation of diffusion of the platinum deposit along the tip by M. Ovsyanko, it was decided not to use platinum fixation for field emission sources anymore. From now on the fixation of the CNTs is being done by carbon deposition. Another alternative would be the use of a tungsten containing precursor, like WF_6.

Table 4.2 CNT mounting methods and properties.

Method	Length control	Cap type
 Non destructive mounting	No	Closed and graphitized, see Chapter 6
 E-beam induced cutting	Yes	Open, but can be closed after field emission and heat treatment, see Chapter 5
 Bias current cutting	Maybe	Closed and graphitized?

4.4 Conclusions and discussion

An overview of the different temperature states in the graphitization process of carbon nanotubes is given in Figure 4.12 and a list of the developed carbon nanotube mounting and modification methods is given in Table 4.2. From this it is seen that a temperature larger than 1500 °C is needed to graphitize a CNT again after cutting it. Such a temperature could be obtained by field emission current induced heating of the CNT apex,[17] and is subject of our research presented in Chapter 5.

The advantages of probes that are short are the high thermal stability. Because of this it is possible to obtain high resolution TEM images, as the thermal vibration amplitude of a short aspect ratio nanotube or nanowire is low enough to image separate walls and crystal planes, see Chapter 5. A graph of the thermal vibration

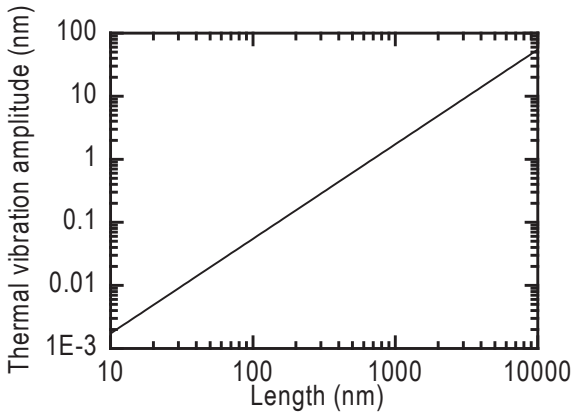


Figure 4.13 Thermal vibration amplitude at a temperature of 300 K as a function of length for a MWNT with inner and outer diameter of 2.5 and 5 nm, respectively. A Young's modulus of 1 TPa was used. To limit vibrations below 0.34 nm – the MWNT wall separation distance – a maximum MWNT length of ~340 nm was calculated.

amplitude as a function of CNT length is given in Figure 4.13, calculated using the equation by Treacy et al..[18] Furthermore, such probes are also ideal to use as scanning probe microscopy tips. A disadvantage of probes that are too short, however, is the possibility of electron emission from the tungsten support tip if the electric field there is high enough. Too prevent this, tungsten tips were etched with a radius of curvature approximately an order of magnitude larger than the CNT diameter.

References

1. V. A. Ryzhkov, Bulk Production and Applications of Naturally Short Carbon Multi Wall Nanotubes (2008).

2. V. A. Ryzhkov. Carbon nanotube production by a cracking of liquid hydrocarbons. *Phys. B* **323**, 324-326 (2002).

3. V. A. Ryzhkov. Short carbon nanotubes. 7244408 10490606 (2007)

4. R. Bandyopadhyaya, E. Nativ-Roth, O. Regev and R. Yerushalmi-Rozen. Stabilization of Individual Carbon Nanotubes in Aqueous Solutions. *Nano Lett.* **2**, 25-28 (2001).

5. M. A. Doytcheva, E. C. Heeres, M. Kaiser, and N. de Jonge. Developing purification protocols for arc discharge grown multiwalled carbon nanotubes applied for field emitter fabrication. *Philips Research Technical Note* **PR-TN2005-00232** (2008).

6. A. M. Morales and C. M. Lieber. A Laser Ablation Method for the Synthesis of Crystalline Semiconductor Nanowires. *Science* **279**, 208-211 (1998).

7. E. P. A. M. Bakkers, J. A. van Dam, S. De Franceschi, L. P. Kouwenhoven, M. Kaiser, M. Verheijen, H. Wondergem and P. van der Sluis. Epitaxial growth of InP nanowires on germanium. *Nat. Mater.* **3**, 769-773 (2004).

8. M. H. van Es. A new touch to atomic force microscopy: smart probing of biological and biomedical systems at the nanoscale. Ph.D. thesis, Leiden University (2008).

9. T. D. Yuzvinsky, A. M. Fennimore, W. Mickelson, C. Esquivias and A.

Zettl. Precision cutting of nanotubes with a low-energy electron beam. *Appl. Phys. Lett.* **86**, 053109-3 (2005).

10. D. van Baarle. Manipulating carbon nanotubes. B.Sc. thesis, Leiden University (2007).

11. T. D. Yuzvinsky, W. Mickelson, S. Aloni, S. L. Konsek, A. M. Fennimore, G. E. Begtrup, A. Kis, B. C. Regan and A. Zettl. Imaging the life story of nanotube devices. *Appl. Phys. Lett.* **87**, 083103 (2005).

12. H. Y. Chiu, V. V. Deshpande, H. W. C. Postma, C. N. Lau, C. Miko, L. Forro and M. Bockrath. Ballistic Phonon Thermal Transport in Multiwalled Carbon Nanotubes. *Physical Review Letters* **95**, 226101-226104 (2005).

13. H. W. P. Koops, R. Weiel, D. P. Kern and T. H. Baum. High-resolution electron-beam induced deposition. *J. Vac. Sci. Technol. B* **6**, 477-481 (1988).

14. A. P. J. M. Botman. Towards high purity nanostructures from electron beam induced deposition of platinum. Technische Universiteit Delft (2009).

15. A. Botman, M. Hesselberth and J. J. L. Mulders. Improving the conductivity of platinum-containing nano-structures created by electron-beam-induced deposition. *Microelectronic Engineering* **85**, 1139-1142 (2005).

16. N. de Jonge, M. Allioux, J. T. Oostveen, K. B. K. Teo and W. I. Milne. Low noise and stable emission from carbon nanotube electron sources. *Appl. Phys. Lett.* **87**, 133118 (2005).

17. S. T. Purcell, P. Vincent, C. Journet and V. T. Binh. Hot Nanotubes: Stable

Heating of Individual Multiwall Carbon Nanotubes to 2000 K Induced by the Field-Emission Current. *Phys. Rev. Lett.* **88**, 105502 (2002).

18. M. M. J. Treacy, T. W. Ebbesen and J. M. Gibson. Exceptionally high Young's modulus observed for individual carbon nanotubes. *Nature* **381**, 678-680 (1996).

5

Making carbon nanotube electron sources of defined lengths and with closed caps

A method is reported to make an electron source consisting of an individual multi-walled carbon nanotube (MWNT) mounted on a tungsten support tip, and cut to length using localized electron beam irradiation in a scanning electron microscope. The apex of the MWNT was transformed into a closed cap with at least one fullerene-like layer via an annealing process involving simultaneous heating and the extraction of an emission current of 1 μA. The electron emission occurred at localized emission sites. The electron emission showed Fowler–Nordheim behavior, was highly stable with time, and exhibited a low energy spread. The structure of the caps of two MWNTs was studied with transmission electron microscopy before and after the cap closure.

This chapter is based on the following publication:
Erwin C. Heeres, Tjerk H. Oosterkamp and Niels de Jonge, Making carbon nanotube electron sources of defined lengths and with closed caps, *Nanotechnology* **22**, 235308 (2011).

5.1 Introduction

Carbon nanotubes (CNTs) have been extensively studied for their use as next generation electron sources in electron microscopy, x-ray microscopy, and scanning probe microscopy.[1,2] A CNT with a closed apex serving as emission site has proven to yield much higher stability of the emitted current than cold field emission sources made of tungsten.[3,4] The emission site consists of covalently bound carbon atoms,[5] and is highly stable under the harsh conditions of field emission; a lifetime of over two years of continuous operation was demonstrated.[1] The apex can also be open, but then the emission current shows fluctuations larger than 10% with time.[6] For an electron source to exhibit a stable current it is thus needed to obtain a CNT with a closed cap, either by direct growth of a CNT with a closed cap on a support tip,[7] or by closing the cap.[8] To create a closed cap, the otherwise flat, hexagonal lattice needs to be curved.[5] This curvature is induced by the introduction of pentagonal carbon rings (pentagons).[9] A complication with the use of CNTs is that long and thin CNTs tend to vibrate,[10] which broadens the virtual source size and thus limits the brightness in microscopy applications. It is thus necessary to ensure that the freestanding fraction of a CNT is short enough. In this paper, we describe a new method to cut the freestanding part of a multi-walled carbon nanotube (MWNT) mounted on a support tip to a desired length via electron beam irradiation, and a procedure to close the apex subsequently. We have studied the morphology of the tip with transmission electron microscopy (TEM) and with field emission microscopy (FEM), and characterized the field emission properties.

5.2 Cutting a carbon nanotube to length

MWNTs were mounted on tungsten support tips on heating filaments, and then cut to a desired length using electron beam irradiation. The ideal length of the fraction of a MWNT protruding from a tungsten support tip for our samples was 200 nm. This length was sufficiently long to provide a strong improvement of the field enhancement with respect to a bare tungsten tip with a radius of curvature of 200 nm, and short enough to prevent thermal vibrations from occurring for MWNTs of diameters 10 nm.[10] A single MWNT was mounted on a support tip using a custom built piezo nanomanipulator inside a scanning electron microscope (SEM), see the

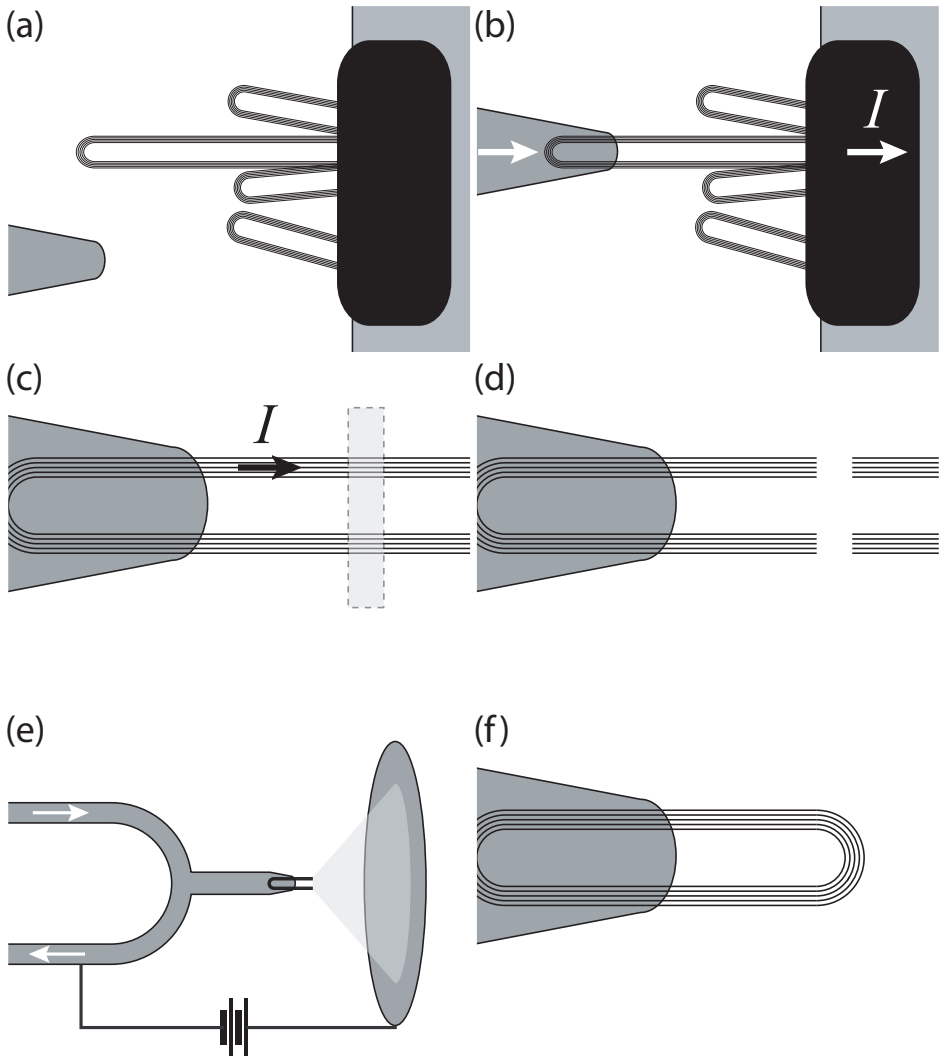


Figure 5.1 Schematic representation of the experiments with multi-walled carbon nanotube (MWNT) electron sources. (a) Selecting a MWNT protruding from a sample and approaching it with a tungsten tip. (b) The tungsten tip was attached to the MWNT. An electrical current was measured, induced by a bias voltage between tip and sample. (c) A selected area of the MWNT was irradiated with an electron beam in a scanning electron microscope (SEM) to (d) cut the MWNT to a desired length. (e) For electron emission measurements the MWNT on a tungsten tip on a heating filament was placed in front of a micro-channel plate, serving also as extractor electrode. (f) After simultaneous heating and electron emission the initial open cap of the MWNT closed.

mounting procedure described in Chapter 4.2.[11,12] The MWNT material was first glued to a carbon tape put on the edge of a metal foil for support in such a way that MWNTs protruded from the edge and thus could be approached with an etched tungsten tip for mounting, see Chapter 4.1.

Figures 5.1a and b show a schematic representation of the mounting steps of approaching a MWNT with a tip and attaching it to the tip. After attachment of a MWNT to the tungsten tip, a current was measured between the MWNT sample and the tungsten tip. To be able to cut a MWNT to a desired length we have adapted cutting methods based on electron beam irradiation,[13,14] providing a better control over the length than our previous method of breaking at the location of a thin spot in the structure,[11] or breaking at large currents.[15] The electron beam of the SEM (FEI, Nova NanoSEM) was focused on the section of the nanotube to be cut. A schematic representation of the main steps involved in the cutting is shown in Figures 5.1c and d. A reduced area-scan was used to irradiate the section to be cut, after zooming in up to a field of view of typically 50 nm × 10 nm, rotated such that only a length of 10 nm of the MWNT was irradiated. We used a beam current of 5.6 nA, and an acceleration voltage to 15 kV. To avoid carbon deposition, the SEM chamber was cleaned beforehand using a plasma cleaner (XEI Scientific, Evactron) installed on the SEM. The current was also used to monitor the instant of breaking. As soon as the current dropped to zero the electron beam was blanked. Note that an oxide-free tip was required for successful mounting; the contact resistance between the tungsten tip and the CNT was typically 100 kΩ – 300 kΩ. Water vapor was added into the vacuum chamber of the SEM via a needle-valve inlet, raising the pressure from 1×10^{-6} mbar up to 5×10^{-5} mbar. The MWNT mass loss due to electron beam irradiation with added water vapor is considered to be caused by the reaction of the carbon atoms with radicals, created by the radiolysis of water molecules, as proposed by Yuzvinsky et al..[13] At this pressure the time to cut through a MWNT was typically 1 minute. Using the method described above, we successfully mounted and cut ten MWNT samples. From these samples, five were imaged and characterized in a TEM, after which four samples were tested in the UHV field emission setup. Three samples showed a significant change in field emission microscopy (FEM) pattern. Two of these are described in this paper,

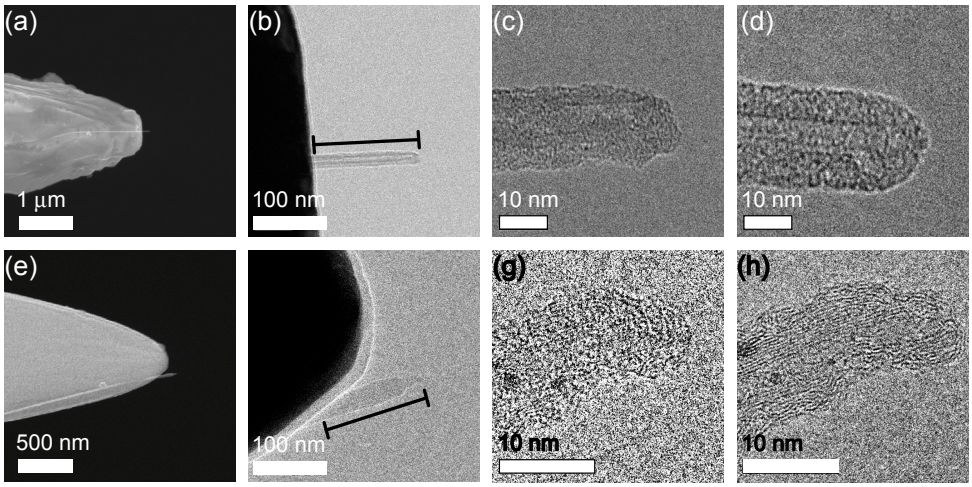


Figure 5.2 SEM and TEM images of two MWNTs before and after cap closing. (a) SEM image and (b)-(c) TEM images of MWNT #1 recorded after mounting and cutting to a length of 150 nm. (d) TEM image of MWNT #1 after electron emission and heating, leading to cap closing. (e) SEM image and (f)-(g) TEM images of MWNT #2 after mounting and cutting. (h) TEM image of MWNT #2 after cap closing.

MWNT #1 and MWNT #2, the third was lost after operating it at an emission current >6 µA; note that at such an emission current level, a MWNT is likely to be damaged destructively.[8] The fourth sample was lost while aligning it inside the vacuum chamber, probably due to a bad attachment of the MWNT to the tungsten tip, as it had a significantly smaller contact length than the other tested samples, <1 µm. From these results a success rate of 1/2 could be derived; however, the number of samples studied is low. The success ratio could be improved upon by using samples with a minimum contact length of 1.5 µm and by limiting emission current to values below 1 µA. The two MWNTs #1 and #2, cut with this method, are shown in Figures 5.2a and e. Using the SEM, MWNT #1 was set to be cut at a length of 150 nm and MWNT #2 at 170 nm. In order to study the effect of the cutting process on the morphology of the cap of the CNT, the two samples were imaged in a transmission electron microscope (TEM), see Figure 5.2. MWNT #1 exhibited a length of 143 ± 1 nm and MWNT #2 had a length of 141 ± 4 nm. These lengths were measured from TEM images obtained at 0° stage tilt and defined as the protruding length from the tungsten tip to the apex, as indicated with a black line

Table 5.1 Geometrical properties of mounted multi-walled carbon nanotubes (MWNTs), including the length protruding from the tungsten support tip (l), the outer diameter of the MWNT at the apex (d_o), and the inner diameter at the apex (d_i).

Parameter	MWNT #1	MWNT #2
l (nm)	143	141
d_o (nm)	12.8	10.2
d_i (nm)	6.3	2.4

in Figures 5.2b and f. The discrepancy in set length and obtained length of MWNT #2 is explained by a layer of material, most likely amorphous carbon deposited during imaging, which hides 30 nm of the MWNT. The dark horizontal lines visible in Figure 5.2c of MWNT #1, indicating the walls of the nanotube shaft, terminate into an amorphous structure at the right-hand side. The nanotube does not have a crystalline cap structure. The TEM image of MWNT #2 shown in Figure 5.2g shows more structural details of the walls of the nanotube, but also for this sample the cap consisted of amorphous material. Despite the fact that the electron beam irradiation of the MWNT was localized to a section with a length of only 10 nm, a sharp cut was not obtained, which would have resulted in a pronounced carbon nanotube structure up to the last 5 nm – 10 nm of the MWNT. The cutting process caused structural damage over a larger distance than the irradiated area, presumably due to a combination of deposition of carbon, drift of the electron beam, and mechanical instabilities of the setup.[12] The crystalline nanotube structure of the pristine MWNT #1 appears to have been damaged to a larger extent than was the case for MWNT #2. The measured dimensions of the MWNT tips are summarized in Table 1.

5.3 Closing the cap of a MWNT

We have investigated the electron emission from MWNTs mounted on tungsten support tips and cut to length via electron beam irradiation. The MWNTs were loaded in an ultra-high vacuum (UHV) system with a base pressure of 10^{-9} mbar for field emission microscopy (FEM). A tungsten tip on a heating filament was placed at a distance of a few centimeters in front of a micro-channel plate (MCP)

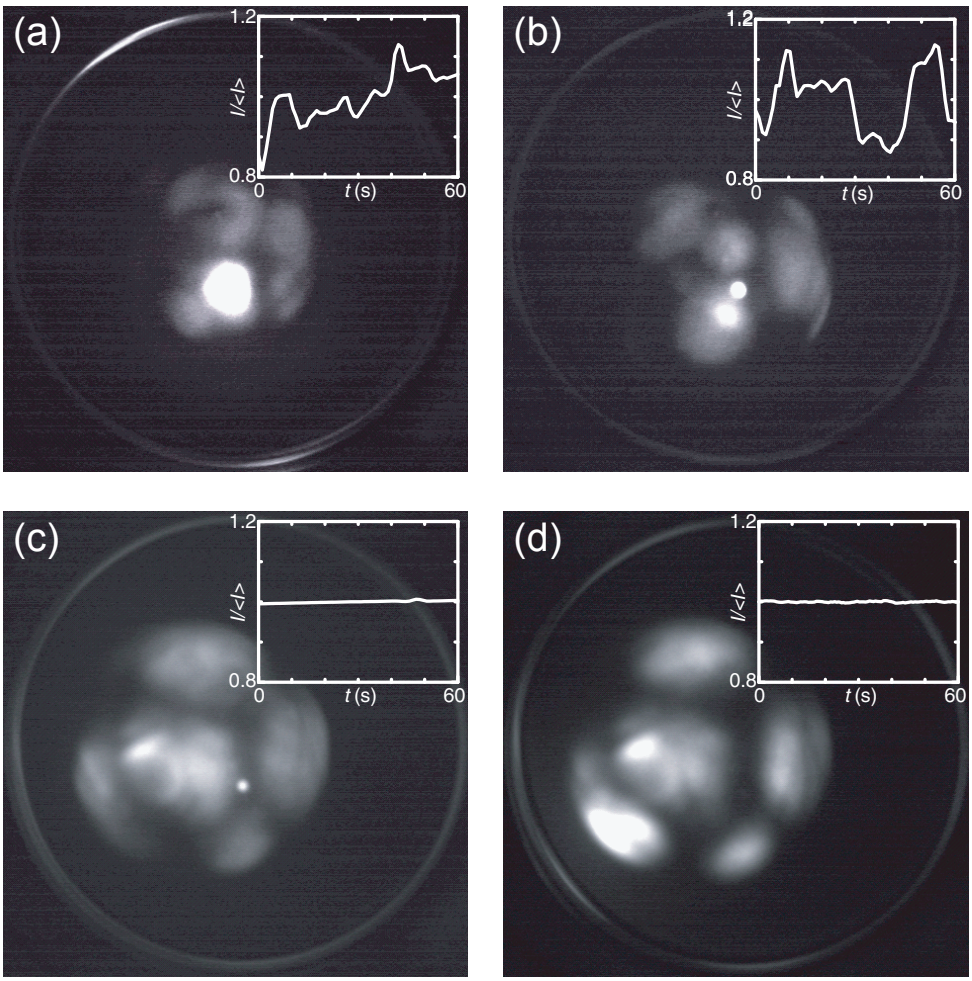


Figure 5.3 Field emission microscopy of the emitting surface of MWNT #1. (a) Emission pattern recorded at an average emission current $\langle I \rangle$ = 1.0 nA and an extraction potential U = 1472 V applied between the tip and the micro-channel plate with an active area of diameter 30 mm. The emitter was heated to a temperature $T \sim$ 500 °C. The normalized emission current $I/\langle I \rangle$ versus time t is shown in the inset. (b) Emission pattern recorded 11 minutes after (a) with $\langle I \rangle$ = 1.1 nA, U = 1500 V, and $T \sim$ 800 °C. The sharp round spot in the middle is an artifact of the micro-channel plate. (c) Emission pattern recorded after the current had stabilized, taken 204 minutes after (a) with $\langle I \rangle$ = 751 nA, U = 1155 V, and $T \sim$ 800 °C. (d) Emission pattern after 12 hours of continuous operation since stabilization occurred, with $\langle I \rangle$ = 91 nA, U = 932 V, and $T \sim$ 500 °C.

and phosphor screen (Hamamatsu), as shown in the schematic of Figure 5.1e; readout was with a CCD camera. To achieve a stable emission current, the samples were first annealed by heating. The temperature was slowly increased to 800 °C, as determined from the color of the filament, over a period of 7 min, until the vacuum level decreased to 10^{-7} mbar. The temperature of the tip of the filament was then decreased to 500 °C, and after the vacuum had recovered to a level of 10^{-9} mbar, the emission was initiated by applying a voltage difference between the MCP and the tip. The emission pattern of MWNT #1 is shown in Figure 5.3a, at an average emission current $\langle I \rangle$ of 1.0 nA. Several separated spots are visible, indicating distinct emission sites. The normalized emission current $I/\langle I \rangle$, shown in the inset, changed by about 20% over a time period of 60 seconds. During this 2 hour period we gradually increased the heating current to 800 °C, aiming to stabilize the emission current, while we recorded movies of the FEM pattern at the same time. The emission pattern continuously changed its shape (e.g., Figure 5.3b), and current changes of an order of magnitude occurred. Since this procedure did not lead to a stable emission current we ramped down the extraction potential and the heating current to zero. The filament was then heated again to a temperature of 600 °C. The emission was restarted, while ramping up the extraction potential such that an emission current of several tens of nanoamperes was maintained. After 0.5 hour we gradually increased the emission current up to 200 nA at 1000 V, briefly waited, and then increased the extraction potential with two additional steps of 100 V up to 1200 V. Suddenly, the current jumped up to about a microampere. We immediately reduced the potential to 1100 V. Hereafter, the current was stable at a level of 390 nA with maximal changes in $I/\langle I \rangle$ of 0.65%, see Figure 5.3c. The temperature was then reduced to 500 °C, the extraction potential reduced, and the current was monitored for a period of 12 hours. Figure 5.3d, recorded at the end of the 12 hour period, exhibits the same emission pattern and emission stability as in Figure 5.3c. We assume that the initial instability of the emission current was caused by instabilities of the structure of the cap of the MWNT during the emission, and local variations of the work function.[8,16] The observation of a stable current after the emission had reached the microampere level, while being heated, is consistent with the idea of cap closure, after which the emitting surface increases in stability.[8] The FEM pattern of Figure 5.3d shows several stable and localized emission sites,

similar to what was found in other studies of carbon nanotube electron sources with closed caps.[8,16,17] However, we did not observe interference fringes, which are observed for certain types of closed carbon nanotubes.[9] MWNT #2 was annealed with a similar procedure, and its cap was closed. The nanotubes were studied with TEM after the FEM experiments to verify the occurrence of cap closure, see Figures 5.2d and h. In Figure 5.2d of MWNT #1 a black line closed the interior of the nanotube, which can be interpreted as a closed cap with one fullerene-like layer. The exterior was still covered by amorphous material. MWNT #2 gained a fullerene-like structure at the cap during the emission experiments; amorphous material is absent in Figure 5.2h. The cap appears to be closed by a single carbon layer. However, the layers of carbon are not oriented crystalline, but still 'wavy' and fragmented. From these experiments it can be concluded that a combination of heating and electron emission causes at least one fullerene-like wall to close at the emitting apex of an open MWNT. We propose that the cap closing (or formation of a graphene layered cap from the amorphous material present after cutting) is caused by field emission current induced heating of the apex of the MWNT,[18] probably up to a temperature 1500 °C, which is well above the graphitization temperature.[5] Crucial in the process is to achieve the temperature at the MWNT apex, while not heating the tungsten tip too much, which leads to destabilization of the contact of the MWNT on the tip.

5.4 Electron emission characterization

An electron source made from a closed MWNT is expected to emit electrons via the process of field emission for a work function of 5 eV.[1] The electron emission behavior of MWNT #1 was characterized before being imaged in the TEM the second time. Its field emission energy distribution was measured using a hemispherical energy analyzer (VSW) in the same vacuum chamber used for FEM experiments. The central emission spot was selected by using a phosphor screen with an aperture, after which the energy distribution was measured. Figure 5.4a shows the emission spectrum recorded at a total emission current of 38 nA at 980 V. A fit with a function $J(E)$ of the expected energy spectrum of field emission was also included.[19] The current density as a function of the energy E is given by:

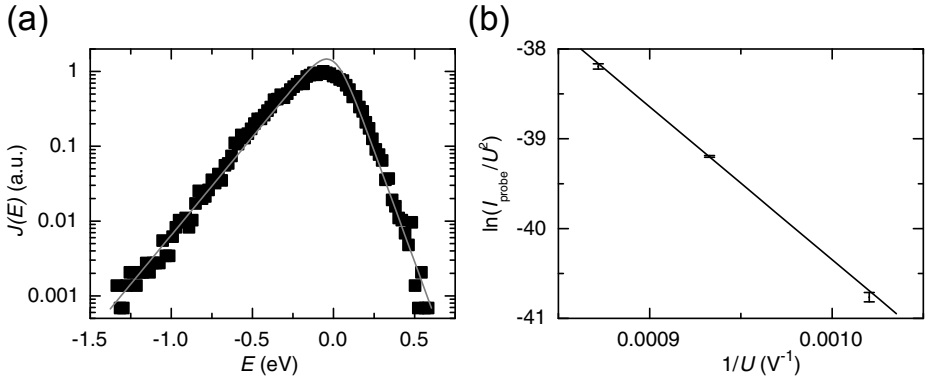


Figure 5.4 Electron emission characterization of MWNT #1. (a) Current density as a function of energy $J(E)$ versus E obtained at a total emission current of 38 nA. (b) Fowler–Nordheim plot of the probe current I_p and U. The emitter was heated to ~ 500 °C.

$$J(E) \propto \frac{\exp(E/d)}{1+\exp(E/k_B T)} \tag{5.1}$$

with tunneling parameter d, temperature T, and Boltzmann constant k_B. The fitted values were $d = 0.17$ eV and $T = 314$ °C, consistent with values found previously.[1] The shape of the theoretical curve approximately approaches the experimental curve, from which it can be concluded that field emission occurred. The energy spread, as measured from the full width at half maximum (FWHM) value of the peak in the energy spectrum, was $\Delta E_{\mathrm{FWHM}} = 0.36$ eV. This value was corrected for the broadening of the energy analyzed by subtracting 0.05 eV. The energy spread was determined for two other emission currents and increases with increasing extraction voltage as expected. The measured energy spread values compare to those obtained on thin closed MWNTs.[1] As a second test of the occurrence of field emission, we have measured the relation between the emitted probe current I_p, measured using a Faraday cup, and the extraction potential U. A linear relationship was found on the curve of $\ln\left(I_p/U^2\right)$ plotted as a function of $1/U$, see Figure 5.4b. A linear relation on this so-called Fowler–Nordheim curve is an indication of field emission.[20] The field factor β defined as $F = \beta U$, as determined from the

Fowler–Nordheim curve, amounted to $(4.4 \pm 0.1) \times 10^6$ m^{-1}.

5.5 Conclusions

Using the cutting method described in this paper, MWNTs protruding from support tips can be cut to length via electron beam irradiation. We demonstrated that it is possible to close the cap of a MWNT by a combination of heating and electron emission. TEM analyses of the cap before and after the experiments showed the formation of at least one closed fullerene-like layer at the initially open end of the MWNT. The cap closure was accompanied by a strong (better than a factor of twenty) stabilization of the emission current. The electron emission after cap closure was of field emission type. The obtained tips can be used for electron emission experiments, and for other applications, such as scanning tunneling microscopy, and atomic force microscopy.

References

1. N. de Jonge. Carbon nanotube electron sources for electron microscopes. *Advances in Imaging & Electron Physics* **156**, 203-233 (2009).

2. Y. Saito (Ed.) *Carbon Nanotube and Related Field Emitters: Fundamentals and Applications*. Wiley-VCH, Weinheim (2010).

3. N. de Jonge, M. Allioux, J. T. Oostveen, K. B. K. Teo and W. I. Milne. Low noise and stable emission from carbon nanotube electron sources. *Appl. Phys. Lett.* **87**, 133118 (2005).

4. J. F. Hainfeld. Understanding and using field emission sources. *Scan. Electron Microsc.* **1**, 591-604 (1977).

5. R. Saito, G. Dresselhaus and M. S. Dresselhaus *Physical properties of carbon nanotubes*. Imperial College Press, London (1998).

6. A. G. Rinzler, J. H. Hafner, P. Nikolaev, P. Nordlander, D. T. Colbert, R. E. Smalley, L. Lou, S. G. Kim and D. Tomanek. Unraveling Nanotubes: Field Emission from an Atomic Wire. *Science* **269**, 1550-1553 (1995).

7. M. Mann, K. B. K. Teo, W. I. Milne and T. Tessner. Direct growth of multi-walled carbon nanotubes on sharp tips for electron microscopy. *NANO: Brief Reports and Reviews* **1**, 35-39 (2006).

8. N. de Jonge, M. Doytcheva, M. Allioux, M. Kaiser, S. A. M. Mentink, K. B. K. Teo, R. G. Lacerda and W. I. Milne. Cap Closing of Thin Carbon Nanotubes. *Adv. Mater.* **17**, 451-455 (2005).

9. Y. Saito, K. Hata and T. Murata. Field Emission Patterns Originating from Pentagons at the Tip of a Carbon Nanotube. *Jpn. J. Appl. Phys.* **39**, L271-L272 (2000).

10. J. H. Hafner, C.-L. Cheung, T. H. Oosterkamp and C. M. Lieber. High-Yield Assembly of Individual Single-Walled Carbon Nanotube Tips for Scanning Probe Microscopies. *J. Phys. Chem. B* **105**, 743-746 (2001).

11. N. de Jonge, Y. Lamy and M. Kaiser. Controlled Mounting of Individual Multiwalled Carbon Nanotubes on Support Tips. *Nano Lett.* **3**, 1621-1624 (2003).

12. E. C. Heeres, A. J. Katan, M. H. van Es, A. F. Beker, M. Hesselberth, D. J. van der Zalm and T. H. Oosterkamp. A compact multipurpose nanomanipulator for use inside a scanning electron microscope. *Rev. Sci. Instrum.* **81**, 023704-1-023704-4 (2010).

13. T. D. Yuzvinsky, A. M. Fennimore, W. Mickelson, C. Esquivias and A. Zettl. Precision cutting of nanotubes with a low-energy electron beam. *Appl. Phys. Lett.* **86**, 053109-3 (2005).

14. E. C. Heeres, E. P. A. M. Bakkers, A. L. Roest, M. Kaiser, T. H. Oosterkamp and N. de Jonge. Electron Emission from Individual Indium Arsenide Semiconductor Nanowires. *Nano Lett.* **7**, 536-540 (2007).

15. M. Doytcheva, M. Kaiser and N. de Jonge. In situ transmission electron microscopy investigation of the structural changes in carbon nanotubes during electron emission at high currents. *Nanotechnology* **17**, 3226-3233 (2006).

16. K. A. Dean and B. R. Chalamala. Experimental studies of the cap structure of single-walled carbon nanotubes. *J. Vac. Sci. Technol. B* **21**, 868-871 (2003).

17. M. Khazaei, K. A. Dean, A. A. Farajian and Y. Kawazoe. Field Emission Signature of Pentagons at Carbon Nanotube Caps. *J. Phys. Chem. C* **111**, 6690-6693 (2007).

18. S. T. Purcell, P. Vincent, C. Journet and V. T. Binh. Hot Nanotubes: Stable Heating of Individual Multiwall Carbon Nanotubes to 2000 K Induced by the Field-Emission Current. *Phys. Rev. Lett.* **88**, 105502 (2002).

19. P. W. Hawkes and E. Kasper *Principles of electron optics*. Academic Press, London (1989).

20. S. Flügge (Ed.) R. H. Good and E. W. Müller *Handbuch der Physik, XXI*. Springer Verlag, Berlin (1956).

Size of the localized electron emission sites on a closed multi-walled carbon nanotube

We have measured the size of the localized electron emission sites on multi-walled carbon nanotubes (MWNTs) with caps closed by a fullerene-like structure. MWNTs were individually mounted on tungsten support tips and imaged with a field emission microscope (FEM). The magnification of the FEM was calibrated using electron ray tracing and verified by comparing transmission electron microscope images. The FEM image was also tested for effects of the lateral energy spread. We found ring-shaped emission areas with three flattened sides, of a radius of (1.7 ± 0.3) nm, and separated by (5 ± 1) nm.

This chapter was adapted from:
Erwin C. Heeres, Tjerk H. Oosterkamp, and Niels de Jonge, Size of the localized electron emission sites on a closed multi-walled carbon nanotube, *Phys. Rev. Lett.* **108**, 036804, (2012).

6.1 Field emission patterns from carbon nanotubes

Electron emission occurs from the apex of a carbon nanotube when placed in an electric field of sufficient strength in vacuum. The resulting electron beam exhibits a specific spatial distribution of electrons,[1] reflected in its emission pattern. Several different classes of patterns were found for nanotubes with closed caps and open caps.[1-4] Some groups found a more or less uniform pattern including a few broad spots.[3,5] For certain batches of nanotubes researchers have found a pattern containing typically six ring-shaped emission sites, and lines were observed between these sites. These lines are attributed to interference of electron waves emitted from the spatially separated emission sites.[6-8] The current hypothesis is that the rings in the emission pattern originate from the carbon pentagon rings in the cap,[1,4,8-13] with a radius of 1.2 Å.[14] A local electron source of such small size may lead to an extraordinary brightness even to the limit of degeneracy.[9,15] The emission patterns of carbon nanotubes were studied[1,4,8-13] with a field emission microscope (FEM).[16] But, because the magnification was not known in those experiments it was not possible to verify if the FEM images actually reflected spots of sizes of 1.2 Å. Here, we measure the size of the emission spots with a FEM with a calibrated magnification.

6.2 Field emission microscopy and its resolution

In a FEM, the carbon nanotube mounted on a metal support tip is placed in front of a phosphor screen, and an electric potential U is applied between the tip and the screen, leading to field emission. A magnified image of the emission surface is obtained at the screen on account of the geometric field enhancement at the tip. An important question is thus whether the resolution of the FEM is sufficient to resolve the atomic structure of the cap. The resolution of a FEM δ is given by[16,17]

$$\delta = \sqrt{\sqrt{\frac{2}{m_e e U}}\hbar k R + \frac{4\hbar F k^2 R^2}{\sqrt{2 m_e \phi}\, U}} \tag{6.1}$$

with electron mass m_e, elementary charge e, reduced Planck constant $\hbar$, image

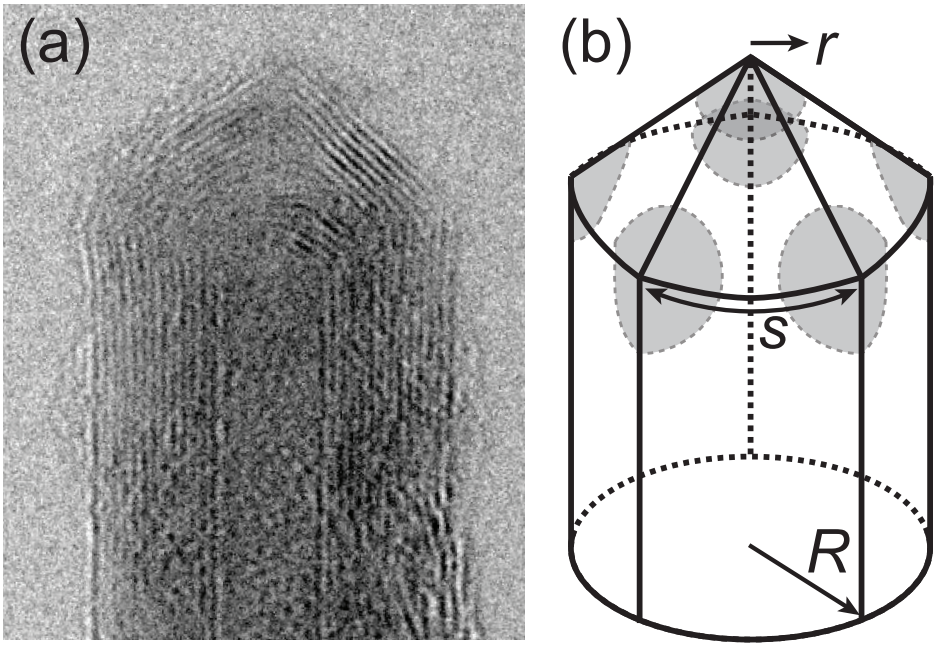


Figure 6.1 Multi-walled carbon nanotube (MWNT) with a cap closed by a fullerene-like structure. (a) Transmission electron microscope (TEM) image of a closed MWNT from the sample used in this study. (b) Simplified model of a hemispherically capped carbon nanotube, with localized emission sites (grey). Indicated are the size of the emission site r, distance between adjacent emission sites s and the carbon nanotube radius R.

compression factor k, emitter radius of curvature R, electric field strength F, and work function ϕ. For typical values of a multi-walled carbon nanotube (MWNT) electron emitter, $U = 500$ V, $k = 2.5$, and $R = 5$ nm, Equation (6.1) gives the FEM resolution $\delta = 1.1$ nm. Thus, the theoretical resolution is not sufficient to resolve an atomic structure.

6.3 Carbon nanotube model

Figure 6.1a shows a transmission electron microscope (TEM, FEI Tecnai 300 kV) image of the apex of a MWNT with a closed cap of a fullerene-like structure, as produced by the arc-discharge method.[18] The shape of the cap has characteristic flat sides and sharp edges, which are believed to be defined by the locations of

the pentagonal carbon rings,[19] with each pentagon inducing a local curvature of the otherwise planar structure of hexagonal carbon rings. Figure 6.1b shows a schematic representation of the electron emission sites mapped on the surface of the cap. The main goal of this Chapter is to measure the radius of an emission area (r). We will also determine the distance between the emission sites (s) and the radius of the total emission area including all spots (R), which should match the radius of the nanotube.

6.4 Mounting and TEM characterization

MWNTs with closed caps with a fullerene-like structure, and grown by an arc-discharge method (Rosseter),[18,20] were individually mounted on tungsten needles using a nanomanipulator (Omicron) inside a scanning electron microscope (Philips).[21,22] The adhesion of a nanotube to a tungsten tip was strengthened with the aid of the glue from carbon tape. The nanotube was detached from the bulk sample by careful pulling without breaking it, such that its closed cap remained intact.[23] More information about nanotube mounting procedures can be found in Chapter 4.2. In Figures 6.2a, b, d, and e two mounted nanotubes are depicted, referred to as MWNT 1 and MWNT 2, respectively, in the following text. MWNT 1 shows a kink, and it is supported by an additional shorter nanotube from which it protruded; see Figure 6.2a. An image of the closed cap of MWNT 1 is shown in Figure 6.2b. Presumably due to thermal vibrations of the nanotube,[24] the image of the cap is somewhat blurred, and its atomic structure cannot be revealed. MWNT 2, see Figures 6.2d and e, also exhibited a closed cap. The radii, (4.5 ± 0.5) nm and (5.5 ± 0.5) nm for MWNT 1 and 2, respectively, were measured as FWHM of a line profile through the image of the nanotube perpendicular to its length direction.

6.5 MWNT imaging inside the FEM

For FEM imaging each nanotube was placed in an ultrahigh vacuum chamber with a base pressure of 1×10^{-10} Torr in front of an imaging device consisting of a microchannel plate and a phosphor screen (Hamamatsu). To clean the nanotube emitter from adsorbed species, it was heated in vacuum for 10 minutes at a

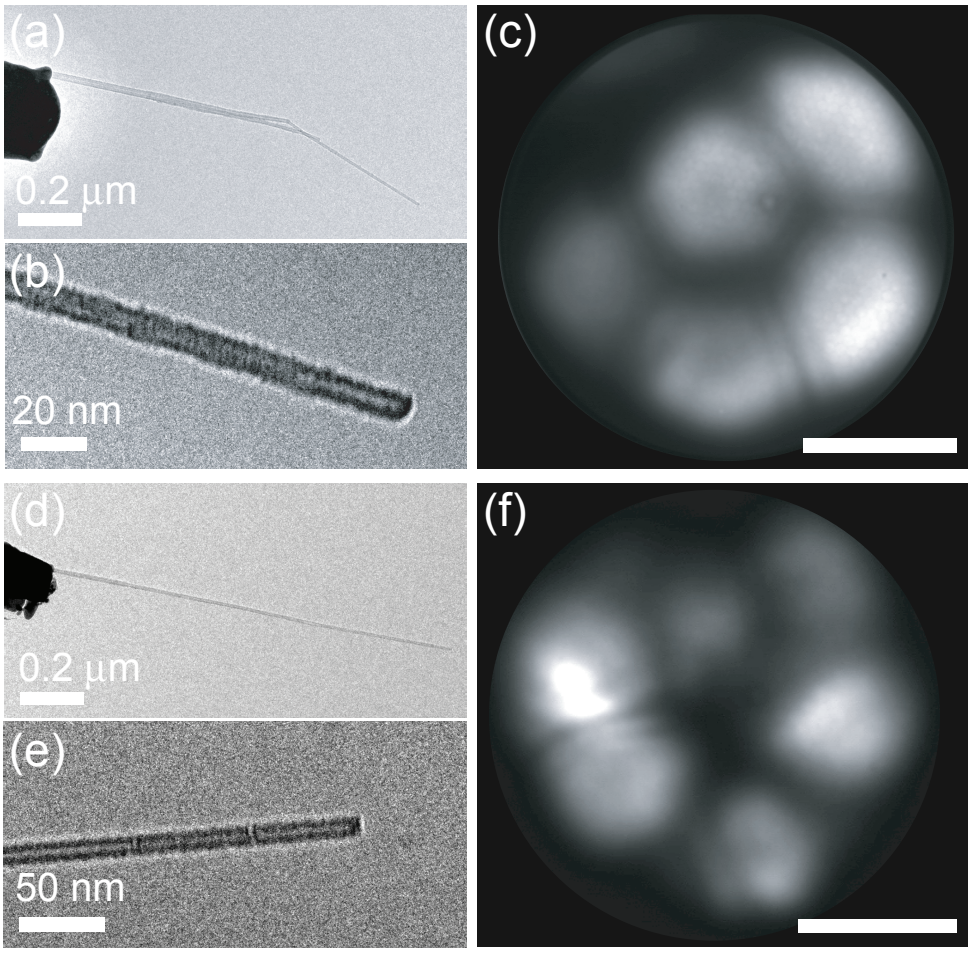


Figure 6.2 Microscopy of MWNTs individually mounted on tungsten support tips and used as field emission electron sources. (a),(b) TEM images of MWNT 1. (c) Field emission microscope (FEM) image obtained using MWNT 1 placed in front of a phosphor screen and microchannel plate at a distance of 24 mm. An extraction potential of $U = 406$ V was applied between the emitter and the screen, resulting in an emission current of $I = 292$ nA. The tip was heated up to ~500 ºC. The size of the scale bar equaled 10.5 mm on the original phosphor screen; and represents 5 nm in the FEM image using the calibrated magnification of 2100000. (d),(e) TEM images of MWNT 2. (f) FEM image of MWNT 2 obtained at $U = 420$ V, and $I = 102$ nA.

temperature of about 700° C prior to the experiments. A stable MWNT electron source showed maximal fluctuations of the current of 0.1%.[25] Figure 6.2c shows a FEM image of MWNT 1, with four spots oriented in a half-circle and one spot in

their middle. At the top edge of the phosphor screen a sixth spot is faintly visible. The presence of the sixth spot was verified by tilting the MWNT. Thus, the total number of spots equaled the number of pentagon dislocations needed to create a closed cap.[26] Between the two adjacent spots lines can be distinguished that are attributed to interference.[6-8]

6.5.1 Magnification of the FEM

To relate the emission patterns in Figure 6.2c to the atomic and electronic structure at the cap of the nanotube we calibrated the magnification of the FEM. This was done by using the equation for the magnification of a field emission microscope $M = z/kR$,[16] with z the tip-screen distance, k the image compression factor, and R the radius of curvature of the emitter. For our carbon nanotube R = 4.5 nm as determined from the TEM image, and z = 24 mm, but the image compression factor was unknown. Numerical calculations were performed to calculate the magnification of the FEM via ray tracing using Munro's electron beam software.

In order to check the validity of this method the magnification was first determined for a tungsten tip (without MWNT) with a hemispherically shaped apex with a radius of curvature of 100 nm on a tapered shank; see Figures 6.3a and b. From three different points near the emitter's apex, ray traces were simulated and the landing positions on the screen were obtained and used to calculate the magnification. The magnification was found by comparing the distances between the rays at the screen s_{screen} and at the emitter apex s_{tip}: $M = s_{screen} / s_{tip} = 1.4 \times 10^5$. The value k = 1.5 is known from literature for a tungsten tip,[16] yielding a theoretical value $M_{theory} = 1.6 \times 10^5$, which corresponds to the value obtained from ray tracing within 15%.

The carbon nanotube field emission tip was modeled as a cylinder with a hemispherically shaped apex on a conically shaped support tip, see Figure 6.3c and d, and it followed that $M = 2.1 \times 10^6$. Using $M = z/kR$, k = 2.5. Based on our TEM image of MWNT 1 we chose to simulate a hemispherical cap model. However, the cap of a carbon nanotube may exhibit sharp edges at the locations of the pentagons of carbon atoms in the cap with an angle of curvature 112.9°.[27] We calculated that the magnification for this geometry was maximal $M = 3.4 \times 10^6$, see Figures 6.3e and f, but this extreme case occurred only at the locations of the sharp edges. Note

that M will likely not be this large in reality due to field penetration, which reduces the extremity of the electric field at the edge.

6.5.2 Calibration and size of the FEM image

With the calibrated magnification in Figure 6.2c we can now determine the values of R, r and s. To compare the total size of the emission pattern with the diameter of the carbon nanotube we have to realize that the cap is a hemispherical surface that is mapped onto a flat screen. The diameter as measured on the screen d_{screen} corresponds to a distance measured along the surface of the cap with radius R_{FEM}, $d_{\text{screen}} = M \cdot \pi \cdot R_{\text{FEM}}$. At the longest side of the emission pattern d_{screen}/M equals 12.8 nm, which translates to a radius of the nanotube of R_{FEM} = (4.1 ± 0.6) nm. This corresponds to the value determined from the TEM image within the error margin. The fact that the value R_{FEM} and the value of R determined from the TEM image of Figure 6.2b are equal verifies the correct magnification calibration of the field emission microscope.

6.5.3 Sizes of individual spots

Values of r were obtained from line profiles through the center of each spot from which FWHM diameter values were calculated ($r = d_{\text{FWHM}}/2$) with respect to the minimum (background) intensity in the emission pattern. The individual spots were not exactly round and line profiles were taken over their short sides. Since an individual emission site reflected only a small solid angle of the total cap, a correction in mapping from a curved surface on a flat screen was neglected here. The average value of r of all five spots was (1.7 ± 0.3) nm. The average value of s (the distance between emission sites were corrected for curvature) amounted to (5.3 ± 1.0) nm. The values for MWNT 2 were $M = 1.6 \times 10^6$ (error 15 %), r = (1.6 ± 0.4) nm, s = (4.5 ± 0.9) nm, and R = (6.1 ± 0.9) nm.

6.6 Transverse energy distribution and deconvolution of the emission pattern

The distribution of the transverse energy of the transmitted electrons limits the resolution of the FEM. We have deconvolved the FEM image with the point spread

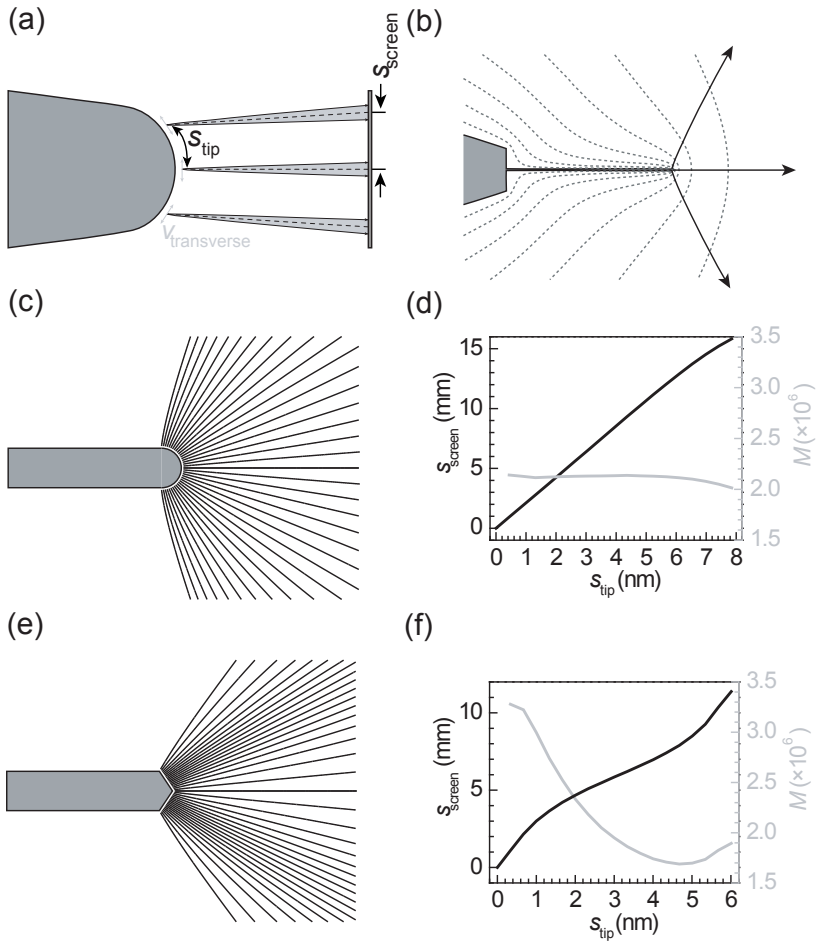


Figure 6.3 Geometry used for numerical calculations of the field factor and the magnification (M). Axial symmetry was assumed. (a) Schematic view of a tip in front of an anode (screen). The distance between the starting point of an electron trajectory and the apex of the cap, measured along the surface of the cap, is defined as s_{tip}. The distance from the symmetry axis to the point where the ray hits the screen is defined as s_{screen}. Three points are shown, where the electron ray tracing starts: either with zero transverse velocity (dashed black line) or with nonzero transverse velocity $v_{transverse}$ (solid black lines). The dimensions are not to scale. (b) The MWNT modeled as a cylinder on a support tip. Dotted black lines show equipotential lines and the solid black lines depict three electron trajectories. (c) Ray traces from a MWNT modeled with a hemispherical cap. All traces start with zero transverse energy at 0.5 nm from the apex to simulate the tunneling barrier. (d) Plot of the calculated values of s_{screen} (black, left axis) and M (gray, right axis) as a function of s_{tip}, using the model shown in (c). (e) Ray traces from a MWNTwith a pointed cap. (f) s_{screen} and M as a function of s_{tip}, using the model shown in (e).

function as obtained from the transverse energy distribution to increase the spatial resolution of FEM.

6.6.1 Energy distribution measurements

The field emission energy distribution of the emitted electron beam was determined by measuring energy spectra of the nanotube emitters using a hemispherical energy analyzer (VSW Atomtech Ltd.). Figure 6.4a shows the energy spectrum of MWNT 1, obtained at I = 130 nA and U = 470 V. The FEM images and shape of the energy spectrum suggest that the electron emission occurred via field emission. As verification, the current I was measured as a function of U. The plot of $\ln(I/U^2)$ versus $1/U$ was linear, and the field factor $\beta = F/U = (1.7 \pm 0.1) \times 10^7$ m^{-1}, indicating that field emission occurred[16] for the MWNT.[28]

The current density as a function of energy can be written as[29]

$$J(E) \propto \frac{\exp(E/d)}{1+\exp(E/k_{\mathrm{B}}T)} \tag{6.2}$$

where d is the tunneling parameter, k_{B} the Boltzmann constant, and T the temperature. Equation (6.2) was fitted to the data, resulting in $d = 0.34$ eV and $T = 601$ K.

6.6.2 Determining the PSF

The average transverse energy of the emitted electrons is equal to the tunneling parameter d.[16,30] The probability distribution for the transverse energy was obtained by integrating the product of the electron supply function and the transmission coefficient[16] over the normal energy range (-∞,0) yielding the transverse energy distribution $D(E_{\mathrm{transverse}})$:[30]

$$D\left(E_{\mathrm{transverse}}\right) \sim e^{-E_{\mathrm{transverse}}/d} \tag{6.3}$$

where d is the average value of the transverse energy:

$$\left\langle E_{\text{transverse}} \right\rangle = \frac{1}{2m}\left\langle {p_x}^2 + {p_y}^2 \right\rangle = d \tag{6.4}$$

For U = 470 V we simulated the electron trajectories for different transverse energies using Munro's electron beam software. The position deviation Δx from the trace of an electron with zero transverse energy was found to be proportional to the square root of the transverse energy, $\Delta x = \alpha\sqrt{E_{\text{transverse}}}$, with the proportionality constant $\alpha = 3.63 \times 10^{-3}\,\text{m}/\sqrt{\text{eV}}$. Substituting this result into Equation (6.3) we found that electrons with different transverse energies emitted from a single point on the carbon nanotube cap yield an intensity distribution of electrons on the screen given by

$$D\left(E_{\text{transverse}}\right) \sim e^{-\frac{(\Delta x/\alpha)^2}{d}} \tag{6.5}$$

6.6.3 Deconvolved field-emission pattern

The Gaussian distribution of Equation (6.5) was used as the point spread function to deconvolve the FEM image (using MATLAB). Figure 6.4b shows a much sharper image than Figure 6.2c. The individual emission sites show a dark center. The interference fringes between individual emission sites are more pronounced. Note that the superimposed honeycomb lattice is an artifact of the microchannel plate. The average radius of the emission sites as determined from the FWHMs of the emission patterns in Figure 6.4b amounts to r = (1.8 ± 0.4) nm, equal to the value determined from the original image within the error margin. Thus, even with the corrected FEM images, the radii of the emission sites are more than a factor of 10 larger than the size of an individual pentagon of carbon atoms.

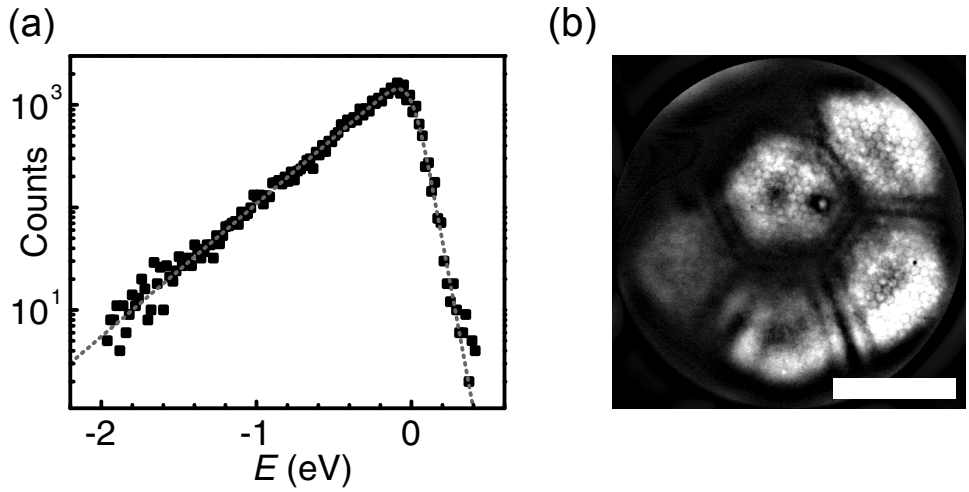


Figure 6.4 Deconvolution of the FEM image of MWNT 1. (a) Energy spread measurement of MWNT 1 obtained at 470 V and 130 nA. Dotted gray curve was the theoretical curve of field emission fitted to the data. (b) Deconvolved FEM image obtained using Figure 6.2(c). The scale bar represents 5 nm.

6.7 Conclusion and discussion

In conclusion, the emission surface of individual closed MWNT field emission sources was studied with FEM. The calibration of the magnification was verified using the radii of the MWNTs from TEM images. The emission originated from localized sites with $r = (1.7 \pm 0.3)$ nm, separated by $s = (5.3 \pm 1.0)$ nm on MWNT 1. For MWNT 2 we found $r = (1.6 \pm 0.4)$ nm and $s = (4.5 \pm 0.9)$ nm. The origin of the emission pattern can be understood as follows. The electron emission from a capped nanotube is known to occur from localized states present at the cap of a nanotube. Electron emission from several localized sites leads to interference of the electron beams, as can be observed as fringes in the emission pattern,[7] and these fringes flatten the sides of the spots where they are adjacent.[31] The emission spots show a dark region in their center. From our measurements it does not seem likely that the spots with dark center arise from emission sites of the size of single pentagons in the carbon lattice at the cap. If the emission would have occurred from single pentagons namely, the emission sites would have measured $r = 0.12$ nm. Such small sites would have appeared as small spots in the emission pattern on account of the limited resolution of the FEM, and not as spots with a dark center. The magnification of the FEM may have been enhanced at the sharp edges

of a MWNT, but not by more than a factor of 1.6. A localized emission site is an interruption of the delocalized π-system of the graphene lattice at the position of one of the bends in the structure needed to form the cap. The site extends over multiple carbon rings.[32,33] It is possible that local field penetration occurs, once electron emission starts, because the electron supply might be limited at interruptions of the electronic structure.[34]

References

1. Y. Saito, K. Hata and T. Murata. Field Emission Patterns Originating from Pentagons at the Tip of a Carbon Nanotube. *Jpn. J. Appl. Phys.* **39**, L271-L272 (2000).

2. Y. Saito, K. Hamaguchi, K. Hata, K. Uchida, Y. Tasaka, F. Ikazaki, M. Yumura, A. Kasuya and Y. Nishina. Conical beams from open nanotubes. *Nature* **389**, 554-555 (1997).

3. N. de Jonge, M. Doytcheva, M. Allioux, M. Kaiser, S. A. M. Mentink, K. B. K. Teo, R. G. Lacerda and W. I. Milne. Cap Closing of Thin Carbon Nanotubes. *Adv. Mater.* **17**, 451-455 (2005).

4. Y. Saito, Y. Tsujimoto, A. Koshio and F. Kokai. Field emission patterns from multiwall carbon nanotubes with a cone-shaped tip. *Appl. Phys. Lett.* **90**, 213108-3 (2007).

5. K. A. Dean and B. R. Chalamala. Experimental studies of the cap structure of single-walled carbon nanotubes. *J. Vac. Sci. Technol. B* **21**, 868-871 (2003).

6. C. Oshima, K. Mastuda, T. Kona, Y. Mogami, M. Komaki, Y. Murata, T. Yamashita, T. Kuzumaki and Y. Horiike. Young's Interference of Electrons in Field Emission Patterns. *Phys. Rev. Lett.* **88**, 038301 (2002).

7. K. Hata, A. Takakura, K. Miura, A. Ohshita and Y. Saito. Interference fringes observed in electron emission patterns of a multiwalled carbon nanotube. *J. Vac. Sci. Technol. B* **22**, 1312-1314 (2004).

8. G. L. Martin and P. R. Schwoebel. Field electron emission images of multi-walled carbon nanotubes. *Surf. Sci.* **601**, 1521-1528 (2007).

9. K. Hata, A. Takakura, A. Ohshita and Y. Saito. Brightness of electron beam emitted from a single pentagon on a multiwall carbon nanotube tip. *Surf. Interface Anal.* **36**, 506-509 (2004).

10. T. Yamashita, K. Mastuda, T. Kona, Y. Mogami, M. Komaki, Y. Murata, C. Oshima, T. Kuzumaki and Y. Horiike. Coherent electron emission from carbon nanotubes.: Young's interference in the emission patterns. *Surf. Sci.* **514**, 283-290 (2002).

11. M. Khazaei, K. A. Dean, A. A. Farajian and Y. Kawazoe. Field Emission Signature of Pentagons at Carbon Nanotube Caps. *J. Phys. Chem. C* **111**, 6690-6693 (2007).

12. T. Fujieda, M. Okai and H. Tokumoto. Energy Spread of Field Emission Electrons from Single Pentagons in Individual Multi-Walled Carbon Nanotubes. *Jpn. J. Appl. Phys.* **47**, 2021-2023 (2008).

13. T. Fujieda, K. Hidaka, M. Hayashibara, T. Kamino, H. Matsumoto, Y. Ose, H. Abe, T. Shimizu and H. Tokumoto. In situ observation of field emissions from an individual carbon nanotube by Lorenz microscopy. *Appl. Phys. Lett.* **85**, 5739-5741 (2004).

14. K. Hedberg, L. Hedberg, D. S. Bethune, C. A. Brown, H. C. Dorn, R. D. Johnson and M. De Vries. Bond Lengths in Free Molecules of Buckminsterfullerene, C60, from Gas-Phase Electron Diffraction. *Science* **254**, 410-412 (1991).

15. J. D. Jarvis, H. L. Andrews, B. Ivanov, C. L. Stewart, N. de Jonge, E. C. Heeres, W. P. Kang, Y. M. Wong, J. L. Davidson and C. A. Brau. Resonant tunneling and extreme brightness from diamond field emitters and carbon nanotubes. *J. Appl. Phys.* **108**, 094322-094326 (2010).

16. S. Flügge (Ed.) R. H. Good and E. W. Müller *Handbuch der Physik, XXI*.

Springer Verlag, Berlin (1956).

17. The original equation by Good & Müller lacks a factor of two in the transverse energy part of the broadening, which has been corrected for.

18. V. A. Ryzhkov. Carbon nanotube production by a cracking of liquid hydrocarbons. *Phys. B* **323**, 324-326 (2002).

19. S. Iijima. Growth of carbon nanotubes. *Mater. Sci. Eng. , B* **19**, 172-180 (1993).

20. V. A. Ryzhkov. Short carbon nanotubes. 7244408 10490606 (2007)

21. J. H. Hafner, C.-L. Cheung, T. H. Oosterkamp and C. M. Lieber. High-Yield Assembly of Individual Single-Walled Carbon Nanotube Tips for Scanning Probe Microscopies. *J. Phys. Chem. B* **105**, 743-746 (2001).

22. N. de Jonge, Y. Lamy and M. Kaiser. Controlled Mounting of Individual Multiwalled Carbon Nanotubes on Support Tips. *Nano Lett.* **3**, 1621-1624 (2003).

23. E. C. Heeres, A. J. Katan, M. H. van Es, A. F. Beker, M. Hesselberth, D. J. van der Zalm and T. H. Oosterkamp. A compact multipurpose nanomanipulator for use inside a scanning electron microscope. *Rev. Sci. Instrum.* **81**, 023704 (2010).

24. M. M. J. Treacy, T. W. Ebbesen and J. M. Gibson. Exceptionally high Young's modulus observed for individual carbon nanotubes. *Nature* **381**, 678-680 (1996).

25. N. de Jonge, M. Allioux, J. T. Oostveen, K. B. K. Teo and W. I. Milne. Low noise and stable emission from carbon nanotube electron sources. *Appl. Phys. Lett.* **87**, 133118 (2005).

26. S. Iijima, T. Ichihashi and Y. Ando. Pentagons, heptagons and negative curvature in graphite microtubule growth. *Nature* **356**, 776-778 (1992).

27. S. N. Naess, A. Elgsaeter, G. Helgesen and K. D. Knudsen. Carbon nanocones: wall structure and morphology. *Sci. Technol. Adv. Mater.* **10**, 065002 (2009).

28. N. de Jonge, M. Allioux, M. Doytcheva, M. Kaiser, K. B. K. Teo, R. G. Lacerda and W. I. Milne. Characterization of the field emission properties of individual thin carbon nanotubes. *Appl. Phys. Lett.* **85**, 1607-1609 (2004).

29. N. de Jonge, M. Allioux, J. T. Oostveen, K. B. K. Teo and W. I. Milne. Optical Performance of Carbon-Nanotube Electron Sources. *Phys. Rev. Lett.* **94**, 186807-4 (2005).

30. P. W. Hawkes and E. Kasper *Principles of electron optics*. Academic Press, London (1996).

31. P. Kruit, M. Bezuijen and J. E. Barth. Source brightness and useful beam current of carbon nanotubes and other very small emitters. *J. Appl. Phys.* **99**, 024315-024317 (2006).

32. A. Buldum and J. P. Lu. Electron Field Emission Properties of Closed Carbon Nanotubes. *Phys. Rev. Lett.* **91**, 236801 (2003).

33. A. De Vita, J. C. Charlier, X. Blase and R. Car. Electronic structure at carbon nanotube tips. *Appl. Phys. A: Mater. Sci. Process.* **68**, 283-286 (1999).

34. J. Peng, Z. Li, C. He, G. Chen, W. Wang, S. Deng, N. Xu, X. Zheng, G. Chen, C. J. Edgcombe and R. G. Forbes. The roles of apex dipoles and field penetration in the physics of charged, field emitting, single-walled

carbon nanotubes. *J. Appl. Phys.* **104**, 014310 (2008).

7

Electron emission from individual indium arsenide semi-conductor nanowires

A procedure was developed to mount individual semiconductor indium arsenide nanowires onto tungsten support tips to serve as electron field emission sources. This procedure could possibly find general application for the construction of nanowire probes for e.g. atomic force microscopy. The electron emission properties of the single nanowires were precisely determined by measuring the emission pattern, current-voltage curve and the energy spectrum of the emitted electron beam. The two investigated nanowires showed stable, Fowler-Nordheim-like emission behavior and a small energy spread. Their morphology was characterized afterwards using transmission electron microscopy. The experimentally derived field enhancement factor corresponded to the one calculated using the basic structural information. The observed emission behaviour contrasts the often unstable emission and large energy spread found for semiconductor emitters and supports the concept of Fermi-level pinning in indium arsenide nanowires. Indium arsenide nanowires may thus present a new type of semiconductor electron sources.

This chapter was adapted from:
Erwin C. Heeres, Tjerk H. Oosterkamp, and Niels de Jonge, Elecron emission from individual indium arsenide semiconductor nanowires, *Nano Lett.* **7**, 536 (2011).

7.1 Introduction

Semiconductor nanowires attracted considerable scientific interest on account of the prospect of tuneable electronic and optical properties.[1-3] Nanowires can serve a variety of applications, such as single-electron transistors,[4] sensors in life-science,[5] nanoscale optoelectronic devices,[6] and tunable superconductors.[7] Recently, it has been shown that near to ideal ohmic contacts to indium arsenide can be established due to Fermi-level pinning in the conduction band,[7,8] an effect that is known for bulk indium arsenide.[9-11] This effect may be used to construct a special type of field emission electron source from indium arsenide nanowires. Field emission electron sources made from sharp, semiconductor tips are often difficult to operate in a stable mode because the Fermi-level is below the conduction band. When an electric field is applied as needed for field electron emission, insufficient charge carriers are available to maintain a zero potential at the surface, leading to band bending. The resulting emission process is highly unpredictable and exhibits a large energy spread of several tens of electron volts of the emitted electron beam.[12] For this reason field emitters are usually made from a sharp metal tip,[13] or a tip of a material with metal-like electronic properties, such as a carbon nanotube.[14] Because of the occurrence of Fermi-level pinning for indium arsenide nanowires, this material could present a special case of a semi-conductor electron source with low energy spread.[15] In this letter, we will describe the construction of the electron source from individual indium arsenide nanowires, demonstrate electron emission, and provide a structural analysis of the emitter.

7.2 Sample preparation

Single-crystal indium arsenide nanowires grown on an oxidized silicon substrate using gold catalyst particles were produced with an optimized vapor-liquid-solid (VLS) laser ablation method described in detail elsewhere.[7,16,17] In short, the nanowires were grown on a thermally oxidized silicon substrate, which was covered with an equivalent of a 10 Å gold layer prior to the VLS process. The substrate was heated to approximately 500 °C in order to break up the thin gold film in an argon environment. Indium arsenide was evaporated from a corresponding target using an intense laser beam. The growth mechanism is believed to be

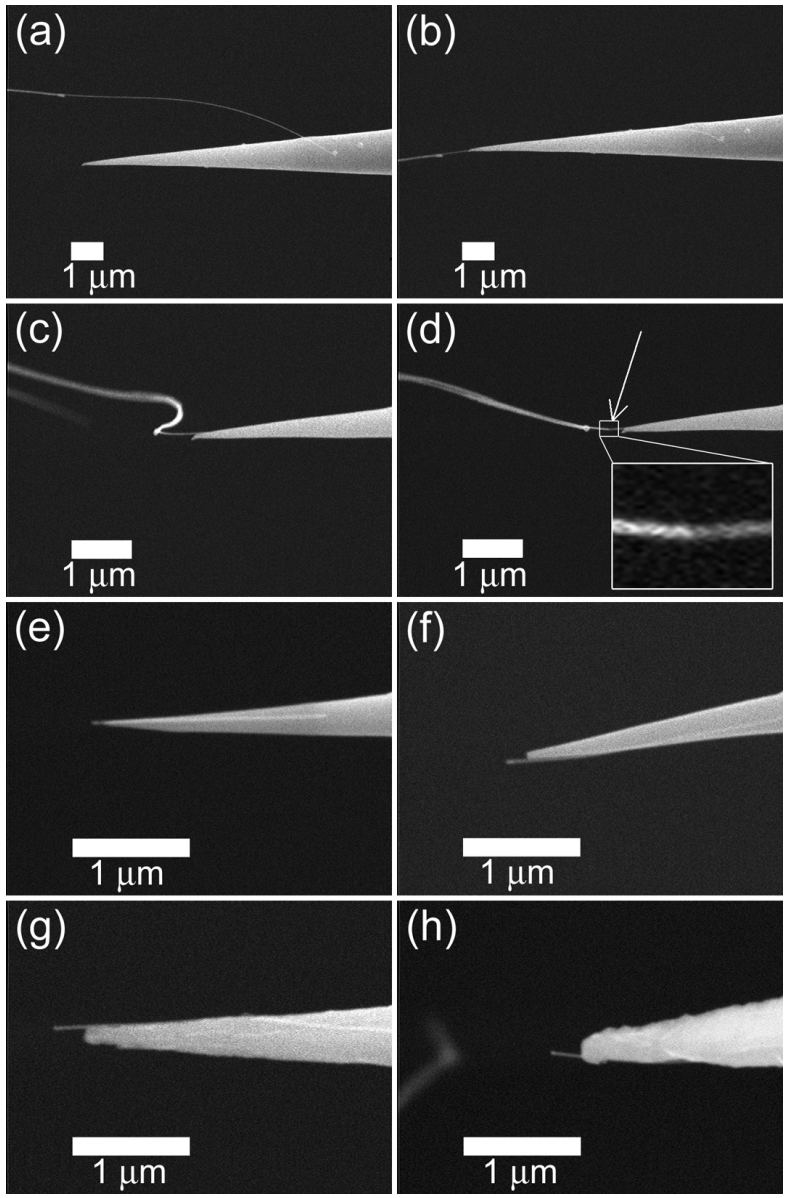


Figure 7.1 Mounting of an indium arsenide nanowire using nano-manipulators in a scanning electron microscope. (a) Attachment of the protruding nanowire, located on the mounting substrate, to a tungsten support tip. (b) Alignment of the nanowire with respect to the tungsten tip. (c) Bending of the nanowire due to lateral movement. (d) Image of the nanowire after irradiation at the desired break position with the electron beam, showing a contrast difference at this position (inset). (e)-(h) Four individually mounted nanowires with protruding lengths of 110, 180, 300 and 260 nm, respectively. The nanowires depicted in (g) and (h) are labeled nanowire I and nanowire II and used for the electron emission experiments.

the dissolving of indium and arsenic atoms in the locally formed gold droplets until supersaturation and the subsequent growth of the single-crystal nanowires. The growth procedure provided indium arsenide nanowires, with a free electron concentration of about 10^{18} cm^{-3}.[7] For the investigation of the emission behavior of the material, it is desirable to perform measurements on individually mounted nanowires. Nanowires were first transferred onto a gold-coated silicon substrate with a sharp edge (the mounting substrate) in such a way that the nanowires were oriented parallel to the surface and protruding over the edge. The procedure was performed with a micro-manipulator and an optical microscope, as described in more detail in Chapter 4. Next, a single nanowire was precisely mounted on a sharp tungsten support tip, in such way that (1) it was aligned with the axis through the support tip and (2) only a short length of the nanowire protruded from the support tip. The tungsten tip with a radius of curvature of 50 nm to 100 nm was obtained by electrochemical etching of a tungsten wire with a diameter of 0.3 mm that was laser-welded on a heating and support filament made of titanium. The mounting was performed in a scanning electron microscope (SEM), equipped with a nano-manipulator (Omicron),[18] see Figure 7.1. It is especially important to control the protruding length to minimize vibrations[19] and to prevent excessive Joule heating during field emission.[20] The mounting substrate was first searched for a clean, freestanding nanowire with no visible defects and protruding straight from the edge. The selected nanowire was then approached by the tungsten tip and attached to the tungsten tip, see Figure 7.1a. Prior to the mounting of a nanowire, the support tip was pressed into conductive carbon tape to apply some glue (hydrocarbons) for the attachment of the nanowire. The nanowire was aligned with the central axis of the tungsten tip by pulling, see Figure 7.1b. This alignment provided a contact between the nanowire and the tungsten tip, with a typical length of several micrometers. A strong attachment was obtained, and the nanowires could be bent strongly, see Figure 7.1c. The most difficult step in the mounting procedure was the controlled detachment of the nanowire from the mounting substrate, defining the length of the protruding nanowire. A new method was developed in which the desired break position could be determined within an accuracy of about 100 nm using electron beam irradiation. A mechanically weak position was induced in the nanowires by electron beam irradiation (operating the SEM in spot mode) until

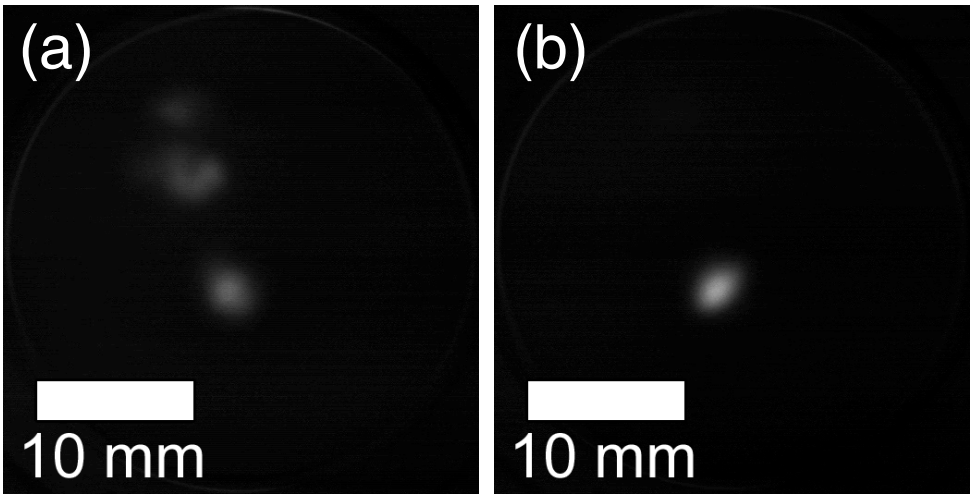


Figure 7.2 Emission patterns of nanowire II recorded after heat treatment recorded with a microchannel plate and a phosphor screen. (left) Emission pattern recorded directly after starting the emission with an extraction voltage of 444 V and 100 pA of emission current. (right) Emission pattern recorded after 30 min of emission for 449 V and 320 pA.

a contrast difference occurred on the material (Figure 7.1d). The current density of the electron beam amounted to 10 nA/μm^2. The nanowire broke at exactly the irradiated position upon applying a mechanical stress by withdrawing the mounting substrate. In Figures 7.1e-h, four mounted nanowires of different lengths are shown. A total of 10 nanowires with protruding lengths between 110 nm and 430 nm were mounted. All were tested for electron emission, but some were destroyed by operating them at too-high temperatures or emission current, as was observed by transmission electron microscopy (TEM). Other did emit electrons, but a too sharply etched tungsten tip started emitting as well at the typical extraction voltage needed to obtain emission from the nanowires. For two nanowires, all experiments could be completed successfully, as described in the next sections. The mounting procedure could possibly be used for other fields of research as well. For example, to mount nanowires on tips for atomic force microscopy (AFM), similar to what was done for carbon nanotubes.[19] Mounted on an AFM tip, the nanowires could serve as semiconductor probes of a precisely defined symmetry (i.e., nanorod). Additionally, the nanowires could also be functionalized with chemical groups.

7.3 Electron emission characteristics

The electron emission properties of two individual indium arsenide nanowires were characterized by the following experiments: (1) recording the emission pattern, (2) recording of the current-voltage curve, and (3) recording of the energy spectrum of the emitted electron beam. These experiments were performed in an ultrahigh vacuum chamber with a base pressure of 10^{-10} Torr. Prior to the characterization of the emission properties, each new sample was heated for 2 h at a temperature of approximately 250 ºC in order to clean the nanowires from volatile species. The temperature of the support tip was measured with an infrared pyrometer (Ircon). The emission pattern was used to check the stability and cleanness of the emitting surface.[21,22] In Figure 7.2, two emission patterns of nanowire II are shown. At first, the emission pattern consisted of several spots, which changed their positions with time, indicating a lack of stability or cleanness of the surface. By slowly increasing the emission current, the nature of the emission pattern changed with time. The maximal current was kept below 0.5 nA because it was found that current well above 10 nA led to a damaged structure, possibly due to Joule heating. A single stable bright spot in the emission pattern was finally obtained after running the emitter for 30 minutes. Similar results were obtained for nanowire I (data not shown). As has been observed previously for carbon nanotubes,[21,22] the fluctuating emission pattern could originate from species being adsorbed at the apex of the emitter and a consecutive change of the work function at that location. By Joule heating of the wire, during emission, the adsorbed impurities were evaporated from the emitter, leading to stable emission. Another possibility is a slight reshaping of the emission site, i.e. the nanowire apex, leading to an equilibrium indium arsenide structure under the influence of the strong electric field and Joule heating. Depending on the temperature and the field, the reshaping can either be dulling or sharpening of the tip. Dulling is often found for metallic electron sources and leads to a more homogeneous emission pattern.[23,24] Sharpening often leads to less emission stability, although special states in which a small tip on top of the main tip, a so-called super-tip, is formed, which may present a new stable configuration with a narrow emission beam.[25]

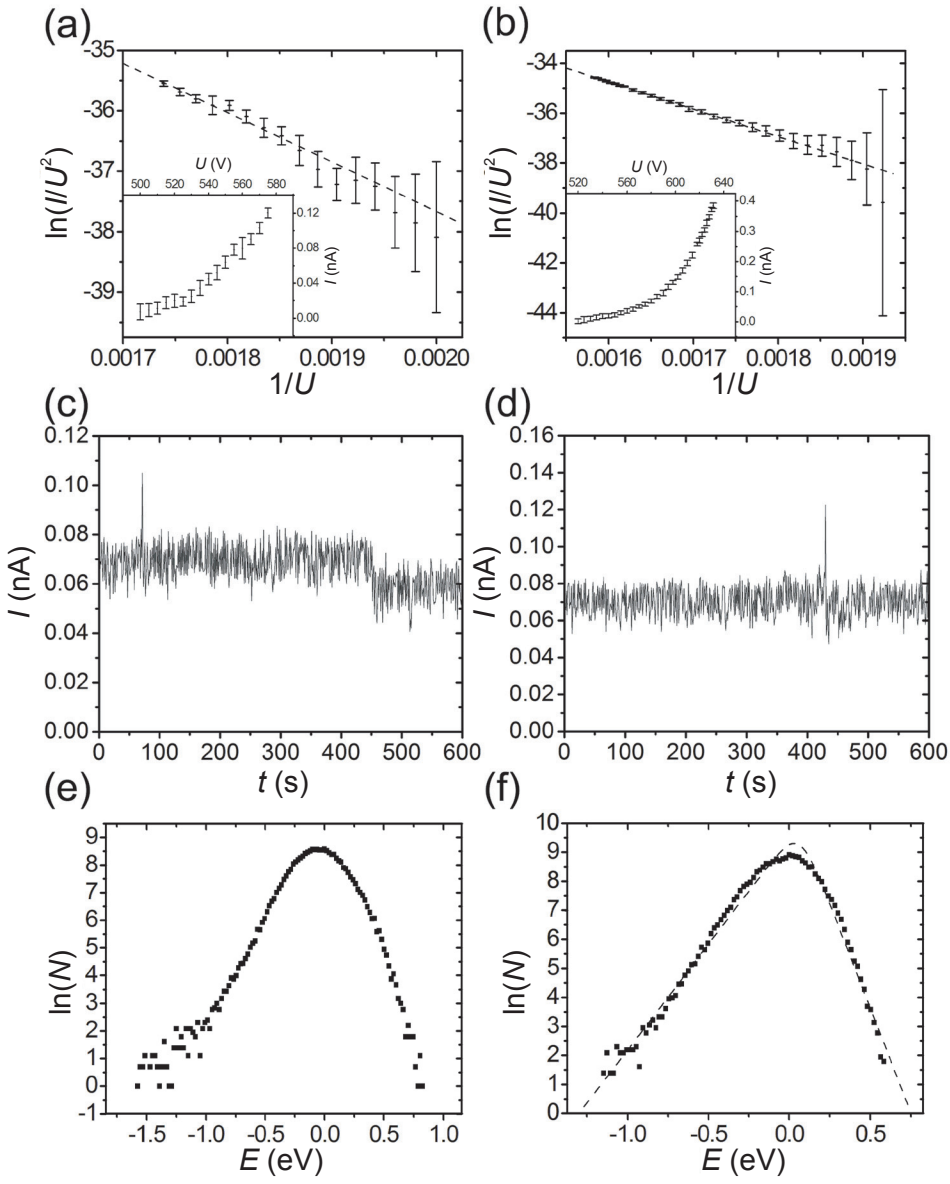


Figure 7.3 Characterization of the electron emission process of nanowire I (a,c,e) and II (b,d,f). In (a) and (b) the current-voltage characteristics are given in the form of the Fowler-Nordheim plot. The dashed lines represent fitting of the Fowler-Nordheim model to the data. The insets show the measured current-voltage curves. Plots of the emission current as a function of time are shown in (c) and (d). The extraction voltage is kept constant at 553 V and 582 V, respectively. Images (e) and (f) show the energy spectra of the emitted electron beam recorded at currents of 70 pA and 185 pA, respectively. A fit of the current density as a function of energy is also shown in (f) using a dashed line.

The electron emission process was further characterized by measuring the current-voltage curves of the two emitters, see Figures 7.3a and b. Current-voltage curves were recorded with a source meter (Keithley) and software of local design in Labview (National Instruments). Because of the Fermi-level pinning effect, we expect that the electron emission can be described by the Fowler-Nordheim field emission model.[26,27] The tunneling current density J through a potential barrier between a metal surface and vacuum in a modified equation of the Fowler-Nordheim model is given by:[14,28]

$$J = c_1 \frac{F^2}{b_1^2 \phi} \exp\left\{ a_2 c_2 c_3 \frac{1}{\sqrt{\phi}} \right\} \exp\left\{ -a_1 c_2 \frac{\phi^{3/2}}{F} \right\} \qquad (7.1)$$

with workfunction ϕ, electric field F and the constants $a_1 = 0.958$, $a_2 = 1.05$, $b_1 = 1.05$, $c_1 = e^3/8\pi h$, $c_2 = 8\pi\sqrt{2m}/3he$, $c_3 = e^3/4\pi\varepsilon_0$, with the electron mass m, Planck's constant h, the electron charge e, and permittivity of free space ε_0. Assuming a hemispherical shape of the emitting surface with radius R, a total emitted current of $I = 2\pi R^2 J$ is obtained. The sharp curvature of the emitting surface leads to field enhancement by a field factor β, $F = \beta U$, where U is the potential difference between anode and cathode. It thus follows that $\ln\left(I/U^2\right)$ is proportional to $1/U$, a plot of which is called a Fowler-Nordheim curve (see Figure 7.3a and b). Table 1 gives the values of the field enhancement factor β_{fit} and the radius of the emitting area R_{fit}, as obtained by fitting the data to the Fowler-Nordheim model and assuming $\phi = 4.9$ eV.[29] A linear relation in the measured current regime of up to 120 pA for nanowire I and 400 pA for nanowire II can be observed, indicating that a field emission mechanism occurs. Fowler-Nordheim behaviour was previously found for tips made of macroscopic samples of indium arsenide.[30] Because both nanowires emitted currents that were equal within a factor of 2 for the same voltage, it can also be concluded that both nanowires had similar properties and shapes.

To show the stability of the emission process, the emitted current was recorded at

constant extraction voltage as a function of time, see Figures 7.3c and d. Over a time period of 10 min, the measured current fluctuations are about 0.1 nA, close to the noise floor of our measurement system, with occasional spikes of the current.

A third important aspect of the emission process is the energy spectrum of the emitted electron beam. For a field emitter the current density as a function of energy E is given by the equation.[27]

$$J(E) \propto \frac{\exp(E/d)}{1+\exp(E/k_{\mathrm{B}}T)} \tag{7.2}$$

with k_{B} the Boltzmann constant, T the temperature, and d the tunneling parameter. Energy spectra were recorded for both nanowires (Figures 7.3e and f) with a hemispherical energy analyzer with a resolution of 50 meV (VSW). An energy spectrum was recorded shortly after the recording of the current-voltage curve and without changing the position of the nanowire. The widths of the spectra were determined by calculating the full width at half maximum (FWHM) and subtracting 50 meV to compensate for the broadening of the spectrum analyzer.[14] The beams coming from nanowires I and II had energy widths ΔE of 0.40 eV and 0.33 eV, respectively. These values are much smaller than the energy widths of emitters from silicon tips, which can amount up to several tens of eV.[12] The energy widths are comparable to the values of tungsten field emitters,[23] with ΔE = 0.3 eV and carbon nanotube emitters,[14] with ΔE = 0.35 eV (typically measured at currents of between 1 nA and 100 nA). This observation supports the conclusion that the nanowires exhibit field-emission-like behavior, as expected on account of the effect of Fermi-level pinning. It should be noted that the performance of semiconductor emitters can sometimes be enhanced by heavy doping. In the case of nanometer sized structures, however, the controlled doping level presents a serious problem due to the very small total number of doping atoms in the nanostructure for typical doping levels used in bulk materials.[30]

7.4 TEM analysis

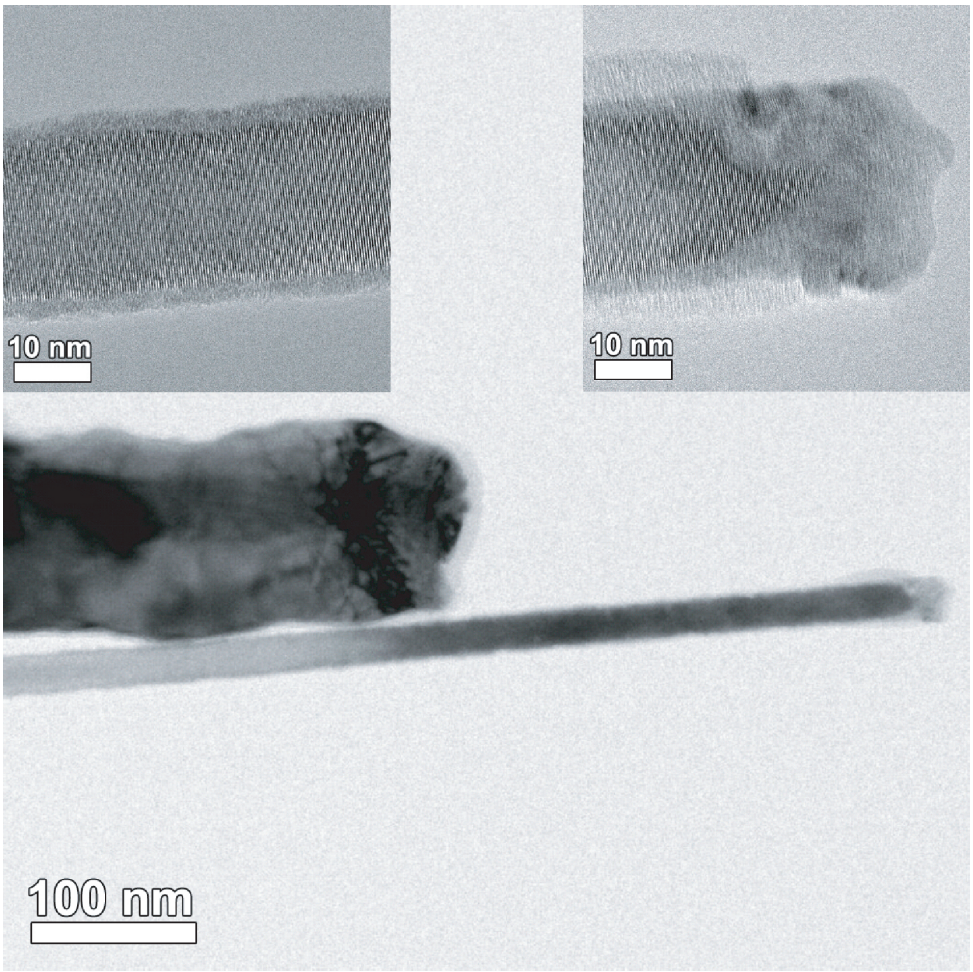


Figure 7.4 Transmission electron microscope (TEM) image of nanowire I on a tungsten support tip. (left inset) High-resolution TEM image of the middle part of the wire in which the crystal planes are resolved. The longitudinal direction of the wire is $\langle 111 \rangle$. (right inset) High-resolution TEM image of the apex of the nanowire showing a polycrystalline fraction.

For a detailed understanding of the emission characteristics of any material, it is required to investigate the relation between the emission properties and the structure of the material. Here we have imaged both nanowires with a Tecnai F30ST transmission electron microscope (TEM, FEI Company) after the emission experiments. The images for nanowire I are shown in Figure 7.4. The high-resolution TEM images reveal the crystal planes perpendicular to the longitudinal direction of

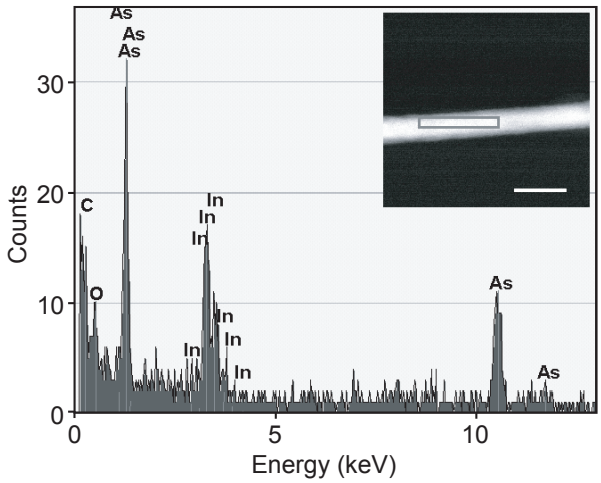


Figure 7.5 EDX data on nanowire I. Inset shows area irradiated by the electron beam.

the nanowire. A lattice spacing of (3.50 ± 0.04) Å was determined corresponding well to the $\langle 111 \rangle$ plane spacing of indium arsenide of 3.4980 Å.[31,32] The lattice constant for indium arsenide a_0 = 0.60584 nm. Therefore, the distance between the $\langle 111 \rangle$ crystal planes is $a_0 / \sqrt{3} = 0.34980$ nm. The TEM images also show a thin amorphous layer surrounding the wire over its entire length and amorphous material with a thickness of about 20 nm at the apex.

The length L_{TEM} and radius R_{TEM} were determined from the TEM image to respective values of 300 nm and 11 nm. These values were used to calculate the field enhancement factor. Numeric calculations of the electric field were performed with the program EMECH (Munro's Electron Beam Software). A rod on a support tip with the same dimensions as determined from the TEM images was modelled in 3D, assuming axial symmetry. The field enhancement factor was calculated to amount to $\beta_{\mathrm{numerical}} = 8.2 \times 10^6$ m^{-1}. The same analysis was performed for the other nanowire. Table 1 compares the obtained values R_{TEM} and $\beta_{\mathrm{numerical}}$, with the values determined from the emission measurements R_{fit} and β_{fit}. For both nanowires, the values of the field enhancement factor agreed within about 20%. This implies that it is reasonable to apply the Fowler-Nordheim model. It also indicates that the shape as seen by the electric field, determining the experimentally obtained field enhancement factor, is approximately equal to the actual shape as determined

Table 7.1 Results of the electron emission measurements and the TEM imaging on nanowires I and II. R_{fit} is the radius of the nanowire obtained by fitting the Fowler-Nordheim model to the data. β_{fit} is the corresponding field enhancement factor. L_{TEM} is the length of the fraction of the nanowire protruding from the support tip as determined from the TEM image and R_{TEM} is the related radius. $\beta_{numerical}$ is the numerically calculated field enhancement factor using the radius and length from the TEM image.

Wire	R_{fit} (nm)	β_{fit} ($\times 10^6\,m^{-1}$)	L_{TEM} (nm)	R_{TEM} (nm)	$\beta_{numerical}$ ($\times 10^6\,m^{-1}$)
I	0.2±0.1	8.7±0.7	300	11	8.2
II	2.1±0.4	6.5±0.2	270	10	7.9

with TEM. The values of the radii as obtained from the emission experiment are much smaller than the wire radii as obtained from the TEM images. The radius as determined from the fit of the current-voltage curve is mainly determined by the size of the emitting area. Looking at Figure 7.4, however, a sharp protrusion is visible at the apex of the nanowire, with a radius of curvature of about 2 nm. This protrusion might have provided a slight additional field enhancement, which could have led to a preference of the emission to occur from the protrusion (compare e.g., the supertip emitter[25]), while the total field enhancement given by the high-aspect nanowires and the support tip hardly changes.

Energy dispersive X-ray (EDX) spectra were recorded to investigate the chemical contents of the nanowires. Spectra were obtained at various positions at the nanowires. From the data obtained at the middle, an In:As ratio of 45:55 (± 10%) was determined, see Figure 7.5. This agrees within the experimental error with the expected stoichiometry of 1:1. EDX data obtained at the apex shows the presence of indium and arsenic in a 60:40 (±10%) ratio. This differs slightly from the ratio obtained at the bulk wire, which could indicate that some As has been removed from the wire's apex. The transformation of the single-crystalline wire's apex into amorphous material can be caused by heating, or electron beam damage in the breaking procedure during mounting, or due to the influence of Joule heating and the electric field during the emission experiments.[20,32] In the bulk of the nanowire, the mean free path for the electrons is 10 nm to 100 nm.[7] We do not know whether

the mean free path in the apex is considerably smaller. If it is much smaller than the dimensions of the amorphous cap, it might influence the emission properties if the scattering is predominantly inelastic. If it is of the same size as the cap, the influence of the cap on the emission properties is expected to be small.

7.5 Conclusions and discussion

In summary, a precise procedure was developed to mount individual indium arsenide nanowires on sharp tungsten support tips. This procedure could possibly find general application for the construction of nanowire probes for, e.g., atomic force microscopy. A detailed investigation of the electron emission properties of individual indium arsenide nanowires was performed. The emission exhibited a narrow electron beam, Fowler-Nordheim-like emission behavior, and a small energy spread. This emission behavior contrasts unstable emission and large energy spread as found for semiconductor emitters and supports the concept of Fermi-level pinning in indium arsenide nanowires. The indium arsenide nanowire thus presents a special type of electron source. The field enhancement factors as determined by fitting the emission data corresponded to the value calculated using the structural information from the TEM images. We envision that indium arsenide nanowires emitters may show emission occurring from quantum confined states when the emitters are externally cooled.

References

1. P. Yang. The Chemistry and Physics of Semiconductor Nanowires. *MRS Bulletin* **30**, 85-91 (2005).

2. Y. Xia, P. Yang, Y. Sun, Y. Wu, B. Mayers, B. Gates, Y. Yin, F. Kim and H. Yan. One-Dimensional Nanostructures: Synthesis, Characterization, and Applications. *Adv. Mater.* **15**, 353-389 (2003).

3. C. M. Lieber. Nanoscale Science and Technology: Building a Big Future from Small Things. *MRS Bulletin* **28**, 486-491 (2003).

4. S. De Franceschi, J. A. van Dam, E. P. A. M. Bakkers, L. F. Feiner, L. Gurevich and L. P. Kouwenhoven. Single-electron tunneling in InP nanowires. *Appl. Phys. Lett.* **83**, 344-346 (2003).

5. F. Patolsky, G. Zheng and C. M. Lieber. Nanowire sensors for medicine and the life sciences. *Nanomedicine* **1**, 51-65 (2006).

6. X. Duan, Y. Huang, Y. Cui, J. Wang and C. M. Lieber. Indium phosphide nanowires as building blocks for nanoscale electronic and optoelectronic devices. *Nature* **409**, 66-69 (2001).

7. Y.-J. Doh, J. A. van Dam, A. L. Roest, E. P. A. M. Bakkers, L. P. Kouwenhoven and S. De Franceschi. Tunable Supercurrent Through Semiconductor Nanowires. *Science* **309**, 272-275 (2005).

8. J. W. G. Wildöer, C. J. P. M. Harmans and H. van Kempen. Observation of Landau levels at the InAs(110) surface by scanning tunneling spectroscopy. *Phys. Rev. B* **55**, 16013-16016 (1997).

9. S. M. Sze *Physics of semiconductor devices*. John Wiley & Sons, New York (1981).

10. B. van Wees. *Phys. World* **9**, 41-45 (1996).

11. P. Mohan, J. Motohisa and T. Fukui. Realization of conductive InAs nanotubes based on lattice-mismatched InP/InAs core-shell nanowires. *Appl. Phys. Lett.* **88**, 013110-013113 (2006).

12. W. Zhu (Ed.) W. Zhu *Vacuum Microelectronics*. John Wiley & Sons, New York (2002).

13. S. Flügge (Ed.) R. H. Good and E. W. Müller *Handbuch der Physik, XXI*. Springer Verlag, Berlin (1956).

14. N. de Jonge, M. Allioux, J. T. Oostveen, K. B. K. Teo and W. I. Milne. Optical Performance of Carbon-Nanotube Electron Sources. *Phys. Rev. Lett.* **94**, 186807-4 (2005).

15. N. de Jonge, E. P. A. M. Bakkers, L. F. Feiner, and A. M. Calvosa. Electron source with low energy spread. European Patent EP1641012 (2005)

16. A. M. Morales and C. M. Lieber. A Laser Ablation Method for the Synthesis of Crystalline Semiconductor Nanowires. *Science* **279**, 208-211 (1998).

17. E. P. A. M. Bakkers, J. A. van Dam, S. De Franceschi, L. P. Kouwenhoven, M. Kaiser, M. Verheijen, H. Wondergem and P. van der Sluis. Epitaxial growth of InP nanowires on germanium. *Nat. Mater.* **3**, 769-773 (2004).

18. N. de Jonge, Y. Lamy and M. Kaiser. Controlled Mounting of Individual Multiwalled Carbon Nanotubes on Support Tips. *Nano Lett.* **3**, 1621-1624 (2003).

19. J. H. Hafner, C.-L. Cheung, T. H. Oosterkamp and C. M. Lieber. High-Yield Assembly of Individual Single-Walled Carbon Nanotube Tips for Scanning Probe Microscopies. *J. Phys. Chem. B* **105**, 743-746 (2001).

20. S. T. Purcell, P. Vincent, C. Journet and V. T. Binh. Hot Nanotubes: Stable Heating of Individual Multiwall Carbon Nanotubes to 2000 K Induced by the Field-Emission Current. *Phys. Rev. Lett.* **88**, 105502 (2002).

21. N. de Jonge, M. Doytcheva, M. Allioux, M. Kaiser, S. A. M. Mentink, K. B. K. Teo, R. G. Lacerda and W. I. Milne. Cap Closing of Thin Carbon Nanotubes. *Adv. Mater.* **17**, 451-455 (2005).

22. K. A. Dean and B. R. Chalamala. Experimental studies of the cap structure of single-walled carbon nanotubes. *J. Vac. Sci. Technol. B* **21**, 868-871 (2003).

23. F. Charbonnier. Developing and using the field emitter as a high intensity electron source. *Appl. Surf. Sci.* **94-95**, 26-43 (1996).

24. L. W. Swanson and G. A. Schwind. A Review of the Zr/O Schottky Cathode *in Handbook of charged particle optics*. J. Orloff (ed.), CRC Press, New York, 77-102 (1997).

25. S. Kalbitzer and A. Knoblauch. High-brightness source for ion and electron beams (invited). *Rev. Sci. Instrum.* **69**, 1026-1031 (1998).

26. R. H. Fowler and L. W. Nordheim. Electron Emission in Intense Electric Fields. *Proc. R. Soc. London* **A119**, 173 (1928).

27. P. W. Hawkes and E. Kasper *Principles of electron optics*. Academic Press, London (1989).

28. O. Groening, O. M. Kuttel, C. Emmenegger, P. Groning and L.

Schlapbach. Field emission properties of carbon nanotubes. *J. Vac. Sci. Technol. B* **18**, 665-678 (2000).

29. G. W. Gobeli and F. G. Allen. Photoelectric Properties of Cleaved GaAs, GaSb, InAs, and InSb Surfaces; Comparison with Si and Ge. *Phys. Rev.* **137**, A245 (1965).

30. S. G. Truxillo, J. C. Blair, N. G. Einspruch and R. Stratton. High-Field Electron Emission from Indium Arsenide. *J. Chem. Phys.* **44**, 1724-1725 (1966).

31. G. Giesecke and H. Pfister. Präzisionsbestimmung der Gitterkonstanten von $A^{III}B^{v}$-Verbindungen. *Acta Crystallogr.* **11**, 369-371 (1958).

32. G. Fursey. Early field emission studies of semiconductors. *Appl. Surf. Sci.* **94-95**, 44-59 (1996).

A

Appendix

A.1 Nanomanipulator specifications

Fine stage range

X-direction:	15 µm
Y-direction:	15 µm
Z-direction:	15 µm

Coarse stage range

X-direction:	4 mm
Y-direction:	4 mm
Z-direction:	2.5 mm

Dimensions

Height without sample sliders mounted:	44 mm
Height with sample sliders mounted:	51.5 mm
Width:	70 mm
Depth:	51 mm

A.2 Parts

The Leiden nanomanipulator consists of the following parts :

- Nanomanipulator insert
- SEM-stage connector block
- High-vacuum feed-through containing 2 high voltage BNC connectors and

3 Caburn connectors
- Attocube system containing:
- Attocube ANC150 controller with additional RS232 interface
- 2x Attocube ANPx50 piezo-motor
- 1x Attocube ANPz50 piezo-motor
- 3 axes piezo amplifier for fine stage (Leiden University ELD)
- Labview data-acquisition cards
- High voltage amplifier to perform field emission tests
- Pico-ammeter (Keithley)
- Joystick (flight controller, at least 3 axes)
- Labview program

A.3 Nanotube (or nanowire) mounting recipe

This is a basic recipe that highlights the different steps performed using the nanomanipulator. For more information on how to prepare samples to mount from and how to detach a nano-object, see Chapter 4.

1. Install CNT sample onto sample slider
2. Install tip onto tip slider
3. Install sliders onto manipulator
4. Evacuate
5. Start imaging
6. Check tip, focus at end of tip
7. Find nanotube
8. Change height of coarse stage, so both tip and nanotube are in focus, i.e. at the same height
9. Approach tip with sample using coarse sample stage
10. If nanotube and tip are in appropriate fine stage range, start using fine stage
11. Approach nanotube with tip underneath, enabling deposition and alignment check
12. Nanotube snaps to tip when separation distance is small enough
13. Align nanotube onto tip using fine stage. By changing the height z of the fine (tip) stage, the development/reduction of slack in the CNT indicates that

the height difference between tip and nanotube is decreasing/increasing. Using this information about the height difference, the tip and nanotube can be positioned in the same *xy* plane that is perpendicular to the electron beam used for imaging.

14. Check conduction between tip and nanotube
15. Improve conduction by irradiating region of overlap with electron beam in reduced area mode
16. Detach carbon nanotube from sample
17. If desired, improve fixation of nanotube using electron beam induced deposition (EBID) of Pt

Summary

This thesis is about the research I performed on novel field emission sources. A field emission source, or electron field emitter, is used to obtain an electron beam by means of applying a high voltage difference between the emitter (cathode) and an extractor (anode) in vacuum. Some time ago, we all used to gaze at electron beam "images" produced by CRT (Cathode Ray Tube) televisions or computer monitors. However, such an electron beam can also be used for microscopy (electron microscope) or lithography (electron beam lithography, used in the chip industry to produce electronics, etc.), where it can be focused into a much smaller spot than possible with photons (light). Hence it is possible to obtain a higher resolution – study smaller objects or write smaller structures – than with optical microscopy or lithography. The quality of the electron beam determines, amongst others, resolution and throughput time of these processes. To have a better electron beam it is possible to improve either the electron optics, or the electron source, and we have chosen to do the latter. Having a better electron source can reduce the time needed to obtain an electron microscope image and enable studying processes at a higher resolution. In electron beam lithography instruments, a better source could provide a higher throughput.

We chose to fabricate electron sources by means of mounting individual nanometer-sized structures, such as nanotubes and nanowires, onto sharp conductive needles. In this context, nano means the diameter of such a nanotube or nanowire is of the order

of a nanometer up to tens of nanometers. Its length, however, is not constrained and therefore such a structure can have a large aspect ratio. These nanostructures have interesting electrical and/or mechanical properties, which make them attractive candidates for novel field emission sources. By using a nanomanipulator inside an electron microscope, we could select and mount an individual nanostructure onto a sharp needle. In a field emission setup, the needle with the nanostructure (cathode or emitter) is placed in front of an extractor (anode) and a voltage difference is applied between. The resulting electric field has its maximum value at the end of the protruding nanostructure; hence the electrons leave the emitter through the end of the nanostructure. The resulting electron beam can be studied in several ways. The total current of the electron beam can be measured and observed as a function of time, but it is also possible to map the electron density of the beam's cross section, also called a field emission pattern. The field emission pattern, obtained with a Field Emission Microscope (FEM), provides information on the shape and electronic structure of the emitting nanostructure. In this situation, where we have a sample with only a single emitting structure, it is possible to also study the structure's morphology before and/or after field emission experiments inside a high resolution Transmission Electron Microscope (TEM) and relate it to the electron emission characteristics. The theory behind the field emission process and the FEM is described in Chapter 2.

A carbon nanotube can be thought of as a sheet of carbon atoms inside a hexagonal lattice – also known as graphene – rolled up into a cylinder. The two ends of this cylinder can be either open or closed, where the closed end state is the energetically favorable and more stable configuration. As in a field emission experiment electrons are most likely to come from one of the nanotube's end states, it is imperative to know, or even better, to control the end state in our experiments. We found that the emission pattern from a naturally closed carbon nanotube showed a symmetry that can be related to the symmetric positions of the carbon atoms that make up the hemi-spherically shaped cap. Such a cap can be envisioned as one half of a soccer ball, consisting of five- and six-membered rings, also know as pentagons and hexagons. The carbon atoms are located at the corners of the pentagons and hexagons that make up the closed cap. Experiments on carbon nanotubes with such

a closed cap are described in Chapter 6.

In the selecting and mounting process of a nanostructure, the performance of the electron microscope, in which the mounting is done, determines what is feasible. For example: Is it possible to identify single nanostructures at all? Does the electron imaging harm the nanostructure? A new high resolution scanning electron microscope in our group in Leiden asked for its own nanomanipulator. As this microscope put more constraints on the materials being used, it was not possible to copy the setup we had been using at the Philips Research Labs. Based on these constraints and on experiences operating nanomanipulators, such as the one at Trinity College in Dublin, we came up with a completely new design. Although it took longer than planned, the result was an instrument much more versatile than we had envisioned, as you can read in Chapter 3. Collaborations with other groups, such as the Quantum Transport group at Delft University of Technology and the Quantum Optics group at Leiden University, led to successful experiments on samples fabricated using our nanomanipulator setup. The techniques used when mounting nanostructures onto sharp needle-shaped tips, are described in Chapter 4.

We discovered that we could use the high current electron beam of the new electron microscope to cut through our nanotubes and hence control their length. As this affected the end configuration of the nanotubes, we needed to find a way to "repair" them. We succeeded in re-obtaining closed caps during field emission experiments on carbon nanotubes that were previously cut by using this method, see Chapter 5.

Besides carbon nanotubes, we also studied the field emission properties of indium arsenide (InAs) nanowires. Nanowires are solid cylinders of a certain material, with specific electrical and/or mechanical properties. In the case of semiconductor InAs nanowires, we expected to obtain an electron beam with a very low energy spread. In Chapter 7 we describe how we mounted and controlled the length of such nanowires on sharp tips and performed field emission experiments.

Not to be found in this thesis, however, are the experiments performed on sources I made for FEI Beamtech, Hillsboro, USA. Measurements at their laboratory yielded

promising results, but it is a long road towards an application. Although, in my opinion, they had a great success in managing to operate a closed capped MWNT at their facility – that had been produced in our laboratory – it was not good enough to match the requirements set by Beamtech.

Samenvatting

Dit proefschrift gaat over het onderzoek dat ik heb gedaan naar nieuwe veldemitters. Een veldemitter, oftewel een veldemissie elektronenbron, wordt gebruikt om een elektronenbundel te genereren door in een vacuümopstelling een hoog spanningsverschil tussen de emitter (cathode) en een extractor (anode) aan te brengen. Enige tijd geleden waren we allemaal nog gewend om naar beelden te staren, die door middel van een elektronenbundel gegenereerd werden op een CRT (kathodestraalbuis) televisie of computer monitor. Zo'n elektronenbundel kan echter ook gebruikt worden voor microscopie (elektronenmicroscoop) of lithografie (elektronenbundel lithografie, gebruikt in de chip industrie om elektronica te produceren, etc.), waar deze bundel gefocusseerd kan worden tot een veel kleinere spot dan mogelijk is met fotonen (licht). Hierdoor is het mogelijk een hogere resolutie te behalen – oftewel om kleinere objecten te bestuderen of kleinere structuren te schrijven – dan met optische microscopie of lithografie. De kwaliteit van de elektronenbundel bepaalt onder andere de resolutie en schrijftijd in deze processen. Voor een betere elektronenbundel kan gewerkt worden aan het verbeteren van de elektronenoptica of de elektronenbron, waarbij wij gekozen hebben voor het laatste. Met een betere elektronenbron kan ook de tijd om een beeld met een elektronenmicroscoop te maken verkort worden en kunnen processen bestudeerd worden met een hogere resolutie. In het geval van elektronenbundel lithografie kan een betere bron een hogere doorstroming leveren.

Wij hebben gekozen om elektronenbronnen te maken door middel van het monteren van individuele nanostructuren, zoals nanobuizen en nanodraden, op scherpe, geleidende naalden. In deze context betekent nano dat de diameter van een dergelijke nanobuis of nanodraad zich in de grootte orde van één tot tien nanometer bevindt, waarbij de lengte ervan niet vastgelegd is; een grote aspect ratio is dus mogelijk. Deze nanostructuren hebben interessante elektrische en/of mechanische eigenschappen, die ze tot aantrekkelijke kandidaten voor nieuwe elektronenbronnen maken. Met behulp van een nanomanipulator in een elektronenmicroscoop, zijn we in staat om een individuele nanostructuur te selecteren en te monteren op zo'n scherpe naald. In een veldemissie opstelling wordt de naald met de nanostructuur (de cathode of emitter) voor een extractor (anode) geplaatst waarna er een elektrisch spanningsverschil tussen beide wordt aangebracht. Het resulterende elektrische veld heeft een maximum aan het eind van de uitstekende nanostructuur, waardoor de elektronen de emitter verlaten door het einde van deze nanostructuur. De resulterende elektronenbundel kan op verschillende manieren bestudeerd worden. De totale stroom van de elektronenbundel kan als functie van de tijd gemeten en bekeken worden, maar het is ook mogelijk om de elektronendichtheid in een crosssectie van de bundel te plotten, ook wel een veldemissie patroon genaamd. Dit veldemissie patroon, verkregen met behulp van een zogenaamde veldemissie microscoop (FEM), geeft informatie over de vorm en elektronische structuur van de emitterende nanostructuur. Aangezien we dus een sample hebben met één enkele emitterende nanostructuur, kunnen we vervolgens proberen om dit patroon te relateren aan de morfologie van deze structuur. Om in nog meer detail de vorm van de emitter te relateren aan de veldemissie karakteristieken, kunnen we voor en/of na de veldemissie experimenten de emitter afbeelden met een hoge resolutie transmissie-elektronenmicroscoop (TEM). De theorie waarmee we het veldemissie proces kunnen beschrijven, is te vinden in Hoofdstuk 2.

Een koolstofnanobuis kan worden beschouwd als een enkele platte laag koolstofatomen in een hexagonaal rooster (kippengaas) – ook wel grafeen genaamd – opgerold tot een cilinder. De twee uiteinden van deze cilinder kunnen open of gesloten zijn, waarbij de gesloten variant de energetisch voordeligere en stabielere configuratie is. Omdat het in onze veldemissie experimenten waarschijnlijk is dat de

elektronen uit een van deze uiteinden komen, is het belangrijk om de toestand van dit uiteinde in onze experimenten te kennen, of om dit te controleren. We hebben gevonden dat het emissiepatroon van een van nature gesloten koolstofnanobuis een symmetrie vertoont die gerelateerd kan worden aan de symmetrische posities van de koolstofatomen die het bolvormige uiteinde vormen. Zo'n bolvormig uiteinde kan worden voorgesteld als een halve voetbal, bestaande uit vijf- en zeshoeken, oftewel pentagons en hexagons. De koolstofatomen bevinden zich hierbij op de hoeken van de pentagons en hexagons. Experimenten aan koolstofnanobuizen met een dergelijk gesloten uiteinde worden beschreven in Hoofdstuk 6.

Bij het selecteren en monteren van een nanostructuur bepaalt de performance van de elektronenmicroscoop – waarin het monteren plaatsvindt – wat er mogelijk is. Bijvoorbeeld of het mogelijk is om één enkele nanostructuur te identificeren. Of dat het bekijken van de nanostructuur met de elektronenbundel de nanostructuur beschadigt. Door de aanschaf van een nieuwe hoge-resolutie rasterelektronenmicroscoop (SEM) in onze vakgroep in Leiden, ontstond de vraag naar een nieuwe nanomanipulator. Aangezien deze microscoop strengere eisen stelt aan de hiervoor gebruikte materialen, was het niet mogelijk de reeds bestaande opstelling bij Philips laboratoria in Eindhoven te kopiëren. Door deze beperkingen en mede door onze ervaringen met nanomanipulatoren, zoals die bij Trinity College in Dublin, zijn we tot een compleet nieuw ontwerp gekomen. Alhoewel de gehele ontwikkeling en fabricage langer duurden dan verwacht, was het resulterende instrument veel veelzijdiger dan van tevoren verwacht, zoals in Hoofdstuk 3 te lezen is. Samenwerkingen met andere groepen, zoals de Quantum Transport groep aan de Technische Universiteit Delft en de Quantum Optica groep in Leiden, leidden tot succesvolle experimenten aan samples gefabriceerd met onze nanomanipulator opstelling. De gebruikte technieken bij het monteren van nanostructuren op scherpe naalden worden beschreven in Hoofdstuk 4.

We hebben ontdekt dat we de hoge stroom van de elektronenbundel in de nieuwe elektronenmicroscoop konden gebruiken om nanobuizen door te branden en ze zodoende op lengte te maken. Omdat deze methode de toestand van het uiteinde verandert, hadden we een manier nodig om het uiteinde te repareren. We zijn er

gedurende veldemissie experimenten in geslaagd om opnieuw een gesloten uiteinde te creëren aan koolstofnanobuizen die op deze manier ingekort waren, zie hiervoor Hoofdstuk 5.

Naast koolstofnanobuizen hebben we ook de veldemissie eigenschappen van indium arseen (InAs) nanodraden onderzocht. Nanodraden zijn massieve cilinders van een bepaalde stof, met specifieke elektrische en/of mechanische eigenschappen. In het geval van halfgeleidende InAs nanodraden, verwachtten we een elektronenbundel te kunnen genereren met een bijzonder lage energiespreiding. In Hoofdstuk 7 staat beschreven hoe we deze nanodraden hebben gemonteerd op scherpe naalden – waarbij we hun lengte hebben gecontroleerd – en vervolgens veldemissie experimenten hebben uitgevoerd.

List of publications

1. E. C. Heeres, T. H. Oosterkamp and N. de Jonge. Size of the localized electron emission sites on a closed multiwalled carbon nanotube. Phys. Rev. Lett. 108, 036804 (2012).

2. T. van der Sar, J. Hagemeijer, W. Pfaff, E. C. Heeres, S. Thon, H. Kim, P. Petroff, T. H. Oosterkamp, D. Bouwmeester and R. Hanson. Effect of a nanoparticle on the optical properties of a photonic crystal cavity: theory and experiment. J. Opt. Soc. Am. B 29, 698-703 (2012).

3. E. C. Heeres, T. H. Oosterkamp and N. de Jonge. Making carbon nanotube electron sources of defined lengths and with closed caps. Nanotechnology 22, 235308 (2011).

4. T. van der Sar, J. Hagemeier, W. Pfaff, E. C. Heeres, S. M. Thon, H. Kim, P. M. Petroff, T. H. Oosterkamp, D. Bouwmeester and R. Hanson. Deterministic nanoassembly of a coupled quantum emitter--photonic crystal cavity system. Appl. Phys. Lett. 98, 193103 (2011).

5. E. C. Heeres, A. J. Katan, M. H. van Es, A. F. Beker, M. Hesselberth, D. J. van der Zalm and T. H. Oosterkamp. A compact multipurpose nanomanipulator for use inside a scanning electron microscope. Rev. Sci. Instrum. 81, 023704 (2010).

6. D. J. van der Zalm, E. C. Heeres, M. B. S. Hesselberth, A. J. Katan, and M. H. van Es. A nano-scale manipulator. U.K.Patent Application GB0908780.0 (2010)

7. J. D. Jarvis, H. L. Andrews, B. Ivanov, C. L. Stewart, N. de Jonge, E. C. Heeres, W. P. Kang, Y. M. Wong, J. L. Davidson and C. A. Brau. Resonant tunneling and extreme brightness from diamond field emitters and carbon nanotubes. J. Appl. Phys. 108, 094322-094326 (2010).

8. T. van der Sar, E. C. Heeres, G. M. Dmochowski, G. de Lange, L. Robledo, T. H. Oosterkamp and R. Hanson. Nanopositioning of a diamond nanocrystal containing a single nitrogen-vacancy defect center. Appl. Phys. Lett. 94, 173104-3 (2009).

9. T. van der Sar, E. C. Heeres, T. H. Oosterkamp and R. Hanson. Quantumcircuitjes bouwen in een elektronenmicroscoop. Nederlands Tijdschrift voor Natuurkunde 11, 408 (2009).

10. E. C. Heeres, E. P. A. M. Bakkers, A. L. Roest, M. Kaiser, T. H. Oosterkamp and N. de Jonge. Electron Emission from Individual Indium Arsenide Semiconductor Nanowires. Nano Lett. 7, 536-540 (2007).

11. W. M. van Spengen and E. C. Heeres. A method to extract the lateral and normal components of motion from the capacitance change of a moving MEMS comb drive. Journal of Micromechanics and Microengineering 17, 447 (2007).

CV

Curriculum Vitae

Erwin Cornelis Heeres is op 31 juli 1977 geboren in Oss. In 1995 behaalde hij zijn gymnasiumdiploma aan het Titus Brandsma Lyceum te Oss, waarna hij begon aan de studie Technische Natuurkunde aan de Technische Universiteit Delft. Zijn afstudeeronderzoek rondde hij in 2003 af in de vakgroep Quantum Transport bij Prof. Dr. Ir. J. E. Mooij. Dit onderzoek betrof het ontwerpen en fabriceren van en meten aan een gradiometer ontwerp van een Josephson persistent current quantum-bit. In april 2004 begon hij aan zijn promotieonderzoek in de Interface Physics groep aan de Universiteit Leiden. Hij verrichtte onderzoek naar het verbeteren van elektronenbronnen met behulp van koolstof nanobuisjes, onder directe begeleiding van Prof. Dr. Ir. T. H. Oosterkamp. Een groot deel van dit onderzoek verrichtte hij aan het Natuurkundig Laboratorium van Philips in Eindhoven, onder begeleiding van Prof. Dr. Niels de Jonge. Hierna was hij nog werkzaam als onderzoeker aan de Technische Universiteit Delft en aan de Universiteit Leiden. Sinds 2008 leidt hij zijn eigen bedrijf Frozen Lines.

thx

Acknowledgements

Although only a single name is on the cover of this thesis, it would not have been possible to complete this research all by myself. During my PhD, I had the opportunity to work together with many great people, that helped me, provided me with support, or advice.

Most of the work presented in this thesis is part of the research performed within the Novel Electron Sources Project (NES), where we looked for industrial applications of evolving (nano-)technologies. My group in Leiden – the Interface Physics group, led by Joost Frenken – has always been very supportive to me, although most of the actual electron source measurements were performed at the Charged Particle Optics (CPO) group at the Philips Research Laboratories in Eindhoven, Netherlands.

First of all I would like to thank both my supervisors Niels de Jonge and Tjerk Oosterkamp for all their help and support. I am thankful I was given the opportunity to be a part of this challenging project and of two teams. It was a great team effort to design and build such a versatile nanomanipulator for the brand new electron microscope, and I would like to acknowledge the other people closely involved: Allard Katan, Maarten van Es, Anne France Beker, Marcel Hesselberth and Dian van der Zalm. I would like to thank Dirk van Baarle – who performed his B.Sc. research with me – for your nanotube shortening experiments, mounting experiments and

help on the nanomanipulator's software. Thanks to the always helpful team at the fine mechanics department – Emiel Wiegers, and Martijn Witlox – and Bert Crama at the electronics department. Thank you Ellie van Rijsewijk-Salman for all the administrative help and support.

Thank you to all the people at Philips who helped me find my way at their labs and contribute to my research. The CPO group members: Maya Doytcheva, Antonio Calvosa, Mikhail Ovsyanko, Theo van Rooij, John Cox, and Sjoerd Mentink. The nanowire team of Erik Bakkers, Aarnoud Roest, and Lou-Fé Feiner. Last but not least the materials analysis section that helped me obtain even better electron microscope images of our samples inside their high resolution TEM: Monja Kaiser and Marcel Verheijen.

The move of Niels de Jonge to the U.S. – at the start of the project CPO group member at the Philips laboratories – provided the opportunity to visit him and Diana and to work together with the Vanderbilt University team: Charles Brau, Jonathan Jarvis and Heather Andrews.

I would like to thank Ronald Hanson and Toeno van der Sar from Delft University of Technology for the cooperative work on the nanodiamonds.

A final thank you to my parents Kees and Else and my brother Martin for all their support throughout the years.